DYNAMIC NMR STUDIES OF POLYMER ELECTROLYTE MATERIALS FOR APPLICATION TO LITHIUM-ION BATTERIES AND FUEL CELLS

by

AMISH N. KHALFAN

A dissertation submitted to the Graduate Faculty in Physics in partial fulfillment of the requirements for the degree of Doctor of Philosophy, The City University of New York

2007

This manuscript has been read and accepted for the
Graduate Faculty in Physics in satisfaction of the
dissertation requirement for the degree of Doctor of Philosophy.

Steven G. Greenbaum

Date — Chair of Examining Committee

Sultan Catto

Date — Executive Officer

Gregory Boutis

Leon Cohen

Yuhang Ren

Supervisory Committee

THE CITY UNIVERSITY OF NEW YORK

Abstract

DYNAMIC NMR STUDIES OF POLYMER
ELECTROLYTE MATERIALS FOR APPLICATION
TO LITHIUM-ION BATTERIES AND FUEL CELLS

by

Amish N. Khalfan

Adviser: Professor Steven G. Greenbaum

This dissertation investigates the structural and dynamical properties of polymer electrolyte materials for applications to lithium-ion batteries and fuel cells. The nuclear magnetic resonance (NMR) technique was used to characterize these materials. NMR aids in understanding the local environments of nuclei and the mobility of a molecular/ionic species. Five research projects were carried out, and they have been outlined in this work.

NASA has developed rod-coil block copolymers for use as electrolytes in lithium-ion batteries. The copolymers exhibit a microphase separation within their structure leading to the formation of ionically conducting channels. We studied ion transport properties of the copolymers, and determined the predominant mechanism for transport to occur in the amorphous phase.

Seven gel polymer electrolytes, each containing a mixture of LiBETI salt and organic solvents, were studied. Two of them incorporated BMI (1-n-butyl-3-methylimidazolium) ionic liquid. Ionic liquids are room temperature molten salts. BMI had been thought to enhance ion mobility. However, the BMI component was observed to restrict ion mobility.

Gel polymer electrolytes containing LiTFSI salt and P_{13}TFSI ionic liquid with or without the inclusion of ethylene carbonate (EC) were studied for application to lithium metal/air batteries, which have high theoretical energy densities. The addition of EC was found to improve lithium ion transport. The gels with EC therefore prove to be favorable for use as electrolytes in lithium metal/air batteries.

Highly sulfonated poly(arylenethioethersulfone) (SPTES) membranes were examined for use in direct methanol fuel cells (DMFCs) as an alternative to the Nafion membrane. DMFCs use methanol as a fuel instead of reformed hydrogen as in conventional proton exchange membrane fuel cells. Compared to Nafion, the SPTES membranes were shown to retain water better at high temperatures and yield lower methanol diffusion.

SPTES membranes with the addition of fluorine groups (6F-SPTES) were also studied, and these membranes had been thought to show an improvement in water transport properties over SPTES. However, water diffusion studies of the 6F-SPTES membranes revealed the fluorinated membranes to be unfavorable. The morphology of the FSPTES is suspected to be more susceptible to the loss of bound water at higher temperatures than SPTES.

Acknowledgments

I would like to thank my mentor, Prof. Steven Greenbaum, for his wisdom, generosity, and tireless support. He is a gem in the scientific community and a true steward of physics whose work remains an inspiration to young scientists of all backgrounds. I'd like to thank all the postdoctoral scientists I have worked with over the years, especially Dr. Jay Jayakody and Prof. Phil Stallworth. From them I've learned a great deal about experimental methodology, NMR theory, and data analyses, and I have gained invaluable insight as a result. I'd very much like to thank all my lab mates and colleagues, George Bennett, Gabriel Goenaga, Nicole Leifer, Chandana Kodiweera, Luz Sanchez, Lina Gonzalez, and Jaime Farrington, for sharing their knowledge, encouraging me, and just being wonderful people to be around and know. I wish to thank Prof. Sultan Catto and Miss Allida Gupton for their compassion, encouragement, and their dedication in keeping the physics program at the Graduate Center one of the highest caliber.

To all my friends, thank you for your loyalty and support. I'd like to thank my twin brother Imtiaz for not choosing to go into physics and leaving me something to identify with on my own. I'd like to thank him as well as my younger brother Parvez for their helpful words, support, and for being the best brothers one could ask for. I would like to extend my warmest thanks to my mother, Fatma Khalfan, and father, Nurali Khalfan, for their unconditional love and hard work in having raised me. It is to them that I dedicate this work.

Table of Contents

Lists of Tables, Schemes and Figures

Chapter 1

Chapter 2

Chapter 5

Chapter 6

Chapter 1: Introduction

1.1 Setting Our Sights on Alternative Energy Devices

As the demands for energy increase on a global scale and the production of fossil fuel energy sources such as oil and natural gas nears decline, alternative energy sources are being highly sought after. Currently, over 80% of the world's energy is supplied by the use of fossil fuels, and a threefold increase in energy demand is anticipated for the end of this century [1]. Concerning our environment, dangerous amounts of CO_2 gases are being released into the atmosphere from the burning of fossil fuels. Undesirable climate changes arise as a result and the effects of global warming become more widespread and realizable. In addition, energy contributes greatly to the economic health of countries around the world [2]. Electricity remains one of the largest energy commodities being bought and sold in America's economy. An increase in demand for electrical energy is indicative of a fast growing use of electric based technologies, which help to boost an economy. Cheaper energy is therefore desired in order for a more consumer driven market to prosper.

Renewable alternative sources of energy are actively being pursued in efforts to minimize the reliance on fossil fuels. Such sources include solar, hydroelectric, geothermal, wind, nuclear and even biomass. In Brazil, for instance, biomass conversion of sugar cane to alcohol is used to power vehicles [1]. Although alternative sources are being investigated and implemented to some extent, alternative energy devices such as rechargeable lithium-ion (Li-ion) batteries and fuel cells can help to utilize available energy more efficiently. Li-ion

batteries, in particular, are energy storage devices which can hold their charge very well, possess high energy densities, and provide high power discharge during operation. To date, Li-ion batteries power portable devices such as laptops and cell phones, military electronics including radios and mine detectors, spacecraft, and satellites. Fuel cells, on the other hand, are energy conversion devices that release environmentally-friendly byproducts such as water and heat during operation. Like the Li-ion battery, a fuel cell system has a high energy density, a property dependent on the kind of fuel being employed. Instead of recharging as with the lithium-ion battery, the fuel cell can be refueled by various pump mechanisms. Fuel cells presently supply back-up power to buildings and homes and have also been powering space vehicles since the 1960s [3]. Future commercial applications for fuel cells are likely to include portable electronics and cars. Li-ion batteries and fuel cells share a critical component in their design, namely, the electrolyte, which is a permeable medium allowing for the transfer of ions.

Polymer-based electrolyte membranes, in particular, offer mechanical strength, dimensional stability, flexibility in design, and safety of use when employed in Li-ion cells or fuel cells. Pure liquid electrolyte systems can leak reactive and potentially reactive chemicals under certain operation conditions or even storage. The Li-ion battery and fuel cell heavily rely upon the mechanical, thermal, electrochemical and conductive properties of their respective electrolyte membranes. The electrolyte membrane permits ion conduction, which strongly correlates to the amount of electric power delivered to an electronic device of

interest. A vast amount of scientific research has been dedicated to improving the structural and dynamical properties of electrolyte membranes so as to enhance the performance and efficiency characteristics of Li-ion batteries and fuel cells. For the studies contained herein, various polymer-based electrolyte membranes were investigated for applications to both Li-ion batteries and fuel cells. A central focus in carrying out the studies hinged upon understanding the mechanism of ion and molecular transport in these membranes for the development of better performing lithium batteries and fuel cells than what is available in today's market.

1.2 The Evolution of Batteries and the Emergence of the Lithium-Ion Battery

Dating back approximately 2000 years ago in the ancient Middle East, the "Baghdad" battery, is believed to have been the first battery devised, and it may have been used for electroplating objects with gold. The battery consisted of a clay vessel inside of which a copper cylinder stood, with an iron bar inside the copper cylinder (See Figure 1.1) [4]. Wine or vinegar was most likely used as the electrolyte. Replicas of this primitive battery have shown to generate 0.8 to 2 volts, driving a current sufficient to produce a thin layer of gold on an object. It wouldn't be for another 1800 years that the battery would be rediscovered.

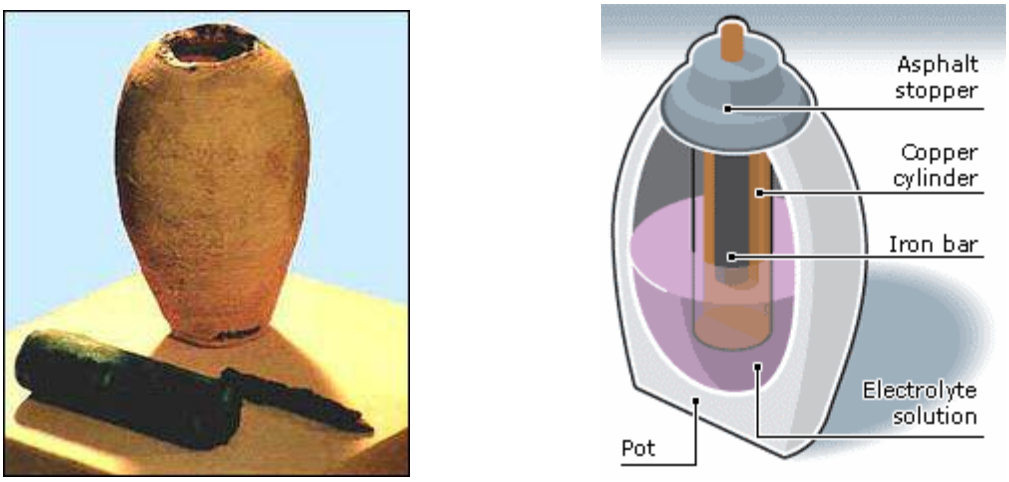

Figure 1.1- The Baghdad battery and its components.

In the year 1800, Alessandro Volta invented the electric battery with which we are familiar today. His battery design consisted of cells. In the simplified model of such a cell, a copper strip and a zinc strip are partially submerged in a solution of sulfuric acid H_2SO_4 in water as a conducting wire connects both metals [5]. In water, sulfuric acid dissociates into $2H^+$ and SO_4^{2-} ions and an electrolyte medium is formed (See Figure 1.2). The electrolyte solution will tend to dissolve the zinc strip. For a particular zinc atom on the strip, two of its electrons are left behind as Zn^{2+} enters the solution and clings to, or associates with, a negatively charged SO_4^{2-} group. The electrons pass from the zinc strip to the copper through the conducting wire since copper has a stronger affinity for the attraction of electrons than does zinc due to their relative outermost electron configuration. A copper atom then gains two electrons The electrolyte becomes positively charged with more and more Zn^{2+} ions, the Zn^{2+}

and H^+ ions will draw negative charge through electrostatic interaction, in which case the Cu^{2-} ions enter the solution and associate with the positive ions. During this process, the zinc rod becomes increasingly negatively charged (termed the negative electrode) as the copper becomes increasingly positive such that a potential difference exists with positive current flowing from the copper strip to the zinc. This current can be used to power a load, i.e. a light bulb, connected via the conducting wire.

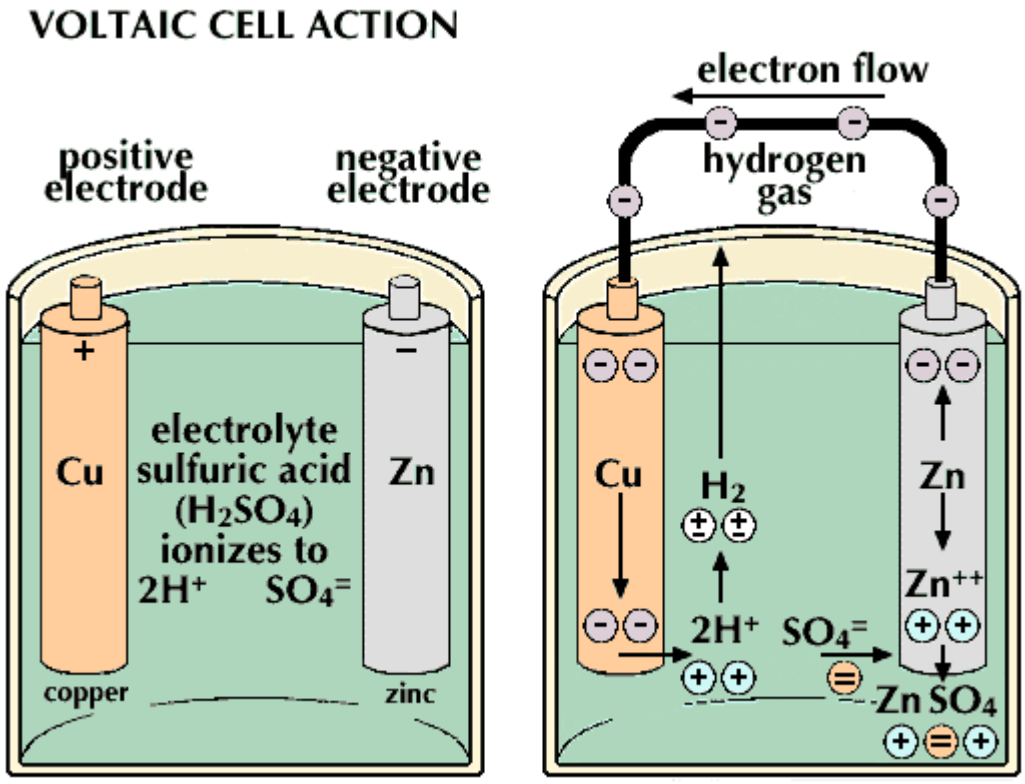

Figure 1.2 - A voltaic cell produces current when the electrodes are joined by a conducting wire [6].

In a Voltaic cell, work is done on the electrons by an electric field existing within the conducting wire due to the oppositely charged electrodes. In terms of energy, the work to accomplish electron transfer makes use of electric potential energy that has been stored as a result of the chemical reactions having taken place. When the electrons have used up all the available electric potential energy, then the battery is considered dead unless some external source can now drive the electrochemical process in reverse and recharge the battery. Volta's battery consisted of stack of zinc and silver discs with a piece of cardboard soaked in salt solution lying between each pair of electrodes to prevent them from touching and shorting out. Connecting the zinc-silver cells in series was found to yield a greater output voltage. Multi-cell batteries "pump" fewer electrons while giving each electron more energy [7].

Some time after Volta's invention, in 1859, the lead-acid battery was invented. The lead-acid battery is a rechargeable storage battery whose energy can be replenished many times, and it is commonly used to start car motors. In a standard automobile, 6 lead acid cells are connected in series to give an output voltage of 12 volts. The reason why a car battery can last so long is that the car routinely recharges the battery through an electric generator, which converts mechanical work into useful electrical energy. Some of the electric power produced is used to increase the battery's chemical potential energy by reversing the chemical reactions associated with discharge. Lead and lead dioxide electrodes are what allow a lead-acid battery to deliver the enormous currents required to start a car as these electrodes possess a large amount of surface area.

Lead acid batteries don't last forever since the charging and discharging cycles slowly damage the electrodes, eventually causing them to make contact with one another or fall to the bottom of the container of a particular cell [7].

The alkaline battery was invented in 1866. It is commonly used to power flashlights and remote controls. It is more compact and of less weight than a lead-acid battery although an alkaline battery typically has a shorter lifetime since its electrochemical reaction is not reversible. An alkaline battery incorporates a positive carbon and manganese dioxide positive electrode on the outside and a powdered zinc electrode at the center of the cell (See Figure 1.3) [8], [9]. An electrolyte paste of potassium hydroxide and water is used. A paste instead of a pure liquid is used for protection against dangerous chemical leakage. When in water, the potassium hydroxide dissociates into potassium ions (K^+) and hydroxyl ions (OH^-) in water. The abundance of hydroxyl ions in the paste makes it alkaline. The powdered zinc electrode provides the large surface area needed for high current applications. A typical alkaline cell has a potential difference of about 1.5 volts between its positive and negative terminals.

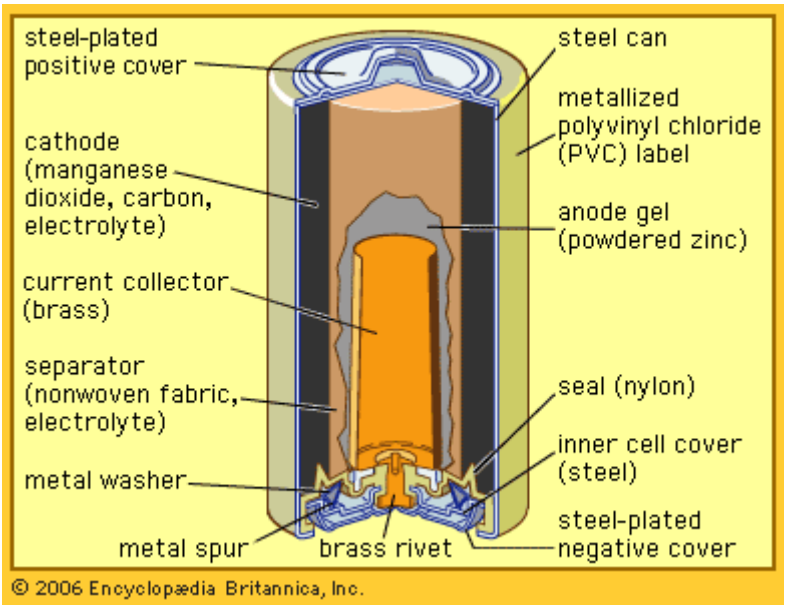

Figure 1.3 - A cross sectional view of an alkaline–manganese dioxide power cell.

The nickel-cadmium, or Ni-Cd, rechargeable battery first appeared in 1899. Ni-Cd batteries can be used to power portable CD players, transistor radios and toy racing cars. They compete with alkaline batteries. A Ni-Cd cell has a lower discharge capacity than that of an equivalent alkaline cell, a lower nominal cell voltage (1.2 volts), and the Ni-Cd cell is a bit more costly. However, a Ni-Cd battery has a longer lifetime than the alkaline battery because of its inherent ability to recharge via external power. The Ni-Cd battery also maintains a nearly constant voltage during discharge whereas the alkaline battery's voltage drops as the amount of charge drops. In comparison to rechargeable lead-acid batteries, Ni-Cd batteries have higher energy densities, typically last longer (i.e. have a greater number of charge/discharge cycles), and have faster charge and discharge rates.

The operational principle underlying Ni-Cd batteries is based on its multiple valence states, as present in the transition metals. This flexibility is also found in the manganese atoms of the alkaline cells. Nickel can form stable molecules while sharing either two or three of its electrons with other atoms, and it has a stronger attraction for electrons than cadmium. A drawback of the Ni-Cd battery is the toxicity of cadmium. Manufactures have used materials other than cadmium for the negative electrode such as a compound consisting of rare earth metals (e.g. lanthanum, cerium) to construct what is known as a nickel-metal-hydride or NiMH battery. NiMH batteries have less memory problems than Ni-Cd's, or rather, don't have to be fully discharged before recharged (as doing so can lead to quick discharge and loss of charge capacity over time), require a shorter amount of time to fully charge, and are more ecological [10]. On the flip side, NiMH batteries have higher rates of self-discharge.

It wasn't until the 1970s that lithium batteries (prior to lithium-ion) became commercially available even though revolutionary work on such batteries began in 1912 by G.N. Lewis [11]. Lithium batteries derive their energy from lithium metal's electropositive nature. Lithium is therefore highly reactive. It gives up an electron so easily that it reacts violently with many chemicals. Lithium reacts so strongly with water such that water-based electrolytes are not used in lithium batteries. Instead, various organic solvents are used in which lithium salts are dissolved to form the electrolytes. Lithium is also one of the lightest elements and the lightest of all metals, which allows it to store a great deal of chemical potential energy and to have the largest specific energy density. The

negative electrode (or anode) in the lithium cell is commonly metallic lithium with the positive electrode (cathode) being one of a number of transition metal oxide components. A porous material soaked with the electrolyte is sandwiched between the electrodes and is termed a separator as it functions to prevent touching of the electrodes and short circuiting. Also, current collectors sit on the cathode and anode. The lithium cell is usually manufactured as a coin cell and can generate voltages of 3 volts or more, twice more than an alkaline battery. Lithium batteries are used for watches and cameras, where reductions in weight and volume are important.

It turned out to be quite a struggle to make the lithium batteries rechargeable because of the instability of lithium metal. The design of the battery gradually changed to a non-metal lithium battery which highlighted the use of lithium ions. In 1990, the Sony Corporation commercialized the first Li-ion battery [12]. Although slightly lower in energy density than lithium metal, the Li-ion is safe when certain precautions are met during charging and discharging. The energy density of Li-ion cell is typically twice than that of the standard Ni-Cd cell. A potential for higher energy densities exists for Li-ion batteries as well. The rechargeable Li-ion battery can perform charge/discharge cycles many times over and has a longer cycle life than the Ni-Cd battery. With only one Li-ion cell, a superior electromotive force of 3.6 volts is generated. A nickel-based pack would require three 1.2-volt cells connected in series to yield the same amount of voltage. As it stands, most of today's cellular phones run on a single Li-ion cell. The Li-ion battery has the advantage of being a low maintenance battery,

something which most other battery chemistries cannot claim [7]. There is no memory effect with the Li-ion battery, and no scheduled cycling is required to prolong the battery's life. In addition, the self-discharge of a Li-ion battery is less than half compared to that of the Ni-Cd battery [12]. Li-ion cells cause little harm when disposed. Rechargeable Li- ion batteries do not use environmentally harmful heavy metals such as cadmium and lead, and they are thus environmentally friendly. The Li-ion rechargeable battery has ushered in the most important period in battery history since the Baghdad battery, and its applications continue to grow with the ever-increasing technological demands of society.

The Li-ion cell battery has three main components: the cathode, the electrolyte, and the anode as shown in Figure 1.4 [13, 14]. A lithium transition metal oxide compound (e.g. lithium cobalt oxide) comprises the cathode, and it functions as an electron acceptor. The anode is usually a composite consisting of mostly carbon such as graphite or carbon fibers. There is conventionally a non-aqueous liquid electrolyte having a lithium salt, e.g. lithium hexafluorophosphate dissolved in a non-aqueous organic solvent, injected onto a porous polyolefin separator between the electrodes. In the charge process, the lithium ions transport from the cathode through the permeable electrolyte and into anode. The free electrons move to the current collector and pass through an external circuit. At the anode during charging, a lithium ion combines with an electron and intercalates, or is inserted, into layers of carbon atoms through a reduction reaction. The opposite occurs during the discharge process as the lithium ions of a carbon layer in the anode are now released and finally inserted into the cathode material (i.e.

between planes of oxygen atoms). In the discharge process, lithium is reduced at the cathode (i.e. $Li^+ + e- \rightarrow Li$) If an external load is connected, power is delivered to that particular device, e.g. a notebook computer or cellular phone. The ability to intercalate lithium into the carbon structure of the anode plays an important role in determining the performance of the battery in terms of its charge/discharge capacity, voltage stability, and cyclic stability [15]. A key factor in improving the performance and efficiency of a Li-ion battery lies in synthesizing an electrolyte which is electrochemically stable and one that sustains a high ionic conductivity over a wide range of temperatures. In general, high ionic mobility and a high ionic conductivity of the electrolyte allow having a high output of power.

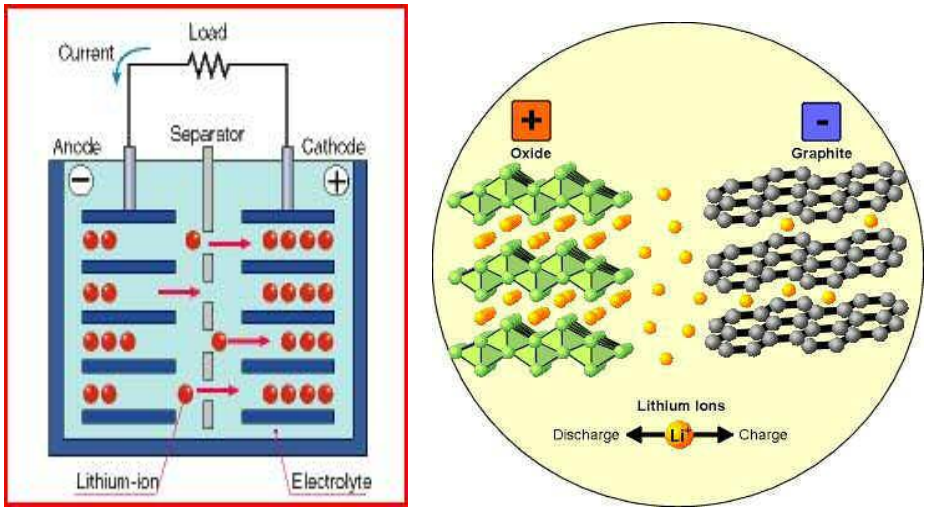

Figure 1.4 - During the charging process of the Li-ion battery, Li ions are extracted from the cathode and travel to the anode as electrons pass through an external circuit. At the anode side, the ions are intercalated or inserted in between layers of graphite atoms. When discharging, the process is reversed, with now the lithium ions being intercalated into oxygen layers of the cathode as useful electrical energy is produced. Not shown are current collectors that are in contact with the electrodes.

1.3 The Lithium-Ion Polymer Battery

As an outgrowth of the Li-ion battery, rechargeable Li-ion polymer batteries began being developed in 1996 in efforts to improve performance criteria such as energy density [16]. Such batteries use either a gel polymer electrolyte, i.e. a solidified liquid electrolyte, or a solid polymer electrolyte in which no liquid component exists. Li-ion polymer batteries are desirable because the possibility of liquid electrolyte leakage is reduced or eliminated, and they are capable of being shaped into almost any form. They provide cost and performance advantages over other kinds of batteries. Gel and solid polymer electrolytes replace the traditional porous separator that is soaked with the liquid electrolyte. The polymer electrolytes require good interfacial contact with the electrodes, high cation mobility, reasonable ionic conductivity, low electronic conductivity, good mechanical properties, and also safety and ease in processing [17, 18].

Gel polymer Li-ion batteries incorporate an organic liquid electrolyte that is held together by a polymer matrix, i.e. the liquid electrolyte is trapped by the polymer, typically PVDF-HFP, or poly(vinylidene) fluoride-co-hexafluoropropylene [12]. Gel polymers tend to have almost liquid-like ionic conductivities with solid-like durability [19]. The microporous separator film used in conventional Li-ion batteries is substituted by the gelled polymer electrolyte. The cells are therefore similar in their composition and chemistry to their liquid electrolyte counterparts. Not only are the gel polymer cells safe due to less chance of electrolyte leakage, but they are also lightweight which simplifies processing and packaging [12]. Physically, gel polymer electrolytes can be somewhat sticky

yet flexible and thin allowing for portable applications, i.e. PDAs and cell phones. Li-ion gel polymer cells can take a cylindrical, prismatic, or a coin type shape.

In Li-ion solid polymer batteries, the electrolytes consist of lithium salts dissolved into polymers [20]. The original design of these batteries dates back to the 1970s and uses a dry solid polymer electrolyte instead of a liquid electrolyte [21]. Armand et al. reports that solid polymer electrolytes bring together the benefits of solid state electrochemistry with the ease of processing inherent to plastic materials [22]. The internal structure of a solid polymer cell can be configured to almost any size and thickness, which makes the solid polymer Li-ion a batter candidate than liquid Li-ion batteries for electric vehicles and other large-cell applications [23]. The solid polymer electrolytes are very flexible. In comparison to gel polymer batteries, the solid polymer batteries have advantages including greater design flexibility, greater stability with lithium metal, and the elimination of intricate packaging to support the liquid phase. After completion of synthesis, the solid polymer electrolyte resembles a plastic-like film. Solid-polymer Li-ion cells have demonstrated safety under harsh conditions and are environmental friendly. Ionic conductivities for solid polymer electrolytes are generally not as high as for liquids or gels but are reasonably high for temperatures above 60^{o}C, and thus such electrolytes may not be suitable for portable room temperature applications [24]. Solid-polymer Li-ion cells are rolled into sheets and can support cost-effective, smooth and efficient productions. Li-ion cells, on the other hand, have winding and canning processes involved which are time-consuming and expensive [23].

Lithium-ion polymer batteries are gaining ground in the race for finding suitable alternative energy devices. Improvements in conductivity, capacity gain, and performance are growing fast as research and development progresses. Contained herein are two independent studies carried out on various gel electrolytes. In one of the studies, the applications of the gels were specifically targeted for lithium metal/air batteries. Lithium metal/air batteries use air as the cathode making it theoretically possible to have a high energy density that is only limited by design. These batteries will be discussed in more detail in Chapter 4. Both projects included understanding the effects of employing ionic liquids, which are molten salts at room temperature and possess desirable qualities. A study was also conducted on an interesting kind of solid polymer electrolyte, whose structure consists of block copolymers, for applications to NASA technology. Background information of the materials is given in Chapter 4. The lithium-ion polymer battery materials are listed under the following headings in that chapter:

(4.1) "NASA Rod-Coil Block Copolymers as Solid Polymer Electrolytes"

(4.2) "Gel Polymers Incorporating LiBETI Salt and Ionic Liquids"

(4.3) "Gel Polymers Incorporating Li_{13}TFSI/P_{13}TFSI Salt and Ionic Liquids"

1.4 A Brief History of the Fuel Cell

The underlying mechanism of a fuel cell was originated by English physicist William Grove (1811-1896). While a professor of experimental

philosophy, he befriended well-known physicist Michael Faraday (1791-1867), who was able to relate the phenomenon of magnetism to electricity through his law of electromagnetic induction. Faraday also conducted research in electrolysis. Electrolysis is the process by which electric current passes through an electrolyte to cause positive ions to move to the cathode and negative ions to move to the anode [25]. It can be used on water to produce hydrogen gas by separating hydrogen from oxygen. Grove was able to reason that reversing electrolysis on water could generate electricity from the reaction of hydrogen with oxygen to form water. He built what is considered to be the first fuel cell in 1839, but it provided little electricity (See Figure 1.5) [3,26].

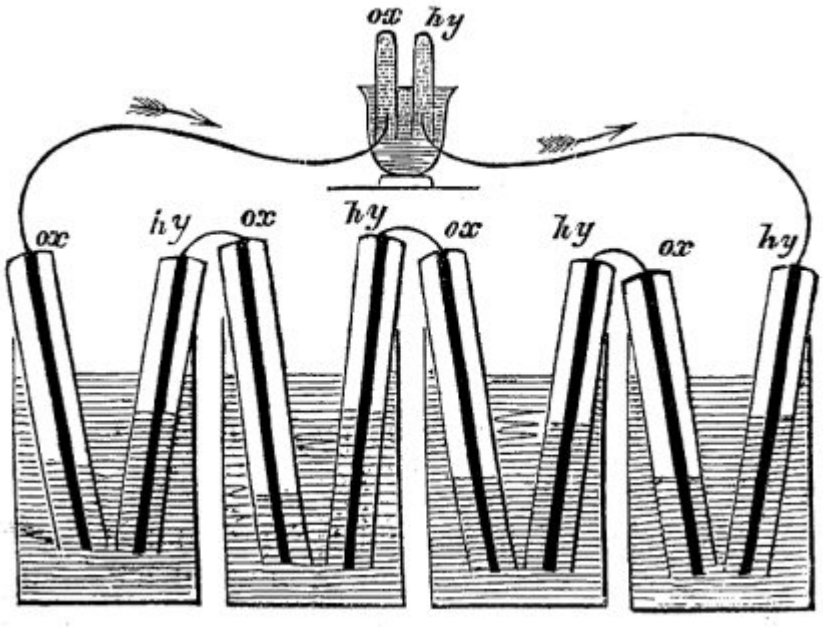

Figure 1.5 - William Grove's Fuel Cell.

Work with fuel cells was not too active until 1889 when a British Scientist, Ludwig Mond, and his associate Charles Langer, repeated the earlier work of Grove's which included employing dilute sulfuric acid as the electrolyte. In fact, they were the first to call the device the "fuel cell," and they tried being more pragmatic by replacing oxygen with air and hydrogen with impure industrial gas obtained from coal. Unlike a battery, fuel is actually stored outside the fuel cell. However after achieving 1.5 Watts at 50% efficiency, they abandoned the project because of the high cost of platinum catalysts used to oxidize hydrocarbons at the electrodes. In 1896 an American engineer by the name of J.J. Jacques constructed the largest fuel cell system at the time, which operated for as long as 6 months at a time. Jacques is also credited with being the first to propose the idea that a fuel cell could provide electricity for domestic use [3].

In 1959, engineer Francis T. Bacon (1904-1992) and his coworkers demonstrated a practical 5 kW unit with enough power to run a 2-ton capacity forklift truck. Two months later in October, Allis-Chalmers Manufacturing Company demonstrated the first fuel-cell powered vehicle, a 20-horsepower tractor [3].

In the early 1960s, NASA discovered that fuel cells were suitable sources of electric power for space flights of up to 14 days (See Figure 1.6). Rechargeable batteries were inefficient, as they required large and often cumbersome photovoltaic arrays. Perhaps most significantly, a fuel cell system which ran on liquid hydrogen and liquid oxygen produced about 8 times as much power per weight (~1.6 kWh/kg), compared to 0.2 kWh/kg being supplied by the best

batteries then available [3]. In the 1980s, fuel cells provided electric power on board space shuttles. As a bonus, ultra pure vapor produced by the cell served as drinking water for the astronauts.

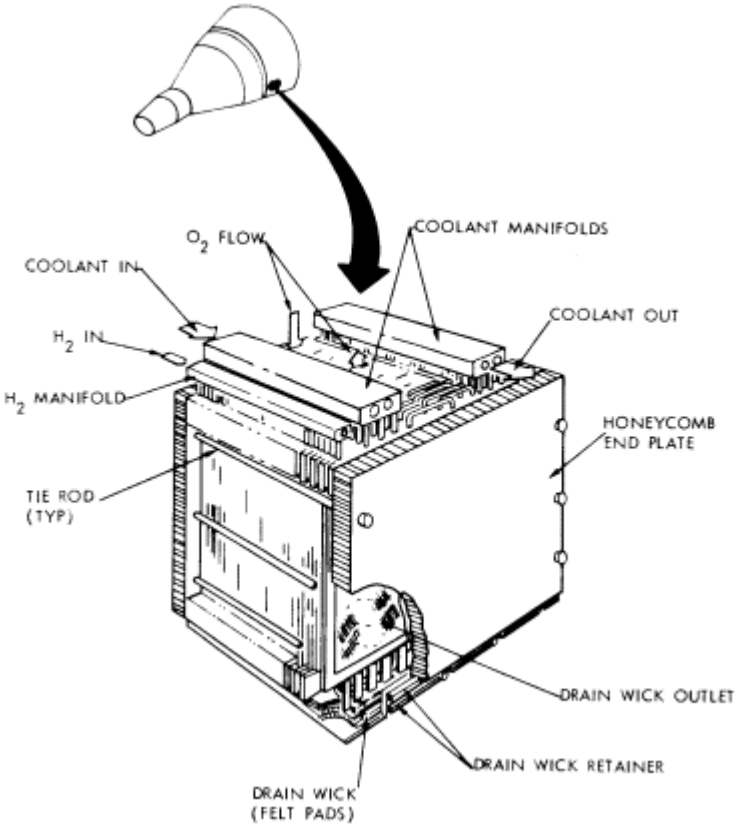

Figure 1.6 – Shown is a sketch of a fuel cell stack and its location in the spacecraft adapter section [27].

In the late 1960s and early 1970s, the fuel cell community faced challenges as small natural gas fuel cells were being developed for home use. Fuel cells were deemed not so successful for terrestrial applications. The use of hydrogen fuel required high temperatures and pressures when used with relatively cheap nickel catalysts in an alkaline fuel cell (i.e. consisting of aqueous alkaline

solution such as potassium hydroxide), and alkaline fuel cells required very pure hydrogen. In addition, dirty commercial fuels were used as opposed to pure hydrogen. To make matters worse, government funding for fuel cells slowed as deadlines were not met.

NASA's large involvement in the advancement of fuel cell technology helped to renew interest in fuel cell development worldwide in the 1990s. A slew of programs were being funded in the United States, in Europe (including the former Soviet Union), and in Japan to design and build various types of fuel cells – molten carbonate, solid oxide, phosphoric acid, alkaline, solid polymer, direct methanol. These were classified as such according to the type of electrolyte employed and also the nature of the hydrogen fuel, i.e. reformed or directly fed.

An experimental phosphoric acid fuel cell power plant was built in New York City Fire Department in the early 1980s. With all the fuel cell stacks in place, they were found no to function properly. These fuel stacks had been in storage for 7 years and were determined to have a limited shelf life because of the chemical interaction between the phosphoric acid electrolyte and the graphite bipolar plates between the cells. Despite this misfortune, the plant showed that it was possible for a fuel cell generating station to comply with the demands of the local authorities. In August of 1991, an 11 MW plant was developed in Tokyo. It produced 10,246 MWh of electric power in 1414 hours of operation. The measured efficiency exceeded the design value. Sometime in 1993, United Technologies Corporation began building 200-kW phosphoric acid fuel cell

plants. About 200 of these plants have been deployed, all over the world, at a rate of about two dozen a year since the program launched [3].

It was assumed that small fuel cells, for electric vehicles in particular, would be commercialized first and that larger multi megawatt stationary fuel cells would follow but that obviously wasn't the case. Part of the reason for the way things played out is that big stationary fuel cells do not encounter the resistance of strong lobbying groups such as automobile manufacturers who may prefer to use the internal combustion engine for as long as it remains profitable [3].

In the mid 1990s, companies began developing small scale fuel cells in order to power portable device such as cellular telephones, laptop computers, and electric hand tools. In 1996, small proton exchange membrane fuel cells (PEMFCs) emerged. These fuel cells incorporate polymer electrolyte membranes that when hydrated facilitate proton transport from the anode to the cathode side of the cell. The PEMFCs operated in the 40-125 Watt range. Larger PEMFCs are currently being developed to produce power in the kilowatt range. PEMFCs also require high temperature operation (above 120^{o}C) for peak performance.

Fuel cells have been around for over 150 years. Fuel cells can provide a great deal of electrical energy enough to power our homes and cars as well as portable electronic devices. The fuel capacity is only limited by size of the fuel container. Concerning the effects on our environment, fuel cells release undamaging byproducts such as water and heat during operation. While greenhouse gases such as CO_2 are produced as well when using a hydrocarbon fuel, these tend to be in smaller amounts due to the higher thermodynamic

efficiency of a fuel cell compared to a heat engine. The high cost in manufacturing fuel cells has, in part, slowed its progress but that is now changing. The advancement of fuel cell technology also largely depends on improving critical properties of the polymer electrolyte membranes which comprise fuel cells. Some key aspects to consider in developing electrolyte membranes for higher performing and more efficient fuel cells are mechanical integrity, thermal stability, and ionic conductivity.

1.5 The Proton-Exchange Membrane Fuel Cell (PEMFC)

Proton exchange membrane fuel cells (PEMFCs) typically use reformed hydrogen as a source of fuel to provide hydrogen ions, or protons, which are transported from the anode side to the cathode side of the cell. Located between the electrodes is a polymer electrolyte membrane, and it allows proton flow while also preventing mixing of hydrogen from the anode with oxygen, the oxidizing agent, at the cathode. As the protons pass through the membrane, free electrons flow through an external circuit and provide useful energy to the device of interest (See Figure 1.7) [28]. As in the Li-ion battery, it is thus generally the case that enhanced output power can be achieved through increased ion (in this case, proton) conduction. PEM fuel cell stacks have been shown to generate power densities as high as 2.5 Watts per square centimeter [29]. PEMFCs typically operate in the temperature range of $60^{o}C$ – $100^{o}C$. However, PEMFCs can operate optimally at higher temperatures (above $120^{o}C$) given that the membranes are moderated to retain water better. High temperature fuel cell operation offers

several advantages including greater proton kinetics, better water management, and also the minimization, or elimination, of poisoning on Pt-based catalyst layers in the cell due to CO impurity in the fuel.

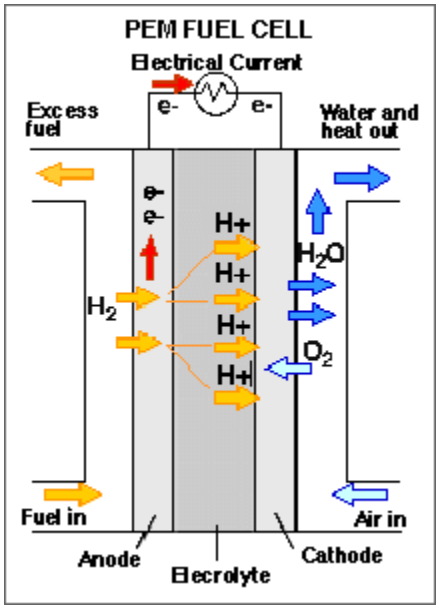

Figure 1.7 – Hydrogen gas is pumped into the anode. A Pt based catalyst at the anode reacts with the hydrogen causing it to break up into hydrogen atoms and then into electrons that move through an external circuit while hydrogen ions that flow through the membrane. At the cathode, the hydrogen ions meet up with the electrons and combine with oxygen from the air with the help of another Pt-based catalyst. Water and heat are released as byproducts.

Possible PEMs need to meet certain requirements for inclusion into a fuel cell. These include electrochemical stability under operating conditions as well as during cell assembly, mechanical and dimensional stability, compatibility with other fuel cell components especially with electrodes, low cost, and high proton

conductivity. Proton conductivity is a key property of the polymer electrolyte membrane, and it directly affects the performance of a fuel cell. Different factors affect conductivity with the most important probably being the ability of the membrane to take in and retain water.

Proton exchange polymer membranes were used as electrolytes in fuel cells beginning in the 1950s. Several membrane candidates existed early on. These membranes suffered from poor stability. The Nafion membrane was developed in the 1960s by DuPont [30]. Nafion, did show vast improvements in stability and performance, and it is currently the most commercially used membrane in PEMFCs. Nafion experiences efficiency loss at higher temperatures mostly due to water loss and is rather expensive to synthesize. The choice of the membrane can affect the total cost of a fuel cell greatly, 2-18% of the total cost [31]. The search for cost effective and better performing PEMs (than Nafion) has led to the research and development of alternative materials in institutions around the world.

In the studies undertaken herein, the Nafion membrane was examined for use in PEMFCs as well as DMFCs, or direct methanol fuel cells. DMFCs are really a subcategory of PEMFCs except that they use methanol as a fuel that is directly fed into the anode. The DMFC is preferable for high temperature operation [29]. Also studied were two kinds of novel polymer membranes that rival Nafion as PEMs. These materials were supplied by the Air Force Research Laboratory. They are non-fluorinated and fluorinated SPTES (sulfonated

poly(arylenethioether) sulfone) membranes In Chapter 4, regarding the background of materials studied, the membranes are listed as:

(4.4) Nafion Membrane for Use in PEMFCs.

(4.5) SPTES and 6F-SPTES Copolymer Membranes for Use in PEMFCs.

1.6 Introducing Nuclear Magnetic Resonance (NMR) Spectroscopy

We can apply the technique of nuclear magnetic resonance (NMR) spectroscopy as a noninvasive tool to aid in the development of better performing and more efficient lithium-ion polymer batteries and fuel cells. Nuclear magnetic resonance (NMR) spectroscopy is an experimental means by which one can extract useful information regarding the structural and dynamical properties of a certain material, namely the electrolyte. Through the absorption of electromagnetic radiation while in the presence of a strong magnetic field, atomic nuclei composing a substance undergo changes in their magnetic behavior. The experimentalist makes use of a net magnetization arising from the collection of nuclei, and analyzes the way in which this magnetization varies in strength and orientation over time. By implementing various radiofrequency pulse techniques, we can manipulate the magnetization to better understand the local environments of nuclei and characterize the motion of different molecular groups.

NMR can permit us to determine, to a fairly good degree of accuracy, the translational mobility of a molecular or ionic species through a permeable

medium as in a polymer electrolyte. The quantity described is known as the self-diffusion coefficient, and it is intimately connected to the ionic conductivity. NMR can also guide us into finding electrolyte materials that possess mechanical integrity as well as thermal stability.

In the electrolyte materials investigated, the self-diffusion coefficients of ions and molecules were measured. Other physical quantities were also measured as a function of temperature. These include the spin-lattice relaxation time, T_1 and the linewidths of absorption spectra. T_1 is related to the lifetime of excited nuclei and informs of the local environment of ions and molecules as well as their short range motion. The linewidth of an absorption peak is defined as the full width of the peak at half of its height, and the integrated peak intensity is proportional to the concentration of excited nuclei giving rise to the peak. The nuclei investigated were ^{7}Li, ^{19}F, and ^{1}H. Again, the quantities of interest in the studies contained included

(A) the self-diffusion coefficient

(B) T_1

(C) linewidth

Chapter 2: A Historical and Theoretical Background of NMR

2.1 Historical Development of NMR

During the mid 1940s, two physicists, Felix Bloch and Edward Mills Purcell, independently discovered the phenomenon arising from placing nuclei with non-zero spin angular momentum in a static magnetic field and subjecting them to electromagnetic radiation. Nuclear magnetic resonance, as it had been detected, made use of the energy difference between the nuclear spin states of an atom to be the precise amount of electromagnetic energy required for inducing transitions between lower and higher energy states. Only a certain frequency of electromagnetic radiation could therefore excite a particular nucleus with spin that experiences an applied magnetic field. In 1952, both Bloch and Purcell shared the time-honored Nobel Prize in physics for their revolutionary work in nuclear magnetism [33]. Bloch and Purcell based their observations on a branch of spectroscopy known as continuous wave (CW) NMR, in which an appropriate range of radiofrequency (RF) waves slowly sweeps through a sample containing the pertinent nuclei while the external magnetic field is kept fixed. In some cases, the field is swept while a source of RF wave is kept fixed. The CW NMR spectrometer instrument consists of a recorder which is synchronized to the RF source to record the resulting spectrum [34].

For some time, CW NMR proved very useful as an analytic tool in investigating the structure of organic molecules (i.e. ethanol) by probing the local

bonding environments of nuclei. It wasn't really until 1966, however, that a new method of NMR spectroscopy began to emerge and slowly replace CW NMR as the most commonly used NMR technique. Fourier Transform (FT) NMR was being brought to the forefront by the efforts of Richard Ernst and others. Instead of slowly varying and continuous RF irradiation, Ernst implemented short intense RF pulses [33]. In doing so, he was able to generate a band of frequencies that could essentially excite all the nuclei of a given species at once. A short pulse on the order of microseconds provided a frequency band on the order of MHz. The observed signal would be called an FID for Free Induction Decay). The FID is a signal in the time domain that could be Fourier transformed to give an NMR signal in the frequency domain. Advantages of FT NMR over CW NMR include faster data collection (less time for scans) and greater signal to noise ratio. The first FT-NMR spectrometer was introduced in 1970 [35].

Liquids were primarily being studied by NMR in the early years. Solid samples would often give broad and featureless signals. However, in the period of 1965-1975 methods incorporating sample spinning to achieve line narrowing and FT pulse techniques were being developed [35]. The technique became known as MAS, or magic angle spinning. It involves spinning the sample through a certain angle with respect to the external field, which acts to average out interactions that would otherwise give rise to line broadening.

Multidimensional NMR sprung about in 1971 as the first 2D NMR experiment was conducted, known as a COSY or correlation spectroscopy. Until then, NMR had used the 1D time (acquisition time dependent) signal to provide a

signal in 1D frequency space. In 2D NMR, another time, known as the evolution time, is varied (i.e. the time between pulses). A FT of the FID along the acquisition time is made first, followed by a second FT along the evolution time to produce a stacked plot of peak intensity. One axis of the plot corresponds to the frequency from the first time variation (acquisition time) and the other from the second variation in time [36]. In 1976, Richard Ernst executed and published the first 2D COSY experiment [37]. Later, 3D and 4D NMR experiments were being performed. Ernst also developed a switched time domain gradient (changing magnetic field with position) method. In the early 1970s, Paul Lauterbur realized that with a magnetic field gradient, information contained in the signal distortions could be used to create 2D images of the sample's internal structure [35]. Peter Mansfield expanded on Ernst's work and developed a phase encoding technique for image collection. Mansfield published the first cross-sectional image of a human body part and this then became the crux of MRI, or magnetic resonance imaging, technology [38]. In 1991, Ernst won the Nobel Prize in Chemistry. Two years later, Peter Mansfield and Paul Lauterbur won the Nobel Prize in medicine for their work in developing MRI. Today, NMR continues to be widely used as one can find various pulse techniques being used to understand biological systems, organic compounds, quantum computation, and also materials for advanced energy research.

2.2 NMR Theory

2.2.1 Nuclear Spin, Energy Quantization, and Resonance

Let us consider a nucleus of spin $I = \frac{1}{2}$ as in that of the hydrogen atom. Since the nucleus has the property of spin and is positively charged, there exists a nuclear magnetic moment $\vec{\mu}$, which may be expressed by the following

$$\vec{\mu} = \gamma \vec{I} \tag{2.1}$$

where γ is the gyromagnetic ratio (a constant dependent upon the type of nucleus being observed), $\vec{I}$ is the spin angular momentum, which is quantized in units of $\hbar$, or Planck's constant divided by 2π. Nuclei with no net spin and therefore no magnetic moment are not detectable by NMR. Such nuclei include ^{16}O and ^{12}C as these contain an equal amount of protons and neutrons.

When a hydrogen nucleus is immersed in a static and uniform magnetic field $\vec{B}_0 = B_0 \hat{k}$, the energy of the nucleus splits into distinct levels (See Figure 2.1). The energy can take on $2I+1$ different values according to the magnetic quantum number m, where $m = -I, -I+1, \ldots, I-1, I$. In the case of our nucleus with $I = 1/2$, $m = \frac{1}{2}, -\frac{1}{2}$, indicating that two energy levels are present, where one corresponds to $m = \frac{1}{2}$ (a lower energy state) and the other to $m = -\frac{1}{2}$ (a higher energy state). The energy of the interaction between our nucleus and the external field can be written as

$$E = -\vec{\mu} \cdot \vec{B}_0 = -\mu B_0$$

$$E = -\gamma I_z B_0 \qquad (2.2)$$

where I_z can take on the value of $\frac{1}{2}\hbar$ or $-\frac{1}{2}\hbar$ (recall the I_z operator yields eigenvalues of $m\hbar$).

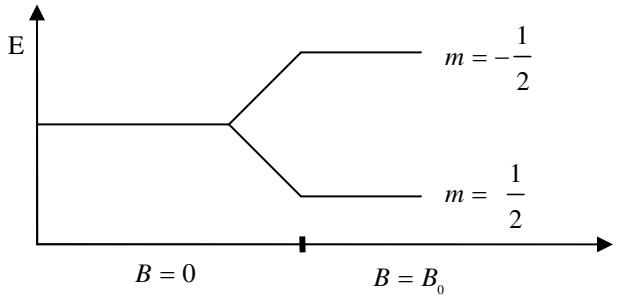

Figure 2.1- Energy levels of spin-1/2 nucleus in a uniform magnetic field.

From a classical perspective, $\vec{B}_0$ tends to align the nuclear dipole moment in its direction (or along the positive z-axis) analogous to the way a compass needle deflects in the direction of the earth's magnetic field. The dipole moment however does not remain stationary in the external field. Instead, it precesses about the field with a characteristic frequency f_o, known as the Larmor frequency (See Figure 2.2). The precession occurs because a torque $\vec{\tau}$ is exerted on the dipole moment due to $\vec{B}_0$. $\vec{\tau}$ is directed perpendicular to both $\vec{\mu}$ and $\vec{B}_0$ ($\vec{\tau} = \vec{\mu} \times \vec{B}_0$), and therefore causes the angular momentum of the nucleus to change with time. The dipole moment is left to precess at the Larmor

frequency f_o, or angular frequency $\omega_0 = 2\pi f_0$, indefinitely. The Larmor frequency is uniquely valued for each different nucleus.

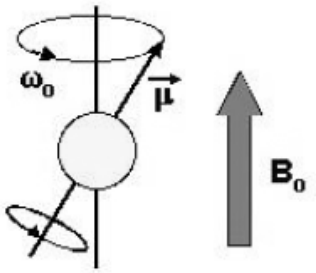

Figure 2.2 – Dipole moment in a static field.

For the phenomenon of resonance to occur and the nucleus to transition into a higher energy state, the nucleus must absorb a photon of energy equivalent to the energy difference ΔE between the upper and lower energy levels. Mathematically, we write

$$E_{photon} = \Delta E \tag{2.3}$$

$$\hbar\omega_0 = 2\mu B_0 \tag{2.4}$$

Substituting for μ in terms of I_z in equation (2.4) and dividing through by $\hbar$, we obtain the following resonance condition

$$\omega_0 = \gamma B_0 \tag{2.5}$$

We learn that the frequency of the electromagnetic radiation to excite a nucleus is proportional to the strength of the external field. Furthermore, this required frequency of electromagnetic oscillation f_o is in fact equal to the Larmor frequency of precession for the dipole moment.

We can liken the situation of nuclear resonance to that of a driving force acting with a particular frequency on a spring system having its own natural frequency. Resonance is achieved when the frequencies match, and as a result we observe large amplitude oscillations. In a somewhat similar manner, an absorption line spectrum is observed in NMR spectroscopy when the frequency of electromagnetic radiation matches or is near the Larmor frequency for a certain class of nuclei (not having a perfectly uniform $\vec{B}_0$ and the existence of local magnetic fields will slightly shift ω_0). The integrated intensity of the NMR signal is proportional to the concentration of nuclei being excited.

2.2.2 N Magnetic Dipoles and the Magnetization

Let us now extend our nuclear system to include N hydrogen nuclei (or protons) as in a sample of water, where N is somewhere on the order of Avogadro's number. The individual nuclear moments are randomly oriented, but we can conceive of a net magnetic moment by summing all the moments over the entire volume of our sample, or

$$\vec{M} = \sum_{i=1}^{N} \vec{\mu}_i \tag{2.6}$$

where $\vec{M}$ is the magnetization vector and is directed in some way.

When the sample is placed in a uniform field $\vec{B}_0 = B_0 \hat{k}$, as before, not all the spins (moments) align with the field. The population ratio of spins follows a

Boltzmann distribution, which is related to the energy and temperature of the nuclear system. We have

$$\frac{N_{\uparrow}}{N_{\downarrow}} = e^{\frac{\Delta E}{kT}} \tag{2.7}$$

where $N_{\uparrow}$ is the number of spins aligned with the field, $N_{\downarrow}$ is the number of spins aligned against it ($N = N_{\downarrow} + N_{\uparrow}$), k is Boltzmann's constant (= 1.38×10^{-23} m^2kg/s^2K) and T is temperature. The difference in population, or simply $N_{\uparrow} - N_{\downarrow}$ is typically very small, about 1 part in 10^5, but this difference becomes larger with increasing strength of the external field or lowering temperature [39].

Since more spins point in the direction of the external field than against it, the sample will be slightly magnetized along the longitudinal direction, or the z-axis. Therefore the magnetization $\vec{M}$ is in the direction of the field and precesses about it with the characteristic Larmor angular frequency ω_0. The individual spins themselves actually precess about either the positive or negative z-axes with a frequency at or near ω_0 or - ω_0, respectively. In the rotating frame, that is, a frame that rotates with respect to the z-axis at ω_0 , $\vec{M}$ lies along the z-axis and is termed the equilibrium magnetization $\vec{M}_0 = M_0 \hat{k}$. With the magnetization along the longitudinal direction, the spins will have reached a state of thermal equilibrium with their surroundings (or the lattice). Also, the population of spins will have been distributed as described in equation (2.7).

The equilibrium magnetization may be written as

$$M_o = N_{\uparrow}(\mu) + N_{\downarrow}(-\mu)$$

M_0 may be expressed more explicitly by considering the partition function of an N spin-1/2 particle system (involves taking the sum of all the Boltzmann factors), finding the average energy of the system, and solving for M_o. One then finds

$$M_0 = -N\mu \tanh\left(\frac{\mu B_0}{kT}\right) \tag{2.8}$$

where T is absolute temperature [40].

The energy of our N particle system in the external field (neglecting all other interactions for now) can be written as

$$E_N = -M_0 B_0$$

or

$$E_N = N_{\downarrow}\mu B_0 - N_{\uparrow}\mu B_0 \tag{2.9}$$

2.2.3 Perturbation of a Nuclear System and Relaxation Processes

In pulse NMR, a radiofrequency pulse (essentially a burst of energy) is applied to a nuclear system that's in its equilibrium state. The RF pulse consists of a continuous band of frequencies lying in the range of the Larmor frequency of precession. The sample of interest is placed inside an inductor, or a coil, that is situated perpendicular to $\vec{B}_0$. In the transmission of the RF pulse of frequency ω_0, alternating current flows along the turns of the coil. An oscillating magnetic field $\vec{B}_1 = B_1 \cos(\omega t)\hat{\imath}$ is generated. $\vec{B}_1$ perturbs the nuclear system as it exerts a

separate torque on $\vec{M}_0$ (as seen from the rotating frame), and $\vec{B}_1$ is much weaker than $\vec{B}_0$. Depending on the strength of $\vec{B}_1$ and the duration of the pulse, $\vec{M}$ will tilt through a certain angle with respect to $\vec{B}_0$. This tilt angle is defined by the following relation

$$\theta_t = \gamma B_1 t_p \tag{2.10}$$

where t_p is the duration of the pulse. In usual NMR experiments, t_p lasts somewhere from 1 to 50 μs [41]. Full excitation occurs when $\vec{M}$ is rotated $\frac{\pi}{2}$ radians or 90° onto the transverse plane, or onto the rotating plane x'y'. In the rotating frame, $\vec{M}$ actually rotates about the $\vec{B}_1$ or the x' axis with angular frequency $\omega_1 = \gamma B_1$ The spin population becomes equalized immediately after the application of the $\frac{\pi}{2}$ pulse . We then turn off the secondary field $\vec{B}_1$, and allow for relaxation of the magnetization back to equilibrium.

We can gain better insight as to what happens after the RF pulse is given if we look at the behavior of isochromats. An isochromat is a group of spins in which all the spins precess at the same frequency. With the magnetization orthogonal to $\vec{B}_0$, there are different isochromats that precess at different rates due to an inhomogeneous $\vec{B}_0$ field across the sample and local magnetic effects between the isochromats. In other words, each isochromat experiences a slightly different magnetic field. In the rotating frame, there is a dephasing or fanning out

of the isochromats since some precess faster than ω_0 and some slower [42]. As a result, there arises transverse relaxation of the magnetization, and the transverse component of the magnetization decays (See Figure 2.3).

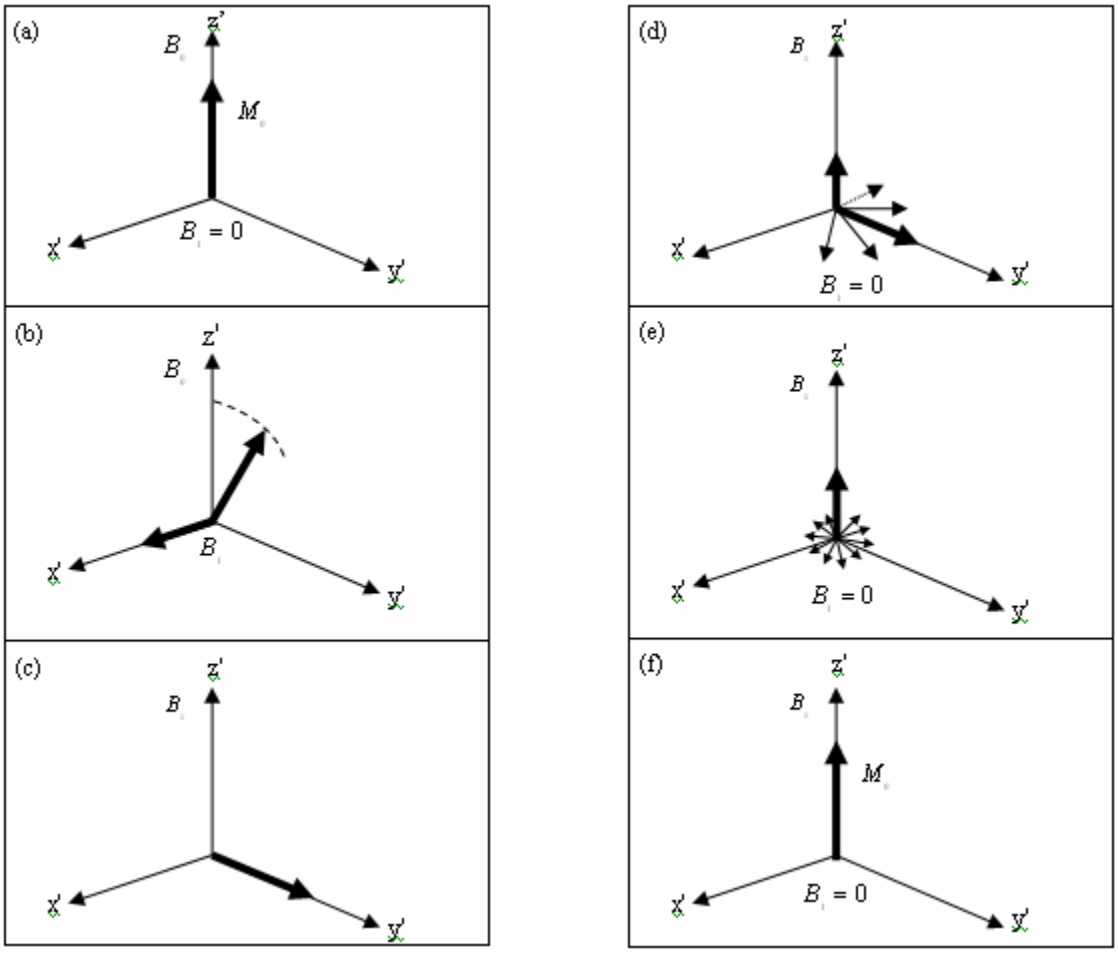

Figure 2.3 – (a) In the rotating frame, the magnetization is aligned along B_0. (b) A secondary field B_1causes the magnetization to flip. (c) The magnetization lies in the transverse direction. In (d) and (e) B_1=0, the spins dephase, and the transverse component of magnetization decays until (f) the equilibrium magnetization is recovered.

The loss of coherence of the transverse magnetization induces a voltage in the coil. A time-domain signal is thus obtained. The signal is coined the FID, or Free Induction Decay, and it is observed immediately after a $\frac{\pi}{2}$ pulse is applied. The FID originates from of nuclei resonating at or near the Larmor frequency. A Fourier transform of the FID allows us to analyze a spectrum of peak(s). The amplitude $A(\omega)$ in the frequency domain of an absorption peak can be written as

$$A(\omega) = \int_{-\infty}^{\infty} A(t) e^{-i\omega t} dt$$

where $A(t)$ is the time-dependent intensity of the FID. The decay of the FID is usually exponential in time, and the Fourier transform of such a time response correspondingly gives rise to a Lorentzian lineshape in the spectrum**.** The lineshape depends on the rate at which energy is exchanged between nuclear spins in the isochromats (See Figure 2.4).

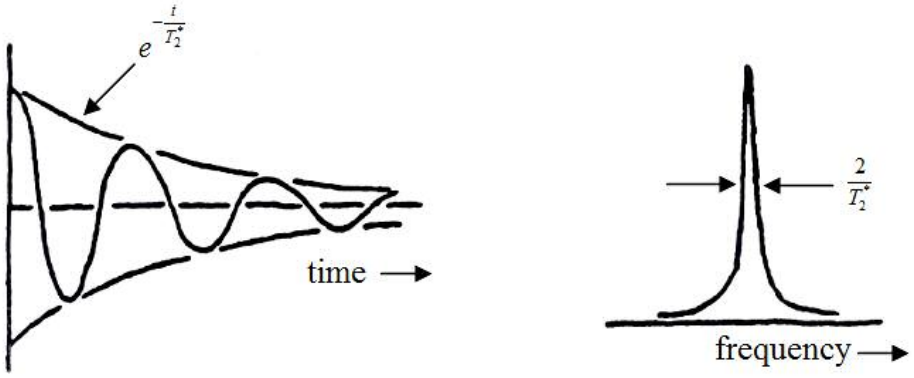

Figure 2.4 – An FID and its Fourier transform in the frequency domain.

The amplitude of the transverse magnetization falls off at the rate of $e^{\frac{-t}{T_2^*}}$, where T_2^* is the time constant pertaining to the dephasing of the isochromats. T_2, or the spin-spin relaxation time, however, is related to transverse magnetization decay along one particular spin isochromat. T_2 is the time during which the spins in a single isochromat remain in phase with each other. T_2* and T_2 are related in the following way

$$\frac{1}{T_2 *} = \frac{1}{T_2} + \gamma \Delta B_0 \tag{2.11}$$

where ΔB_0 is the external field inhomogeneity [9]. Equation (2.11) is only true for nuclei with I=1/2 or nuclei with I>1/2 having no quadrupole effects. If ΔB_0 is negligible, then the two time constants are approximately equal, and therefore each isochromat relaxes by approximately the same amount. The linewidth, which is the full width of an absorption peak at half of its maximum height, is inversely proportional to T_2*. If the spins exchange energy quickly (i.e. if spins interact quickly), then the transverse magnetization decays rapidly. Consequently, one may observe a significant contribution to the beginning of the FID as well as broad lines in the spectrum. When T_2* is fairly long, however, narrow lines in the spectrum are observed. For the spectral studies conducted herein, the difference between T_2 and T_2* can be considered to be rather small since our external field was relatively homogeneous, and the nuclei were in relatively mobile environments.

There are actually two relaxation mechanisms at play after the application of a $\frac{\pi}{2}$ pulse. Thus far, we've discussed relaxation in the transverse plane, but there is also a longitudinal relaxation process attempting to recover the equilibrium magnetization $\vec{M}_0$. In the case of longitudinal relaxation, the nuclear spins give up the energy they received upon excitation back into the lattice. The rate of this energy transfer for thermal equilibrium to be fully restored is measured by T_1, or the spin-lattice relaxation time. T_1 can also be viewed as the lifetime of the nuclei in their excited states. The value of T_1 depends on many factors as one might imagine, which include the size of the molecules these nuclei are in, molecular rotation, paramagnetic impurities, nuclear dipole-dipole interaction, and more. T_2 is generally less than or equal to T_1. In rigid solids, T_1 is usually much longer than T_2 since molecular motion is more limited [39]. In addition, T_1 actually indicates how often you can repeat an NMR experiment, which is crucial for garnering high signal resolution (or high signal-to-noise ratio) by signal averaging.

2.2.4 Classical Magnetization

The equations relating the evolution of the magnetization to both T_1 and T_2 can be derived classically. Taking the time derivative of equation (2.1), we have

$$\frac{d\vec{\mu}}{dt} = \gamma \frac{d\vec{I}}{dt} \tag{2.12}$$

The right hand term of the equation is the gyromagnetic ratio multiplied by the time derivative of the spin angular momentum. We know that the total time derivative of the angular momentum equals the net torque acting on the nuclear system, or

$$\frac{d\vec{I}}{dt} = \vec{\tau} \tag{2.13}$$

Rewriting equation (2.12) in terms of torque, we see that

$$\frac{d\vec{\mu}}{dt} = \gamma\vec{\tau} \tag{2.14}$$

$$\frac{d\vec{\mu}}{dt} = \gamma(\vec{\mu}\, x\, \vec{B}) \tag{2.15}$$

for a magnetic moment μ in a magnetic field $\vec{B}$. For $\vec{\mu} \to \vec{M}$, we have

$$\frac{d\vec{M}}{dt} = \gamma(\vec{M}\, x\, \vec{B}) \tag{2.16}$$

Rewriting (2.16) in component form, we obtain

$$\frac{dM_x}{dt} = \gamma(M_y B_z - M_z B_y) \tag{2.17}$$

$$\frac{dM_y}{dt} = \gamma(M_z B_x - M_x B_z) \tag{2.18}$$

$$\frac{dM_z}{dt} = \gamma(M_x B_y - M_y B_x) \tag{2.19}$$

Equations (2.17), (2.18), and (2.19) are known as the generalized Bloch equations. The Bloch equation in (2.16) governs the motion of $\vec{M}$ in an applied

field $\vec{B}$. In thermal equilibrium, without incurring any pulses, $B_x = B_y = 0$. Our applied field lies purely along the z-axis. Equations (2.17), (2.18), and (2.19) then become

$$\frac{d M_x}{dt} = \gamma M_y B_0 \tag{2.20}$$

$$\frac{d M_y}{dt} = -\gamma M_x B_0 \tag{2.21}$$

$$\frac{d M_z}{dt} = 0 \tag{2.22}$$

Differentiating equation (2.20) and substituting in equation (2.21) we have

$$\frac{d^2 M_x}{dt^2} = -(\gamma B_0)^2 M_x \tag{2.23}$$

Similarly,

$$\frac{d^2 M_y}{dt^2} = -(\gamma B_0)^2 M_y \tag{2.24}$$

We can solve equations (2.23), (2.24), and (2.22) to arrive at the following

$$M_x(t) = M_x(0)\cos(\omega_0 t) \tag{2.25}$$

$$M_y(t) = M_x(0)\sin(\omega_0 t) \tag{2.26}$$

$$M_z(t) = M_z(0) = M_0 \tag{2.27}$$

where ω_0 is as usual 2π times the Larmor frequency. If we were to observe the magnetization in the x-direction, there would be an oscillation between $+M_x(0)$ and $-M_x(0)$ for all time. However, the oscillation is finite if we include the RF

field $\vec{B}_1$. After the $\frac{\pi}{2}$ pulse, the magnetization will decay in the transverse direction, and increase in the longitudinal direction. We need to modify the Bloch equations to incorporate the effects of $\vec{B}_1$ and relaxation. We will use a general expression for $\vec{B}_1$

$$\vec{B}_1 = B_1 \cos \omega t \hat{\imath} + B_1 \sin \omega t \hat{\mathrm{j}} \tag{2.28}$$

In the rotating frame, the total magnetic field is written as

$$\vec{B}_{rot} = B_0 \hat{k} + B_1 \hat{\imath}_{rot} \tag{2.29}$$

The Bloch equations, in the rotating frame, become the following

$$\frac{dM_x^{rot}}{dt} = M_y^{rot} \left(\gamma B_0 + \omega \right) - \frac{M_x^{rot}}{T_2} \tag{2.30}$$

$$\frac{dM_y^{rot}}{dt} = -M_x^{rot} \left(\gamma B_0 + \omega \right) + \gamma B_1 M_z - \frac{M_y^{rot}}{T_2} \tag{2.31}$$

$$\frac{dM_z^{rot}}{dt} = -M_y^{rot} \gamma B_1 - \frac{\left(M_z - M_0 \right)}{T_1} \tag{2.32}$$

where we see T_1 and T_2, and the term $\gamma B_0 + \omega$ is actually the z-component of the effective field in the rotating frame, or rather

$$\vec{B}_{eff} = \Delta B \hat{k} + B_1 \hat{\imath}_{rot} \tag{2.33}$$

where $\Delta B = \gamma B_0 + \omega$ [43].

Let us consider longitudinal relaxation, and also consider the following equation in the lab frame

$$\frac{dM_z}{dt} = -\frac{\left(M_z - M_0\right)}{T_1} \tag{2.34}$$

We can solve for M_z by separating variables and integrating,

$$\int_0^{M_z} \frac{dM_z}{M_0 - M_z} = \frac{1}{T_1}\int_0^t dt \tag{2.35}$$

obtaining the following

$$M_z(t) = M_0(1 - e^{\frac{-t}{T_1}}) \tag{2.36}$$

Equation (2.36) is telltale of how the longitudinal magnetization changes with time and depends on T_1. We take note that at t=0, M_z=0 and if we wait a sufficiently long time t, then we eventually recover M_0.

The Bloch equations are analogous to the equations of motion for a spinning top in a gravitational field with friction present. We can treat our nuclear system as a rigid magnetized body that is being influenced by a combination of magnetic fields.

2.2.5 Internal Interactions and Hamiltonians

The nuclei in a given volume of a substance can undergo many interactions. We have mentioned the Zeeman interaction, that is, the interaction of spins with an external magnetic field. Other interactions include scalar coupling, dipole-dipole interaction, quadrupolar interaction, and chemical shift interactions. These internal interactions perturb the basic resonance frequency ω_0 of the nuclei.

Each interaction can play an important role in what is observed in an NMR spectrum.

Scalar coupling, or *J* coupling, refers to the interaction between coupled nuclear spins in a given molecule. The interaction depends on the nature of the bonding between the nuclei. The Hamiltonian operator $\hat{H}_J$ underlying this interaction is

$$\hat{H}_J = \sum_j \sum_k 2\pi J_{kj} \hat{\vec{I}}_k \hat{\vec{I}}_j \tag{2.37}$$

where $k < j$ and J_{kj} is a coupling tensor (*J* is the coupling constant) and is a real 3x3 matrix with components J_{xx}, J_{xy}, J_{xz}, etc. J_{kj} is quoted in units of Hz. The strength of J_{kj} is in effect the ability of a nucleus to sense the spin state of another nucleus through the electrons in the bonds of the molecule. *J* coupling may result in a recognizable pattern of signal splitting for coupled nuclei of the same type. For our investigations, *J* coupling did not contribute a great deal to the spectra as the characteristic splitting was much smaller than the spectral linewidths for our materials, i.e. J-coupling is not usually absent in solids [39].

Another type of interaction is the dipole-dipole interaction, which arises from the interaction of magnetic nuclei, be they the same type or different, either through the molecule (intermolecular) or between molecules (intermolecular). It is a through-space interaction, and not dependent upon bonding. Dipole-dipole interaction is a short-range interaction since it falls off as the inverse of the distance between the dipoles cubed**.** The strength of this interaction depends on the relative orientation of the dipoles as well as the distance between them.

Dipole-dipole interaction is a strong interaction in rigid solids but not so much in mobile liquids because of rapid molecular reorientation, which averages out the interaction. For two nuclei *i* and *j* partaking in such an interaction, the Hamiltonian operator can be written as

$$\hat{H}_D = \frac{\mu_0 \gamma_1 \gamma_2 h^2}{16\pi^3}\left[\frac{\left(\hat{\vec{I}}_1 \cdot \hat{\vec{I}}_2\right)}{r^3} - 3\frac{\left(\hat{\vec{I}}_1 \cdot \vec{r}\right)\left(\hat{\vec{I}}_2 \cdot \vec{r}\right)}{r^5}\right] \tag{2.38}$$

where μ_0 is the magnetic permeability, $\vec{r}$ is the radial vector between the two spins. If we write out the Hamiltonian explicitly, the first angular dependent term turns out to be $I_{1z} I_{2z}(1-3\cos^2\theta)$, where θ is the angle from one spin's orientation to the line joining the spins, and this term embeds the second order Legendre polynomial, $P_2(\theta) = \frac{1}{2}(3\cos^2\theta - 1)$. The angular term is pretty much removed in liquids for reasons mentioned, but as for solids, a technique known as magic angle spinning (MAS) which spins the sample through a certain angle about the external field can serve to remove first order dipolar coupling. The "magic angle" is 54.7° (at which $P_2(\theta)$ vanishes) [33].

There exists a dipolar contribution to T_1. As a result of tumbling motion of the nuclei, fluctuating magnetic fields arise. The changing fields assist the relaxation of spins in regaining their equilibrium states, and thus affect T_1. There also exists a motional correlation time, τ_c at which the nuclei move by translation

or rotation. When $\frac{1}{\tau_c}$ is comparable to the Larmor frequency, T_1 approaches its minimum value, and spin-lattice relaxation is deemed efficient. Relative orientation of interacting molecules is also a key factor in determining relaxation rates. Frequencies of molecular rotation much lower than the Larmor frequency (as may be the case in the low temperature regime of a solid) give little contribution to relaxation and T_1 is long. In a high temperature regime, molecular motion may be too fast such that there is little time for the molecules to interact lending to inefficient relaxation. Once again, T_1 becomes longer [44].

Chemical shift anisotropy is another type of interaction worth discussing. Nuclei of the same isotope but in different chemical environments experience different shielding effects. In other words, a nucleus is partially shielded from the external field $\vec{B}_0$ due to magnetic fields being generated by the orbital angular momentum of the bonding electrons. The effective field that the nucleus actually is subject to can be expressed as

$$\vec{B}_{eff} = \vec{B}_0(1-\sigma) \tag{2.39}$$

where σ is a dimensionless shielding constant. The shielding constant σ is actually a second rank tensor, or

$$\sigma = \begin{pmatrix} \sigma_{xx} & \sigma_{xy} & \sigma_{xz} \\ \sigma_{yx} & \sigma_{yy} & \sigma_{yz} \\ \sigma_{zx} & \sigma_{zy} & \sigma_{zz} \end{pmatrix} \tag{2.40}$$

The modification of $\vec{B}_0$ entails a change in the resonance frequency. Now if the shielding effect is negligible, then $\vec{B}_{eff} \approx \vec{B}_0$.

For nuclei in a sample experiencing different chemical environments, NMR may allow us to distinguish between differences in this shielding, and in doing so, measure the quantity of chemical shift. The orientation of molecules and the nature of molecular bonds with respect to $\vec{B}_0$ influence the effect of shielding**.** In liquids, the molecular reorientation is reasonably fast, and so the shielding is averaged out over all orientations. The shielding tensor just becomes the trace of the matrix in (2.40), or $\sigma_{ave} = \sigma_{isotropic} = \frac{1}{3}(\sigma_{xx} + \sigma_{yy} + \sigma_{zz})$. In solids however the molecules are not as free to rotate. One is likely to observe a broad envelope in the spectrum, which is really a collection of overlapping spectra (molecules in all different directions), especially in a polycrystalline or amorphous material. MAS, as mentioned before, can be used so as to suppress the orientation dependence of the chemical shifts and provide narrower lines in the spectrum [33].

For a nucleus with $I > 1/2$, there is an electric quadrupole moment that arises in addition to the usual nuclear magnetic dipole moment. The electric quadrupole moment exists due to lack of spherical symmetry in the electric charge distribution (proton configuration) in the nucleus, and the nucleus in turn loses spherical symmetry. The quadrupolar interaction is the interaction between the nuclear quadrupole moment and the surrounding electric field gradient. The electric field implies the presence of an electrostatic potential $V(\vec{r})$ from the

charge distribution external to the nucleus (i.e. electrons in orbitals plus ionic point charges), where $\vec{r}$ can be taken from the center of nuclear charge.

Expanding $V(\vec{r})$ about the nuclear dipole as a power series and substituting the resulting expression for the potential into one for the electrostatic energy of interaction, (i.e. $E = \int \rho(\vec{r})V(\vec{r})d^3r$ where $\rho(r)$ is the nuclear charge density), the equation for the energy will be a sum of terms (i.e. the multipole expansion). The third of these terms includes the electric quadrupole moment. The electric quadrupole moment tensor Q_{ij} is defined by the following equation

$$Q_{ij} = \int (3x_i x_j - \delta_{ij} \vec{r}^{\,2})\rho(\vec{r})d^3r \tag{2.41}$$

where δ_{ij} is the Kronecker Delta. The classical quadrupole energy E_Q can be expressed as

$$E_Q = \frac{1}{6}\sum_{ij} V_{ij}Q_{ij} \tag{2.42}$$

where V_{ij} is a component of the electric field gradient (EFG) tensor at the nucleus. Analogous to E_Q, the Hamiltonian operator $\hat{H}_Q$ can be written as the following

$$\hat{H}_Q = \frac{eQ}{6I(2I-1)}\sum_{ij} V_{ij}\left[\frac{3}{2}\left(I_i I_j + I_j I_i\right) - \delta_{ij} I(I+1)\right] \tag{2.43}$$

where eQ is the electric quadrupole moment of the nucleus and the spin terms are understood to vector operators [44].

Quadrupolar nuclei in solids usually exhibit line splittings or line broadening due to the quadrupolar interaction. The quadrupolar contribution to spectra may be reduced or averaged out by, once again, the MAS technique. For a solid, the total Hamiltonian may be written as a sum of four terms,

$$\hat{H}_{TOT} = \hat{H}_Z + \hat{H}_C + \hat{H}_D + \hat{H}_Q \tag{2.44}$$

which are the Hamiltonians describing the Zeeman interaction, chemical shift anisotropy, dipolar coupling, and quadrupolar coupling, respectively. By rotating the sample at a uniform frequency about the magic angle, the anisotropic terms become time dependent and can therefore average out while the Zeeman term is not affected by the motion.

2.3 Measuring Diffusion and Its Relation to Ionic Conductivity

As mentioned earlier, NMR allows us to measure the self-diffusion coefficient and by doing so, characterize long range translational motion (along the z-direction) of a molecular or ionic species. Diffusion itself results from the random walk of molecules. There is no preferred direction in which these molecules should move in isotropic materials. We can find a reasonable approximation for the self-diffusion coefficient D via the Stokes-Einstein relation. For a diffusing molecule, D can be expressed by

$$D = \frac{kT}{6\pi\eta r_s} \tag{2.46}$$

where k is Boltzmann's constant, T is temperature, η is the viscosity of the solution the diffusing particle is in, and r_s is an effective radius of the molecule, which we assume to be spherically symmetric. We note that for two molecules of the same type except their radii, the larger molecule will diffuse less in the same solution. The Stokes-Einstein equation (2.46) [45] assumes that the diffusing species is smaller than the solvent molecules and also that the diffusing species do not interact with each other, which basically neglects the collisions between diffusing molecules.

The ionic conductivity σ of an electrolyte is generally proportional to the diffusion coefficient(s). The Nernst-Einstein equation [45] states

$$\sigma = \frac{q^2 n}{kT}(D_+ + D_-) \tag{2.47}$$

where D_+ and D_- are the diffusion coefficients for the cation and anion, respectively, n is the number density of the charge carriers, and q is the charge of each carrier. We note that in a given electrolyte, say for a Li-ion cell, all ions (i.e. cations including Li^+ as well as anions) that are transported contribute to ionic conductivity, but only Li^+ transport is pertinent for the charge/discharge of Li-ion batteries. For a fuel cell, only proton transport is relevant for power generation.

Chapter 3: Experimental Setup and Techniques

3.1 The Spectrometer and its Operation

All measurements were performed on a Chemagnetics CMX-300 MHz spectrometer (See Figure 3.1) used in conjunction with a JMT (Japan Magnet Technology) superconducting magnet of field strength B_0 = 7.1 Tesla. The spectrometer system can be thought of as a complex radio station. A continuous radiofrequency waveform is produced from a frequency synthesizer. Thereafter, the oscillating wave passes through the transmitter, whereby the wave is gated on and off with a switch to create a square RF pulse. Out from the transmitter, the pulse becomes amplified to a desired level. The pulse will then pass through coaxial cables, a diode, and a filter before reaching a device known as the probe. The probe houses the sample under investigation and is placed inside the magnet to a position where the sample sees the central field B_0. An LRC circuit is intrinsic to the probe similar to one encountered in a radio receiver. As with a radio, we tune the circuit to a certain radiofrequency or narrow range of radiofrequencies. Variable capacitors are used to accomplish tuning of the probe. One capacitor is termed a matching capacitor and the other a tuning capacitor depending on how they are each connected with respect to the inductor, or RF coil. Impedance matching of the inductor and the capacitors is sought after for maximum RF energy transmission and absorption to be attained. The probe used for the research outlined in this paper was either a broadband Nalorac Z-Spec diffusion probe or a Doty diffusion probe.

On the receiving side of the spectrometer, the signal coming back from the probe is sent through a quarter wave cable, a preamplification buffer (provides signal amplification prior to entering the receiver) and into the receiver, where the FID is detected. The receiver digitizes the data which is then stored as an array of numbers in the computer. The data acquired is ready to be further processed and analyzed through computer software. It should be noted that there are two channels, one denoted as X and the other as Y. The X channel is for low operating frequencies (below 200 MHz), and channel Y is used for higher frequencies (i.e. 200-300 MHz). Associated with each channel is a frequency source, transmitter, receiver, etc. A block diagram of the spectrometer is shown in Figure 3.1 [46].

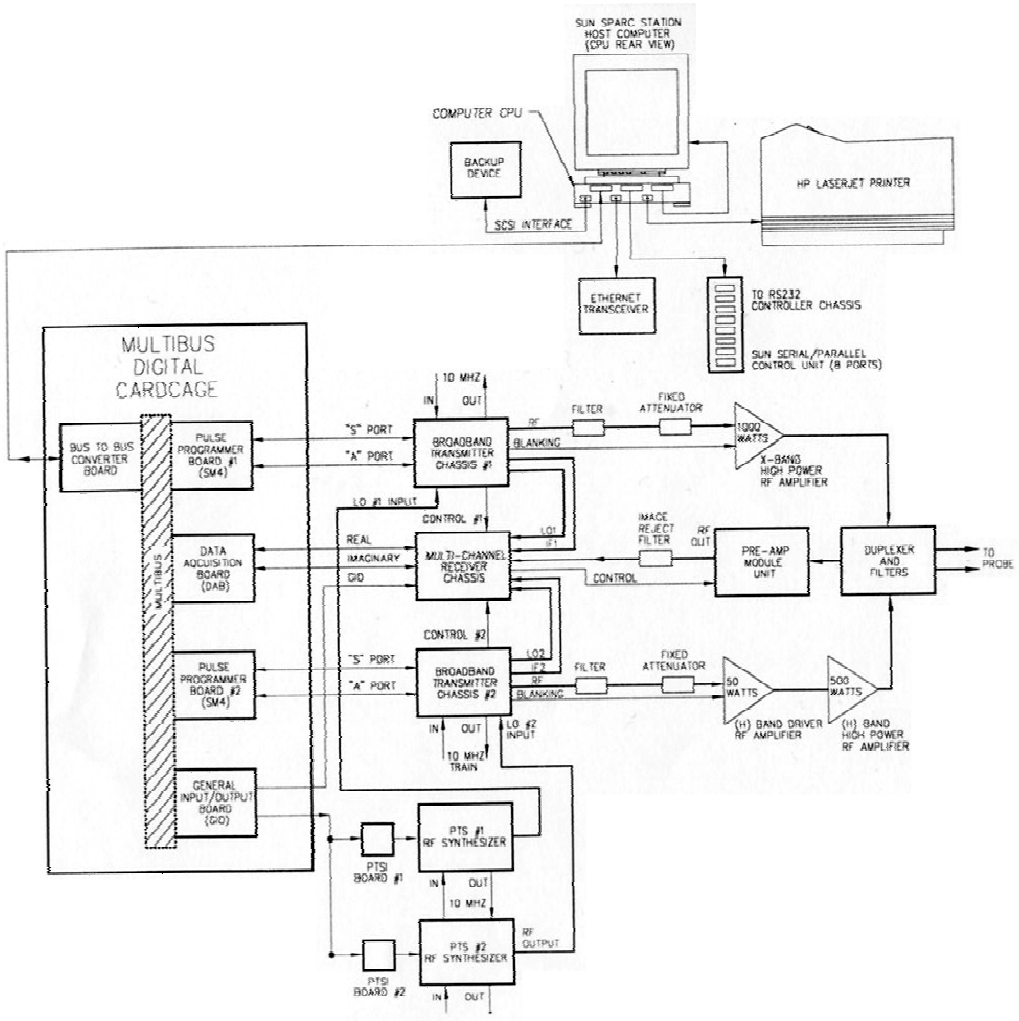

Figure 3.1 – Block Diagram of CMX-300 Spectrometer.

3.2 Pulse Sequences for T_1 and Diffusion

We've touched upon the $\frac{\pi}{2}$ pulse sequence. In this sequence, a pulse of duration t_p is applied. There is then a receiver delay time *rd* (time between end of the pulse and the gating on of the receiver) followed by an acquisition delay time *ad*, or time between the gating on of the receiver and the start of receiver digitization. The FID is then observed along the time axis. Long after the FID decays entirely, a time *pd* (pulse delay) then elapses before the sequence repeats itself. The value for *pd* needs to be about five times the value of T_1 (as derived from the Bloch equations) to ensure the population of spins reach their equilibrium states. In Figure 3.2, the $\frac{\pi}{2}$ pulse sequence is shown.

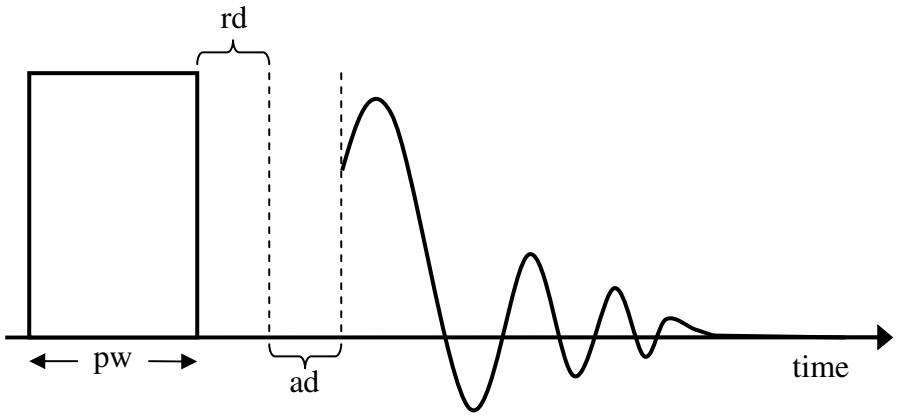

Figure 3.2 – A $\frac{\pi}{2}$ pulse sequence.

T_1 values were measured using the inversion recovery pulse sequence. The sequence begins with the application of a π pulse, from which the magnetization is rotated 180° onto the negative z-axis (as seen from the rotating frame). A time τ then elapses before a $\frac{\pi}{2}$ pulse is applied. In this time τ the magnetization reduces in intensity along the (-) z-axis, and if τ is long enough, the magnetization will start increasing along the positive z-axis attempting to reach the equilibrium magnetization M_0. We recall that $M_z(t) = M_0(1 - e^{\frac{-\tau}{T_1}})$ represents the evolution of the longitudinal component of the magnetization, particularly after the $\frac{\pi}{2}$ pulse. However, the equation $M_z(t) = M_0(1 - 2e^{\frac{-\tau}{T_1}})$, with the extra factor of 2, is used for our measurement of T_1 since there are two time components in the relaxation process (from the (-) z-axis to the transverse plane and from there to the + z-axis) [47]. The equation is computationally fitted for changes in τ (See Figure 3.3).

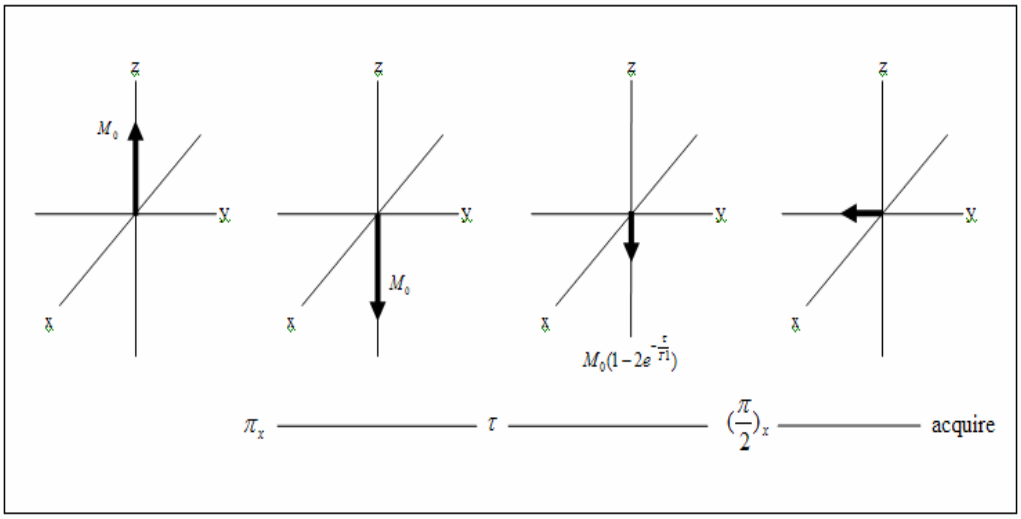

Figure 3.3 – The inversion recovery pulse sequence - M_0 flips onto the (-) z-axis, loses intensity, and is then flipped 90°.

In measuring the self diffusion coefficient *D*, we put into effect a pulsed gradient spin-echo (PGSE) method, which is a combination of the Hahn spin-echo sequence ($\pi/2 - \tau - \pi$) and a pair of square-shaped gradient field pulses. The gradient pulses are generated by a gradient controller and give rise to non-uniform perturbing magnetic fields (along the z-direction). A $\frac{\pi}{2}$ pulse is initially applied to the sample. The magnetization thus flips onto the transverse plane. The RF pulse is then turned off, and the magnetization is allowed to precess freely, that is, the spin isochromats fan out. Not too long after the $\frac{\pi}{2}$ pulse ends, a gradient pulse of strength *g* duration δ is applied. One can think of the application of the gradient pulse as way of encoding the spatial arrangements of the molecules after they have dephased a certain amount. A π pulse is then applied, which also arrives after a time τ from the original $\frac{\pi}{2}$ pulse. As a result of this second RF

pulse, the isochromats that have been dephasing are now flipped 180º along the negative transverse direction and begin to rephase or refocus. Finally, the second gradient pulse of the same strength and duration as the first and at a time Δ from the first gradient pulse, is applied and records the new spatial arrangement of the molecules. Subsequently, we obtain the spin-echo signal in the time domain. The amplitude or intensity of this echo decays with increasing gradient strength since a non-uniform magnetic field will weaken the signal if the nuclei have experienced translational motion during the pulse sequence. Mathematically, the echo amplitude *A* as a function of the gradient strength *g* [47] can be expressed by the following

$$A(g) = \exp[-\gamma^2 D g^2 \delta^2 \left(\Delta - \frac{1}{3}\delta \right) \tag{3.1}$$

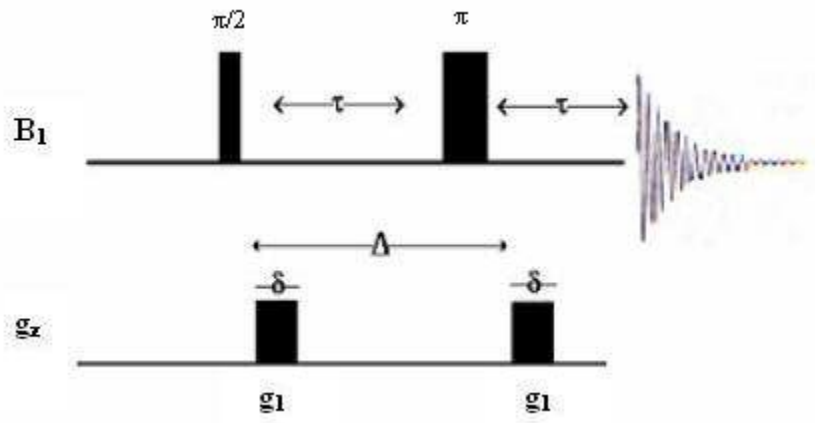

Figure 3.4 – PGSE method.

Experimentally, we vary g and equation (3.1) is mathematically fitted to obtain the self-diffusion coefficient D. For the experiments conducted, the value of g ranged from less than 10 G/cm to ~ 200 G/cm. The time between the gradient pulses, or Δ, ranging anywhere from 10 to 50 ms while δ ranged from 1 to10 ms. The uncertainties in measuring D were about 5%.

The amount by which the echo amplitude attenuates depends on how the diffusing nuclear spins change their positions in the time Δ. If it is the case that T_2, the spin-spin relaxation time, is too short then there may not be enough time to observe an echo. Therefore no value for D can be measured in this case.

Chapter 4: Materials and Their Transport Mechanisms

4.1 NASA Rod-Coil Block Copolymers as Solid Polymer Electrolytes

Lithium-ion solid polymer batteries are promising for air and space applications, such as powering Earth-orbiting satellites and supplying energy for spacecraft vehicles to explore the surface of Mars. Such applications may require a fairly wide temperature range of operation (e.g. -70 to 45 °C for Mars missions). Current state-of-the art solid polymer electrolytes (SPEs) have acceptable ionic conductivities that are on the order of 10^{-4} to 10^{-3} S/cm above 60^{o}C, but the polymers are not mechanically stable and not highly conductive below 60^{o}C [48]. Plasticizers, nanoparticles, and/or solvents may be incorporated into these SPEs in an effort to improve the mechanism for ion transport and sustain high ionic conductivity for a broad range of temperatures**.** However, the addition of such components may compromise the dimensional and thermal stabilities of the solid polymer electrolyte of interest and prove to be incompatible with the electrode materials being employed.

At NASA Glenn Research Center in the group led by Dr. Mary Ann Meador, novel electrolytes have been synthesized which offer a means of improving ionic conductivity while still retaining other critical properties of an effective, viable electrolyte [49]. Instead of utilizing plasticizers and solvents, rod-coil block copolymers have been integrated into the molecular architecture of these electrolytes. Such electrolytes have been reported to generate ionic

conductivities that are almost an order of magnitude greater than that of currently used SPEs at room temperature and below [48], [50].

Block copolymers consist of two or more blocks, or groups of repeat units, connected end to end by covalent bonding. In the investigated solid polymer electrolyte, one set of blocks is composed of rigid polyimide (PI) rods with another made of very flexible, short strands of polyethylene oxide PEO. Due to their incompatibility, the rigid rods and the flexible coils phase separate leading to the formation of nanoscale channels of ionically conducting PEO coils that alternate with rigid PI rods (See Figure 4.1) [50]. The PI rods possess a high glass transition temperature T_g, above which amorphous materials behave like a liquid and below which they exhibit rigid glassy phases. Incorporation of high T_g PI rods improves physical properties of the copolymer and provides mechanical support for the ionically conducting PEO coils.

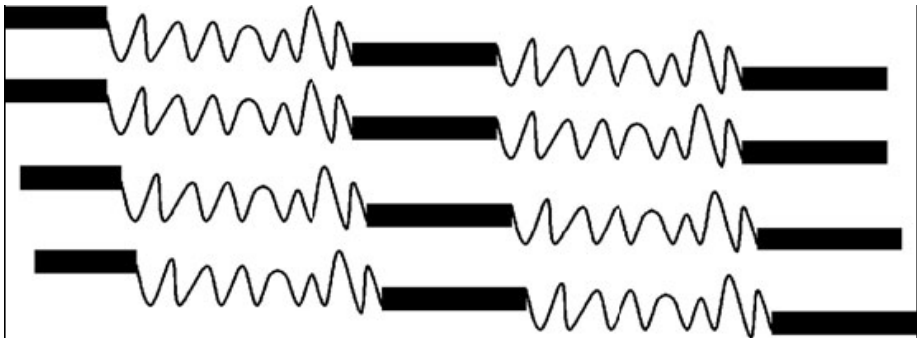

Figure 4.1— A sketch depicting the separate rod and coil phases of this material.

The ion transport in the rod-coil block copolymers primarily occurs in the amorphous phase of semi-crystalline PEO. PEO has a rather simple monomer unit, CH_2-CH_2-O, and it is one of the most studied hosts in polymer electrolytes due to its high chemical stability, high solvating power for salts such as LiTFSI and association of lithium ions to ether linkages, or oxygen sites, in the PEO [51]. The increased solvation may be explained by the flexibility of the polymer chain and the optimal spacing of the polar oxygens, which allows the chain to adopt several low energy conformations. PEO is usually of low molecular weight as higher molecular weights entail higher degrees of crystallization and therefore less ion mobility. Unfortunately, PEO has a tendency to form crystalline regions below 60°C, dramatically lowering conductivity below this temperature [51]. The PEO coil phase of the investigated rod-coil block copolymers does not crystallize and thus allows conduction of lithium ions better than high molecular weight PEO-based SPEs, at room temperature.

In the dynamic bond percolation theory, ionic transport is closely related to the flexibility of the polymer chain backbone [51]. This model can be used to describe long range lithium cation (Li^+) transport in the rod-coil block copolymer. In this model, the cations undergo motion by hopping to vacant coordination sites lying along the polymer backbone. Since the polymer chain is mobile on a local scale, old coordination sites will disappear as new ones are formed. For the mechanism to work, the cations must have the possibility to leave a coordination site. In other words, the interaction between the ions and the polymer chains should be weak enough to allow for a break in the ion-polymer bond. Free volume

and short-range order also facilitate ion transport. The anions of the salt, $SO_2CF_3^-$ ions in our case, tend to have weaker interactions with the polymer chains, and the underlying mechanism of transport for the anions can instead be explained by a jumping to vacant holes in the structure. The positions of these holes vary with time as they are dependent on the segmental motion of the polymer chains.

High conductivity generally requires a low degree of crystallinity of the polymer employed. Li^+ ions have greater mobility in systems based on low molecular weight polymers rather than high molecular weight polymers. The amorphous phase is rather static below the glass transition temperature T_g. Mobility is restricted in the crystalline phase due to the high degree of order. When the glass transition temperature is reached, there is an onset of local molecular mobility at this temperature [51]. Above $T_{g,}$ the amorphous phase is predominantly responsible for ion transport. Ionic mobility is further increased at the melt temperature of the polymer and beyond. To recapitulate, higher conductivities in PEO-based polymers are achieved by lowering the degree of crystallinity as well as lowering T_g.

A standard PEO polymer electrolyte is composed of a salt such as lithium triflouromethane sulfonimide ($LiN(CF_3SO_2)_2$) that is dissolved into solid polymer chains of PEO. The rod-coil block copolymer studied is formed from PEO and rigid polyimides as mentioned but is also characterized by a higher amorphous PEO fraction. Having been doped with lithium salts, the copolymers form rubbery, elastic films having glass-transition temperatures around -50 °C and exhibiting thermal and mechanical stability up to high temperatures (See

Figure 4.2)[52]. Furthermore, these polymers demonstrated room-temperature conductivities as high as 2.3×10^{-5} S/cm, in comparison to 6.0×10^{-6} S/cm for PEO [53]. The copolymer sample tested contained $LiN(CF_3SO_2)_2$ salt with a molar ratio of 20:1 polyether oxygens to lithium ions.

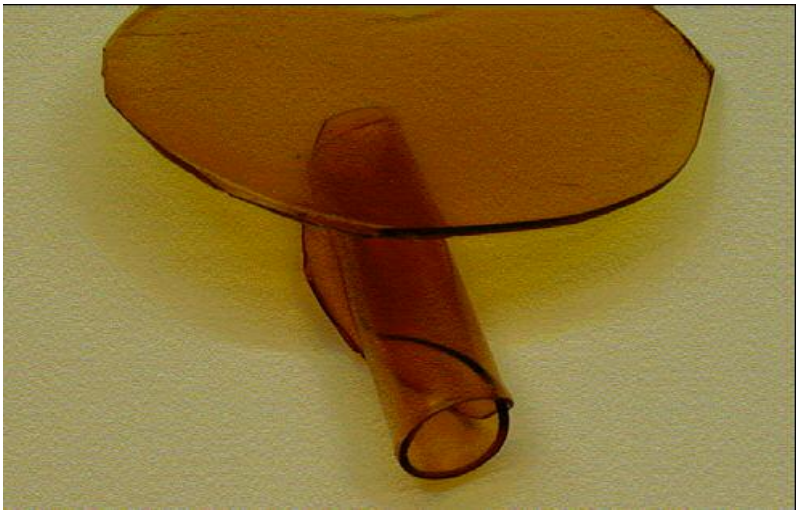

Figure 4.2 – A free standing rod-coil block copolymer.

Some of the factors that can affect Li^+ conduction in these complex materials are lithium salt concentration, polymerization solvent, degree of branching, and molecular weight. One important issue to consider is whether increasing the salt concentration to provide more lithium has an adverse effect on mechanical or ion transport properties. The number of charge carriers of the electrolyte will increase with salt concentration. However, the ionic conductivity will decrease with a sufficiently high concentration of salt since the polymer backbone can stiffen and neutral ion pairs can form [51]. Reduced polymer chain mobility can arise from a crosslinking of the polymer by the coordination of

lithium cations to the ether oxygens. Microscopic viscosity and T_g are then increased. In addition, the free volume for cations to move becomes more limited with increasing salt concentration because the number of vacant coordination sites decreases.

In terms of the polymerization solvent used in synthesizing these rod-coil materials, it is usually N-methylpyrrolidinone (NMP), but lithium salt has been found to be more soluble in the Tetrahydrofuran (THF) solvent [49]. A somewhat elusive factor that can affect ionic conductivity is the degree of branching in the polymer chains. Fully branched polymers suggest more ionic mobility in the coils as opposed to a linear polymer design. Moreover, studies have shown that the highest molecular weight polymers paired with the highest degree of branching result in the greatest conductivity. Yet another variable to consider would be the number of repeat units in the polymer. It has been pointed out that a greater quantity of these units should in fact increase mechanical stability. On the other hand, a smaller number of repeat units may very well allow for greater ion mobility and therefore increased conductivity.

4.2 Gel Polymers Incorporating LiBETI Salt and Ionic Liquids

An NMR study was undertaken on seven gel polymer electrolyte samples from the University of Rome, courtesy of Prof. Fausto Croce and his lab group. These samples were used as received and have possible applications to Li-ion batteries. Each sample incorporates LiBETI ($LiN(CF_3CF_2SO_2)_2$ or lithium bisperfluoroethylsulfonyl imide salt dissolved in a mixed solution of organic

solvents with the entire system being held together by a PVDF-HFP (polyvinylidene fluoride and hexafluoropropylenepolymer) matrix. Synthesis of the gel-type ionically conducting membranes involves first preparing a precursor membrane by dissolving a PVDF matrix in a mixture of organic solvents and then accomplishing gelefication by slowly cooling to room temperature. The precursor membrane is then activated, that is, soaked it into a lithium salt dissolved in organic solvents. During this step, the lithium salt diffuses in the membranes, and the Li-ion conducting gels are formed [54].

The LiBETI salt is a preferable lithium salt for use in a gel polymer electrolyte as it contains a bulky counteranion (allowing for high transference of lithium cations relative to the sulfonyl imide anions), offers good conductivity, has high thermal stability, , and good cycling characteristics. Mixtures of organic solvents were used in these gel electrolytes in efforts to improve ionic conductivity and thermal stability. The PVDF-HFP polymer provides the electrolyte with mechanical strength through polymer chain entanglements and/or chemical cross-linking [55], [56] possesses chemical and thermal stability, and is also inexpensive. Two of the gel polymer electrolytes contained BMITF (1-n-butyl-3-methylimidazoliumbis(trifluoromethylsulfonyl)imide triflate). BMITF is an ionic liquid, or molten salt at room temperature, and it offers a wide liquid range, low volatility, and high thermal stability (above 300°C).

Polar organic solvents tend to have high permittivity, or high dielectric constants, which are desirable for enhancing ionic dissociation and increasing the number of free ion that can contribute to conductivity. Mixtures of two or more

high dielectric solvents were used in efforts to increase conductivity for a wide range of temperatures and lower the melting point of the polymer [57]. The use of these solvents can also improve the mobility of the polymer or PVDF-HFP by increasing the free volume in the system and lowering the glass transition temperature of the polymer, i.e. reduce crystallinty and increase flexibility. In addition, the use of high dielectric solvents has been shown to increase the amount of salt which can be dissolved into the polymer gel electrolyte. These multicomponent solvent mixtures are employed to enhance or optimize the performance and efficiency of a cell over a wide temperature range. A list of the gel polymer samples studied along with their respective compositions is shown in Table 4.1.

Sample	Composition
1	BMITF (ionic liquid), GBL, VC, LiBETI, PVDF 2801
2	EC, GBL, LiBETI, PVDF 2801
20S	EC, GBL, VC, LiBETI, PVDF 2801
25S	EC, PC, VC, GBL, LiBETI, PVDF 2801
26S	GBL, TMP, VC, LiBETI, PVDF 2801
6	BMITF, EC, EMC triflate, LiBETI, PVDF
29S	PC, GBL, VC, LiBETI, PVDF

Table 4.1 – Gel polymers with their composition.

In some of the gel electrolytes studied, EC, or ethylene carbonate and/or PC, or propylene carbonate, were used to achieve desired film characteristics. They both have high boiling points, and they both function as ion dissociation enhancers**.** EC can also provide an effective protective layer on the surface of the graphite anode to prevent continuous electrolyte reduction**.** Five of the electrolytes incorporated another high boiling point solvent GBL (gamma-Butyrolactone), which has a low viscosity and a low melting point. The use of GBL as a cosolvent can allow for high ion conductivity especially at lower temperatures. Ethyl methyl carbonate (EMC) is another low viscosity cosolvent which was incorporated into one of the electrolytes. It enhances low temperature performance as it acts to lower the melting point of the polymer and sustain high conductivity at low temperatures [58]. Vinylene carbonate (VC) was also used as a solvent. It provides thermal stability of the electrolyte for elevated temperatures and/or protects the lithium salt from thermal decomposition [59]. TMP, or trimethyl phosphate, was another solvent used, and it is non-flammable. TMP has also been shown to give good oxidation stability for gel electrolytes in lithium-ion batteries [60].

For two of the gel electrolytes studied, included in their composition was an ionic liquid of BMITF (1-n-butyl-3-methylimidazoliumbis(trifluoromethylsulfonyl)imide triflate). Ionic liquids were developed more than 20 years ago for use in power systems. The ionic liquid gives ionic conductivity and flexibility to an otherwise rigid polymer [61]. Ionic liquids exhibit excellent thermal stability, non-flammability, low volatility (as

opposed to organic solvents), low toxicity, and possess wide electrochemical potential windows. Ionic liquids have proven to be very suitable electrolytes for charge storage systems, such as Li-ion batteries. In application, ionic liquids need to be compatible with the selected polymer as well as the electrodes.

The ion transport mechanism in these composite gel materials appears to be dominated by the liquid component since the conductivity of such gels has been observed to be not much lower than that of the pure liquid electrolyte [62], [63], [64]. In principle, most of the ion conduction occurs through the liquid phase and not through the polymer phase. However, there is sill uncertainty regarding the microscopic environment of the lithium ions, i.e. whether or not they remain completely solvated by the organic solvents, with the host polymer providing only a rigid non-interacting matrix [65]. The T_g of the gel polymer does not as readily dominate the conductivity because the motion of the ions is not reliant on the segmental motions of the polymer chains since the ions are decoupled from the polymer matrix. Ionic conductivity in gel electrolytes is largely dependent on solvent mobility, which allows gel electrolytes to generate higher conductivities than solid polymer electrolytes.

4.3 Gel Polymers Incorporating Li_{13}TFSI/P_{13}TFSI Salt and Ionic Liquids

There is growing interest in the research and development of rechargeable lithium metal/air batteries. Such batteries make use of an inexhaustible supply of air as the cathode and pure lithium metal as the anode. Lithium metal possesses the greatest theoretical specific capacity (mass energy

density) of 3860Ah/kg [66]. The possibility of having a very high specific energy (volumetric energy density) stored in the Li/O_2 system is only limited by design of the device. In today's market, Zn metal/air (theoretical capacity of 820 Ah/kg) batteries are available and are used in hearing aids, but rechargeable lithium metal/air batteries with high specific capacities remain unavailable [66]. Research in Li/O_2 batteries is still evolving, and Li/O_2 batteries are real, promising candidates for energy storage devices.

The discharge reactions of the Li/O_2 battery are [66]:

Anode: $Li \rightarrow Li^+ + e^-$
Cathode: $O_2 + 4Li^+ + 4e^- \rightarrow 4LiO_{1/2}$
Overall: $4Li + O_2 \rightarrow 4LiO_{1/2}$

The Li/O_2 battery has been limited in performance due to a low rate of oxygen diffusion in the porous cathode. Improving the cathode is an essential factor in raising the energy density of the Li/O_2 battery (See Figure 4.3). The anode is composed of a lithium metal foil that is pressed into a metal current collector (e.g. nickel). The air cathode structure is a layered composite with an increased capacity. It is typically a carbon composite made by combining carbon, a metal catalyst, and a binder, all deposited on a metal current collector. A thin Teflon film is good to use as a binder between the air cathode and the atmosphere because it provides hydrophobicity to the cathode to repel moisture and creates channels for oxygen diffusion [67].

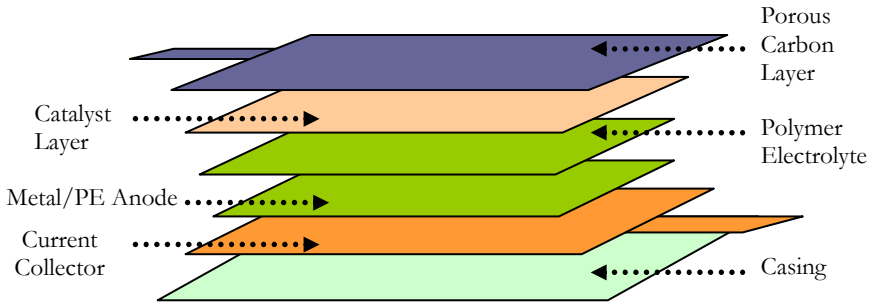

Figure 4.3 – Thin film Li metal/air battery.

An issue of concern in Li/O_2 systems employing a conventional alkaline aqueous electrolyte is that it suffers from a fast capacity loss, which is a result of heavy parasitic reactions between lithium and water. Thermodynamically speaking, a short shelf life is also present, leaving the battery unable to recharge. Desirable electrolytes require good lithium/electrode interface stability, high electrochemical stability, and low volatility. The use of a rechargeable Li/O_2 cell, which used a polymer gel electrolyte based on organic solvents, was first reported by Abraham and Jiang [68]. The cell demonstrated several advantages including a solid state design, rechargeability and high capacity.

However, the highly reactive lithium metal is not so thermodynamically compatible with common organic solvents [66]. Additional challenges arise since the air cathode of Li-air cells must be open to the ambient environment. Whichever organic solvent-based gel electrolyte is employed, it must have the properties of non-volatility or at least very little volatility, air stability, as well as be able to resist moisture absorption, and also allow for penetration to the lithium anode. There exist some ionic liquids that meet the rigorous requirements of the

electrolyte for use in for Li-air batteries. Such liquids have stability with lithium metal, non-volatility, hydrophobicity, stability with air and moisture. Ionic liquids as aforementioned have interesting electrochemical properties including high ionic conductivity and a wide electrochemical stability window. Ionic liquids with proper proportions of cations to anions are electrochemically stable against lithium metal as opposed to the conventional organic solvents.

Novel gel polymer electrolytes based on the room temperature ionic liquid 1-methyl-3-propylpyrrolidinium bis(trifluoromethanesulfonyl)imide(P_{13}TFSI) have been investigated. Our collaborators at Rutgers University, lab by Prof. John Xu, synthesized the electrolyte membranes. Synthesis was accomplished by mixing $LiN(CF_3SO_2)_2$ (LiTFSI) and the ionic liquid P_{13}TFSI and blending the resulting solution with poly(vinylidene co-hexafluoropropylene) (PVDF-HFP), with or without the incorporation of a small amount of ethylene carbonate (EC). Figure 4.4 shows the structure formula of the components of the gel polymer electrolyte membranes [69].

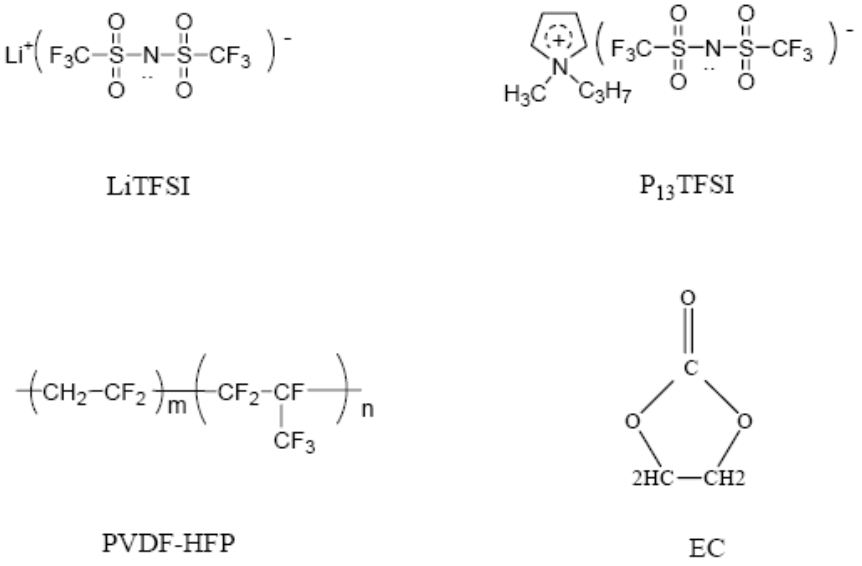

Figure 4.4 - Structure formula of the components of the gel electrolytes.

The addition of EC serves to plasticize, enhance Li-ion transport concentration and kinetics, and extend the low temperature application limit. The electrolyte membranes are elastic and dimensionally and mechanically stable. They exhibit good ionic conductivity of $1\sim5\times10^{-4}$ mS/cm at 23°C, excellent electrochemical stability and thermal stability [69]. Electrochemical characterization has also shown that Li can be reversibly dissolved into and deposited from these membranes.

4.4 Nafion Membrane for Use in PEMFCs

Nafion® is an ion-conducting copolymer that was developed in the 1960s by DuPont de Nemours & Co. To date, Nafion has been the only successful

commercially used membrane for the Proton Exchange Membrane Fuel Cell (PEMFC). Nafion membrane possesses good mechanical strength, selectivity, good ion exchange properties, insolubility in water, chemical stability, and fairly good thermal stability. The structure of Nafion incorporates a hydrophobic fluorocarbon backbone and a hydrophilic, strongly acidic sulfonic pendant side chain (See Figure 4.5). The presence of the hydrophobic fluorocarbon chains together with the hydrophilic sulfonic acid regions provides a phase separation that will in turn give rise to a channel for proton transport [70]. Neutron scattering and small angle X-ray experiments have confirmed that the sulfonic groups aggregate to form tightly packed regions, or clusters, within the Nafion polymer as a result of electrostatic interactions [71].

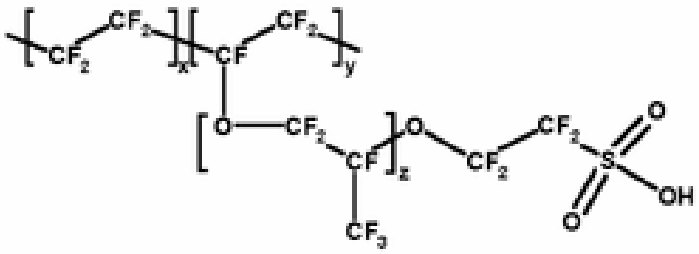

Figure 4.5 – The structure of a Nafion membrane –
a poly(tetrafluoroethylene) based ionomer with
sulfonic acid pendent side chains [72].

During hydration of Nafion, the sulfonic groups absorb most of the water, swell up, and aggregate into larger clusters as their protons are donated to the surrounding water molecules. The number of sulfonic acid groups and the interactions between them and the water molecules affect the formation of hydrophilic channels that interconnect the clusters to permeate proton flow. The

sizes and the forms of the clusters and the channels are defined by the ability of the membrane to take in water, the distribution of the side chains and their ability to form clusters.

One proposed model of proton transport in hydrated Nafion is described by a classical diffusion of the hydronium H_3O^+ ions, which form when dissociated acid protons bind with water molecules. H_3O^+ ions move through the acid sites as they travel from one ion cluster region to the next, and protons therefore move together with the water molecules. Another model, commonly known as the Grotthus mechanism for diffusion, involves a reorganization of the polymer which enables proton hopping between acid sites, that is, protons move by transferring from one water molecule group to another. During the process of Grotthus diffusion, weak hydrogen bonds continually form and break apart between tumbling water molecules and reoriented acid protons [73]. For higher water contents of Nafion, there has been evidence to suggest that the classical diffusion, or vehicular, mechanism plays more of a factor in characterizing proton migration than does the Grotthus mode of transport [74]. Also, at higher temperatures the hydrogen bonding between the water molecules becomes weaker rendering the proton hopping involved in the Grothus mechanism less favorable while the vehicular mechanism dominates. However, it is clear that both mechanisms involve hopping of protons between water and diffusion of water. Thus, increasing the hydration level of a perfluorosulfonic acid membrane such as Nafion is certain to raise its proton conductivity as greater amounts of water entail easier accessibility with which protons can travel.

Nafion has a unique ability to absorb relatively large amounts of water. It can increase its dry weight by as much as 30 percent or more depending upon its molecular weight, sulfonic acid content and concentration, and membrane pretreatment. Proton conductivity is highly dependent on the level of hydration, or water uptake (measured by weight). An excessive increase in the hydration level, however, may potentially cause a considerable loss in mechanical strength and electrical resistance therefore reducing fuel cell efficiency [75]. For temperatures up to ~80^{o}C, proton conductivity increases for Nafion. Above 80^{o}C, the water vapor pressure required to keep a given amount of water in the membrane increases, thereby increasing the likelihood that water loss will occur and significantly reduce proton conductivity [76]. The loss of water at higher temperatures implies an overall drop in conductivity as fewer water molecules remain in tact to "drag" along dissociated acid protons. And so a limitation of Nafion is that it suffers from dehydration for temperatures above 80^{o}C in applications to PEMFCs. Water retention is therefore an imperative issue to be considered when synthesizing PEMs.

In addition, methanol permeability through Nafion is high, which is unfavorable for applications to direct methanol fuel cells, DMFCs. DMFCs are being developed for portable power, automobiles, and military applications, and they have a typical operating temperature range of 60^{o}C – 150^{o}C. The advantages of using methanol include its easy storage capacity, higher mass energy density (than hydrogen gas), and low boiling point [77]. The transport properties of Nafion-117 ("11" referring to its molecular weight value of 1100 and "7"

corresponding to the thickness of the membrane in thousandths of an inch) with water and separately with methanol were investigated.

4.5 SPTES and 6F-SPTES Copolymer Membranes for Use in PEMFCs

Highly sulfonated poly(arylenethioether) sulfone (SPTES) copolymer membranes have been synthesized by Dr. Thuy Dang of the Air Force Research Laboratory for use as electrolyte membrane separators in PEMFCs and DMFCs. SPTES copolymers are possible alternatives to Nafion. The structure of the SPTES copolymer membrane is shown in Figure 4.6 The SPTES copolymer incorporates highly sulfonated regions attached to an aromatic hydrocarbon polymer backbone. The SPTES copolymers contain up to two sulfonic acid units per polymer repeat unit [78]. The high degree of sulfonation in these membranes serves to enhance water uptake and thereby provide greater proton mobility. Too high a sulfonation degree may very well result in excessive swelling or even solubility of the polymers in water. The use of hydrocarbon groups is thought to offer greater structural and thermal stability than the fluorocarbons of Nafion**.** The hydrophobic hydrocarbons and the hydrophilic sulfonic regions phase separate and give rise to ionically conducting channels through which proton hopping is facilitated. Endcapping, or polymer chain stopping, of the copolymers was carried out to minimize the potential for water solubility. The endcapping groups were bulky, organic compounds. SPTES copolymers are also cheaper to synthesize than Nafion.

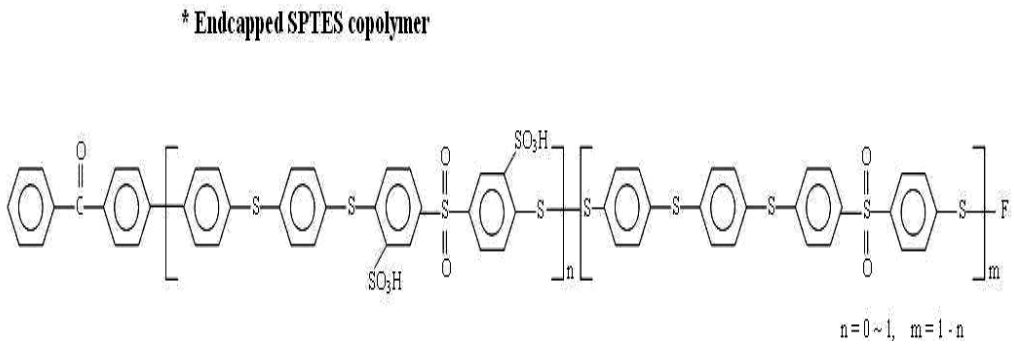

Figure 4.6 – Endcapped SPTES copolymer structure.

Hydrocarbon polymers containing polar groups are particularly attractive because they can retain high amounts of water over a broad temperature range. The SPTES copolymer membrane was designed to deal with the challenges faced in high temperature operation (>120^{o}C) and have extended performance. The PEM used must be able to sustain a high ionic conductivity, retain water well, and at the same time be mechanically stable at elevated temperature. The transport properties of SPTES-50 ('50' referring to percent ratio of sulfonated to unsulfonated sulfone) copolymer membrane were studied herein.

Hexafluorinated SPTES copolymer membranes for applications to PEMFCs have been synthesized and investigated as well. These particular membranes incorporate additional CF_3 groups to the original SPTES structure, i.e. two CF_3 groups per repeat polymer unit (See Figure 4.7). The fluorine groups are believed to balance the hydrophilicity and hydrophobicity of the polymer backbone in an attempt to preserve membrane structure as water is absorbed. More importantly, the fluorination was carried out so as to mimic the morphology of Nafion, and therefore achieve similar ion cluster channel formation for proton

transport. 6F-SPTES-70 and 6F-SPTES-50 copolymer membranes have been studied. Single fuel cells were successfully manufactured with the inclusion of 6F-SPTES 50 membrane material. The overall performance of 6F-SPTES 50 copolymer was found to be similar to Nafion at both low and high temperatures (100°C). The high thermal stability and high intrinsic proton conductivities of 6F-SPTES-50 had qualified these polymers as potential cost-effective alternatives to Nafion [79].

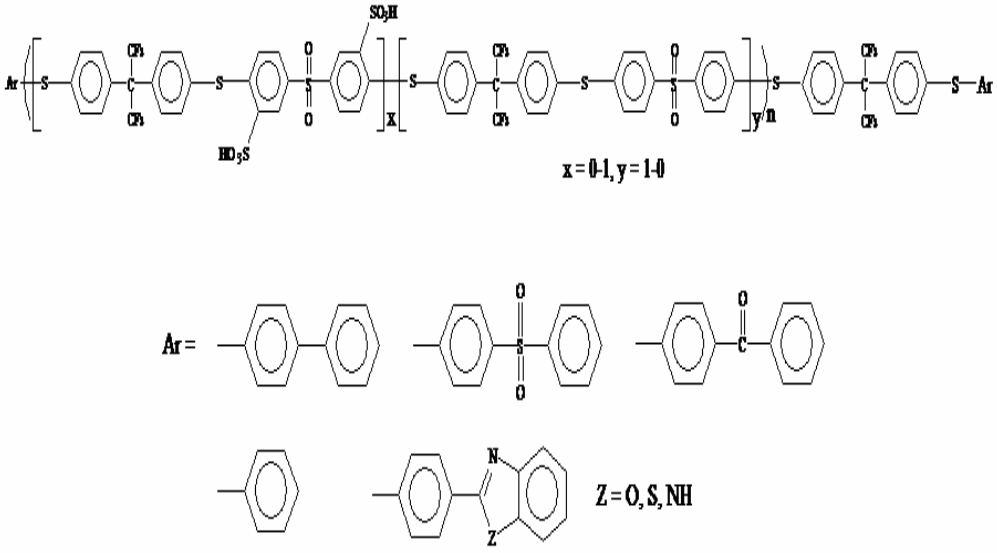

Figure 4.7 - The chemical structure of fluorinated poly (arylenethioethersulfone) endcapped copolymers with sulfonic acid pendants.

Chapter 5: Morphology of PI–PEO Block Copolymers for Lithium Batteries*

Abstract

Polyimide (PI)-polyethylene oxide (PEO) block copolymers have a wide variety of applications in microelectronics, since PI-PEO films exhibit a high degree of thermal and chemical stability. The polymers consist of short, rigid rod T-shaped PI segments, alternating with flexible, PEO coil segments. The highly incompatible PI rods and PEO coils should phase-separate, especially in the presence of lithium ions used as electrolytes for lithium polymer batteries. The rigid rod phase provides a high degree of dimensional stability. In this paper, we provide evidence by DSC that the self-assembled ordered structure of the PI-PEO molecules is formed from concentrated solution rather than the bulk state. Tapping mode AFM and X-ray diffraction are applied to observe the nanodomains in the phase separation of the PI and PEO before and after doping with lithium ions. In addition, we report evidence of the ion transport primary mechanism, in the amorphous phase of the lithium salt-doped PI-PEO block copolymers' multinuclear NMR linewidth, spin-lattice relaxation time, and pulsed field gradient diffusion measurements.

*This chapter constitutes the publication “Morphology of PI–PEO block copolymers for lithium batteries,” by A. Khalfan, G.D. Bennett, S.G. Greenbaum, C. Xue, M.A.B. Meador, L. Zhu, J.J. Ge, S.Z.D. Cheng, S. Putthanarat, R.K. Eby, in Polymer, Volume 47, Issue 17, 9 August 2006, Pages 6149-6155.

5.1 Introduction

Rod-coil molecules are a novel type of block copolymer with unique microstructure due to their ability to self-assemble to various ordered morphologies on a nanometer length scale [80]. These molecules, comprised of two homopolymers joined end to end, microphase separate into ordered, periodic arrays of spheres and cylinders in the bulk state and/or solution [81] and [82]. Recent applications of block copolymers include use as solid polymer electrolytes for lithium batteries. After Wright's discovery of ionic conductivity in alkali metal salt complexes of poly(ethylene oxide) [83], these polymers were proposed as electrolytes for batteries by Armand et al. [84] since they combine the advantages of solid-state electrochemistry with the ease of processing inherent to plastic materials. The poly(ethylene oxide) structure is the basis for many electrolytes currently under study because of its ability to solvate lithium ions. However, long chains of poly(ethylene oxide) tend to crystallize and slow ion mobility at temperatures below about 80 °C, unless the crystalline units are aligned [85]. Various approaches to prevent this crystallization are currently under study [86], including plasticizers [87], hyperbranched polymers [88], and the use of nanoparticle additives [89]. One of the more intriguing approaches involves the use of copolymers that phase-separate into nanodomains. For example, Soo et al. [90] have demonstrated this concept with a system in which one of the domains is a poly(methyl methacrylate) with ethylene oxide side chains and the other is a siloxane. Though both domains consist of polymers that are well above their glass transition temperature (T_g) at room temperature, the interface imparts solid

behavior upon films fabricated from the blocks and room temperature ionic conductivities are quite high. Molecular dynamic simulations suggest that the lithium ions are complexed with PEO through approximately five ether oxygens of a PEO chain.

Okamoto et al. have reported block copolymers consisting of rod-coil structures [91] and [92]. The short, rigid rod segment and flexible, polyalkylene oxide coil segment are phase-separated into two major domains, which increase the selectivity for CO_2/N_2 gas separation. They have found that the linear polyimide rods show the best gas separation properties due to the phase separation.

Recently, Meador and coworkers have reported a similar class of branched polyimides (PI)–polyethylene oxide (PEO) polymers and examined their behavior as possible electrolytes for lithium polymer batteries [93] and [94]. Whereas the coil phase allows conduction of lithium ions better at room temperature than high molecular weight PEO, the more rigid polyimide rod phase with a very high T_g, provides improved physical properties over other phase-separated polymer electrolytes.

In this paper, we give a detailed study of the morphologies of the branched PI–PEO films. The self-assembled ordered structure of the PI–PEO molecules, consisting of short, rigid rod T-shaped PI segments, alternating with flexible, PEO coil segments is formed from concentrated solution. Morphology of the phase separation is monitored by small angle X-ray scattering (SAXS) and Atomic

Force Microscopy (AFM). Direct evidence of the ion transport primary mechanism along the amorphous phase of the lithium salt-doped PI–PEO block copolymers shown is provided by ^{7}Li and ^{19}F NMR relaxation and transport measurements.

5.2 Experimental

A fully branched PI–PEO with a formulated molecular weight of 60 000, n = 10.72 g/mol as shown in Scheme 1 was prepared as previously described with and without lithium doping at a Li:O ≈ 0.05 (the molar ratio of lithium salt over oxygen of ethylene oxide units) [94]. The ionic conductivity of the lithium containing polymer has been previously reported as 2.45×10^{-5} S/cm at room temperature [94]. The samples were stored in vacuum before characterization and analysis.

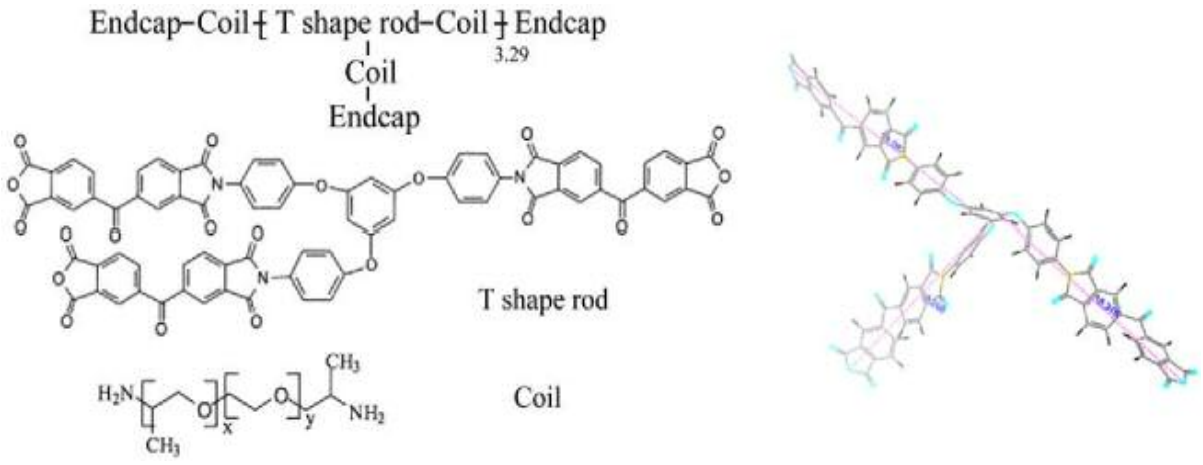

Scheme 5.1 - PI–PEO block copolymer structure and T-shaped imide rod conformation of computer simulation.

Differential scanning calorimetry (DSC, Perkin–Elmer PYRIS Diamond) experiments were carried out to study the isothermal crystallization and melting behaviors of un-doped PI–PEO. The DSC instrument was calibrated with *p*-nitrotoluene, naphthalene, and indium standards. Isothermal crystallization was conducted by quenching the samples from 120 °C to the preset T_c. The fully crystallized samples were then heated to 80 °C at a rate of 5 °C/min. The endothermic peak temperature was taken as the melting temperature (T_m).

A Rigaku 18-kW rotating-anode generator (Cu K) equipped with an image plate and a hot stage was used to obtain high-quality fiber patterns after 30 min to 1 h of exposure times. The diffraction 2θ positions and widths observed on the powder and fiber patterns were calibrated with silicon crystals with known 2θ diffractions and crystallite sizes when $2\theta > 15°$ and calibrated with silver behenate when $2\theta < 15°$.

Transmission electron microscopy (TEM) studies were conducted using a JEOL 1200EX II at an accelerating voltage of 120 kV. Thin slices of block copolymer for TEM observation were obtained using a Reicher Ultracut S (Leica) cryomicrotome at −120 °C. The thin film thickness was around 100 nm. Phase contrast was obtained by staining in vapor of a 3% RuO_4 water solution for 20 min. The PEO phase was stained, since it was more easily oxidized than the PI phase.

Atomic Force Microscopy (AFM, Digital Instrument Nanoscope IIIa) was used to examine the surface topology of the thin film treated as described before

[93] and [94]. A 100 μm scanner was selected and a tapping mode was used to obtain both height and phase images. The scanning frequency was controlled within 0.2–0.5 Hz for the low magnification images. The data were collected with a 512 × 512 pixel per image resolution.

The NMR measurements were performed on a Chemagnetics CMX-300 spectrometer in which the Larmor frequencies of ^{7}Li and ^{19}F are 116.9 and 283.2 MHz, respectively. Variable temperature spectral linewidths, spin-lattice relaxation times (T_1) and self-diffusion coefficients were investigated. Measurements were made using 0.5–1.0 g samples which were loaded and packed into flame-sealed 5-mm Pyrex tubes in a very low humidity (<1 ppm) dry-box (VAC). Self-diffusion coefficients were obtained by the NMR Pulse Gradient Spin-Echo technique [95], which uses the Hahn spin-echo pulse sequence ($\pi/2$–τ–π), with typical $\pi/2$ pulse width of 5 μs for ^{7}Li and 11 μs for ^{19}F, on a Nalorac Z-Spec gradient probe. For a diffusing spin in the presence of a magnetic field, the application of square-shaped magnetic field gradient pulses of magnitude g results in the attenuation of the echo amplitude A, represented by:
$A(G) = \exp[-\gamma^2 G^2 D\delta 2(\Delta - (\delta/3))]$, where D is the self-diffusion coefficient for a range of gradient strengths G from 10 to 200 G/cm, γ is the nuclear gyromagnetic ratio, Δ is the time interval between two gradient pulses and δ is the duration of the single gradient pulse. For the polymer electrolytes investigated, the experimental parameters Δ and δ, given in ms, ranged from 45 to 100 and 15 to 25, respectively, for ^{7}Li, and from 25 to 35 and 4 to 5, respectively, for ^{19}F. Uncertainties in self-diffusion measurements are about 3–5%. NMR spectra were

obtained by transforming the resulting free induction decay (FID) of a single π/2 pulse sequence or a solid echo ($\pi/2_x$–τ–$\pi/2_y$) pulse sequence. Spin-lattice relaxation times, T_1, were obtained by inversion recovery. Uncertainties in T_1 determinations were about 3%. The sample was allowed to equilibrate for 20–25 min between temperature changes.

5.3 Results and discussion

5.3.1 Crystallinity and phase separation of un-doped PI–PEO

The solution self-assembled phase behavior of the un-doped PI–PEO has been examined with SAXS at room temperature as shown in Fig. 5.1. A diffraction scattering halo with a *d* spacing of 13 nm is observed, indicating that a microphase separation occurred when the PI–PEO polymer was cast from solution in *N*-methylpyrrolidinone (NMP). It is known that the phase behavior of a bulk block copolymer actually depends on three physical events, which compete with each other or override one another in forming the final phase and crystalline morphologies in amorphous–crystalline block copolymers. These events are the microphase separation of the block copolymers at T_{ODT} (order–disorder transition), the crystallization of the crystallizable blocks at T_c^c, and the vitrification of the amorphous blocks at T_g^a. To form a microphase separated structure, T_{ODT} should be larger than T_g^a. Since TMA experimental results have shown that the T_g^a of PI is above 200 °C and the T_{ODT} is in the range of 80–110°, it can safely be said that the microphase separation of this PI–PEO material is

occurring in solution rather than in the bulk state. Direct evidence is provided by AFM phase (right) and height (left) images in Fig. 5.2. In the phase image, some lamellar structures stack on top of the others, while some align edge to edge. The lamellar thickness measured from the height image is in the range from 11 to 15 nm, which is in agreement with the SAXS experiment result. AFM experiments were also performed below 10 °C (Fig. 5.3). In the phase image, some PEO crystals are formed between (region A in Fig. 5.3) and in (region B in Fig. 5.3) the lamellas. In region A, the lamellas are edge on and expanded by PEO crystals with a dimension of 16 nm. In region B, actually in one lamella, the PEO crystallized in the lamella with dimension of 16 nm. To understand how the molecules self-assemble into this ordered structure, the molecular conformation of the crystallizable PEO coil and the amorphous PI rod must be studied.

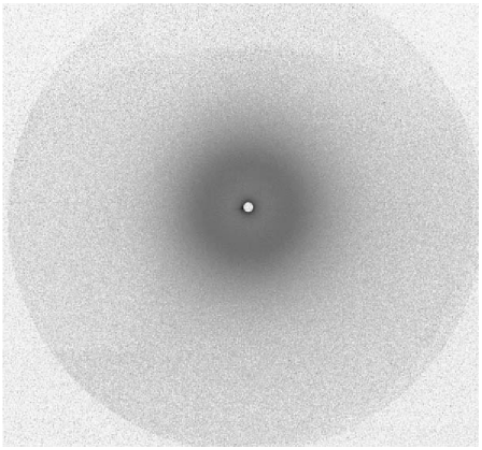

Figure 5.1 High-resolution synchrotron SAXS pattern.

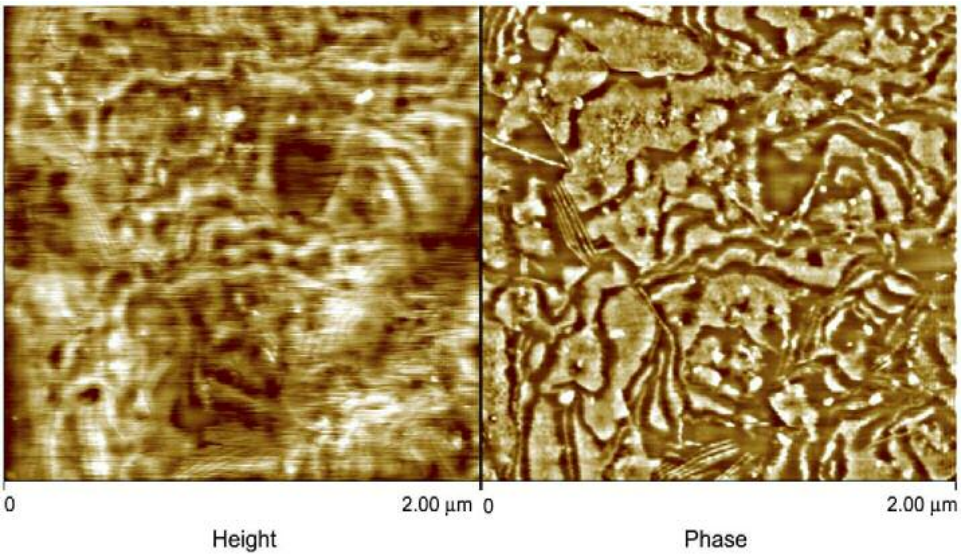

Figure 5.2 - AFM height (left) and phase (right) images of PI–PEO block copolymer at room temperature.

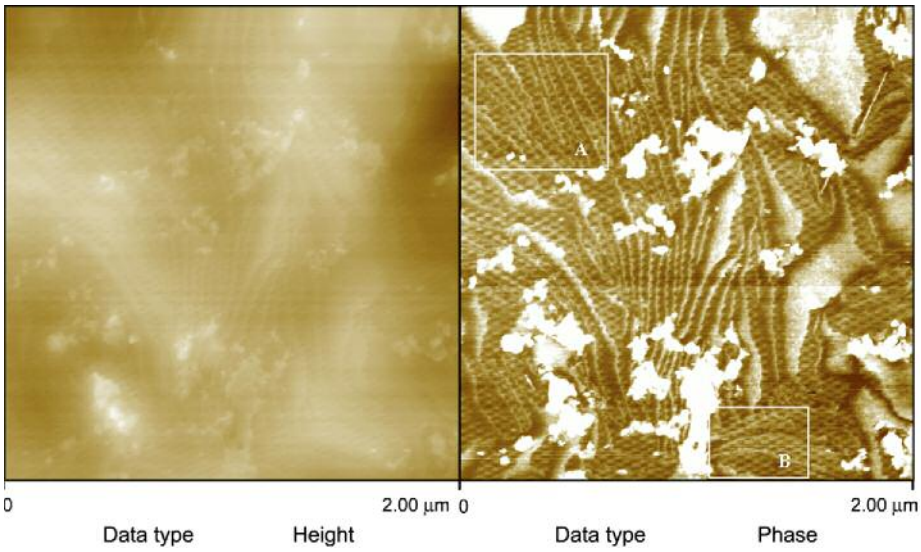

Figure 5.3 - AFM height (left) and phase (right) images below 10 °C.

To investigate the possible effects of the molecular architecture of PEO on this confined environment, a wide angle X-ray diffraction (WAXD) experiment

has been carried out at 5 °C. Fig. 5.4 demonstrates the typical WAXD pattern. The diffraction rings at $2\theta = 19°$ come from the (120) plane, and the ring around $2\theta = 23°$ is actually multiple diffraction rings with contributions from diffraction of several crystal planes. The linear PEO can be fitted into a monoclinic crystal structure. The unit cell parameters are $a = 0.805$ nm, $b = 1.304$ nm, $c = 1.948$ nm and $\beta = 125.4°$ [96]. The repeating unit in a single chain shows a succession of *trans*, *trans*, *gauche* (*ttg*) conformations. The *ttg* conformation exhibits a (7/2) helix with D_7 symmetry. D_7 indicates a dihedral molecular symmetry and the subscript denotes a sevenfold screw axis parallel to the molecular axis. Since the period of the *c*-axis includes seven repeating units, each repeating unit possesses a length of 0.278 nm in the crystalline portion. The average chain length, *L*, is given by the following equation: $L = 0.278 \times M_n/44$, where 44 is the molecular weight of one PEO repeat unit. In our case, the extended PEO chain length is about 12.6 nm with a molecular weight of 2000.

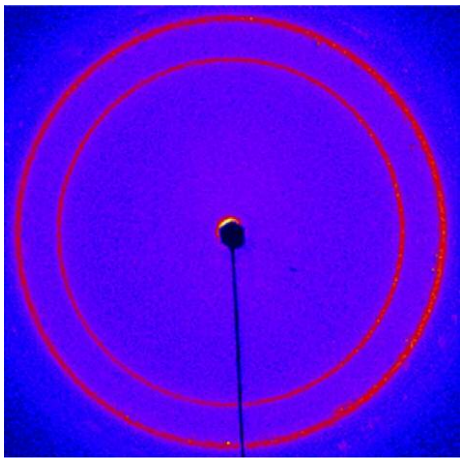

Figure 5.4 - 2D WAXD pattern. (The first reflection ring is (120) reflection. The second ring includes the (−130), (032), (−212), (112), (−124) and (004) reflections.)

The computer simulation provides the T-shaped rod length parameter shown in Scheme 1. The length of the rod in the main chain is 3.7 nm and the length of the rod in the side chain is 1.8 nm. By combining the molecular conformation and the AFM experimental results, a probable microphase separation model has been provided (Fig. 5.5). In this model, the T blocks represent the T-shaped rigid imide rods and the lines represent the extend PEO chains. Fig. 5.5a is the side view of the lamellas, which consist of the main chain polymers. The side chains with rod and PEO crystals will separate the lamellae. This model depends on the inter-molecular phase separation between PEO in side chains and imide rods in the main chain. The top view of the lamellas is shown in Fig. 5.5b. The intra-molecular phase separation between PEO crystals and imide rods will direct the main chains to form this kind of lamella.

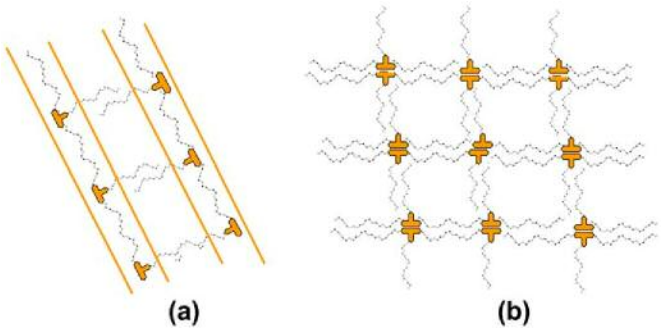

Figure 5.5 - Most probable model (a) lamellar side view (b) lamellar top view

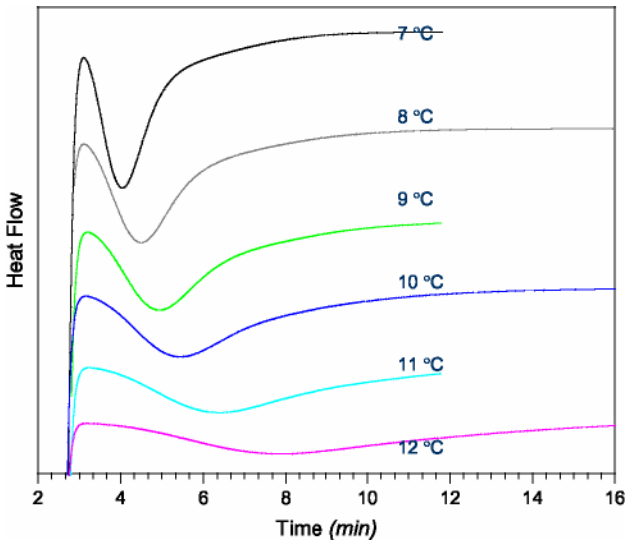

Figure 5.6 - DSC curves of heat flow vs. time during isothermal crystallization. (The numbers for the lines represent the crystallization temperatures.)

To further examine the lamellar formation of the PEO in the confined space, isothermal melt crystallization was studied by cooling the melt rapidly to a designated crystallization temperature (T_c). As the T_c increases, the crystallization exotherms shift to higher temperatures and become broad. The Avrami equation [97], which assumes that the relative degree of crystallinity (X_t) develops with time t, was used to analyze the isothermal crystallization process of PEO. The development of relative crystallization with time for isothermal crystallization from the melt is shown in Fig. 5.6. The relative amount of crystallinity that develops at a definite time decreases with increasing crystallization temperature T_c. The degree of crystallinity of the PEO block can be also measured from wide angle X-ray diffraction by resolving the total intensity curve into three curves representing diffracted X-ray intensities from amorphous material and (120) crystalline planes. The well-known double logarithmic plots $\log[-\ln(1 - X_t)]$ vs.

log(t) are shown in Fig. 5.7. Each curve shows an initial linear portion, subsequently tending to level off. This deviation was considered to be due to the secondary impingement in the later stage [98]. The Avrami parameter n for PEO crystals determined from the initial linear portion in Fig. 5.7 represents the PEO crystallization mechanism. The n values at different crystallization temperatures are from 2.85 to 2.88 °C, which indicate that the PEO is crystallized in a lamellar behavior.

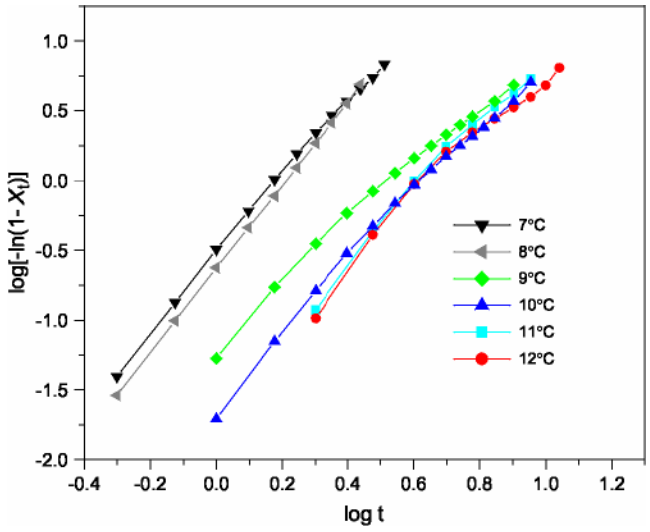

Figure 5.7 - Plots of log[−ln(1 − X_t)] vs. log(t) for isothermal crystallization. (The numbers for the lines represent the crystallization temperatures.)

5.3.2 Lithium doped PI–PEO

As previously reported, the PI–PEO doped with Li at a Li:O ≈ 0.05 (the molar ratio of lithium salt over oxygen of ethylene oxide units) has no crystalline transition as evidenced by DSC and the T_g increases by 8–10 °C over that of the un-doped film (−56 °C) [94]. Morphology of the doped polymer was investigated by AFM tapping model. In the right phase image of Fig. 5.8, we observe no crystalline lamellae as in the un-doped PI–PEO copolymer in Fig. 5.2. Only phase separation is observed. This is also seen in a TEM of the sample stained using RuO_4 after cutting samples of a thickness of about 50 nm as shown in Fig. 5.9. Since PEO-rich phases are more easily stained, they appear darker than the PI-rich phase. There is no obvious ordered structure in the micrograph. Hence, both AFM and TEM results provide further evidence that the lithium doped block copolymer is in an amorphous state.

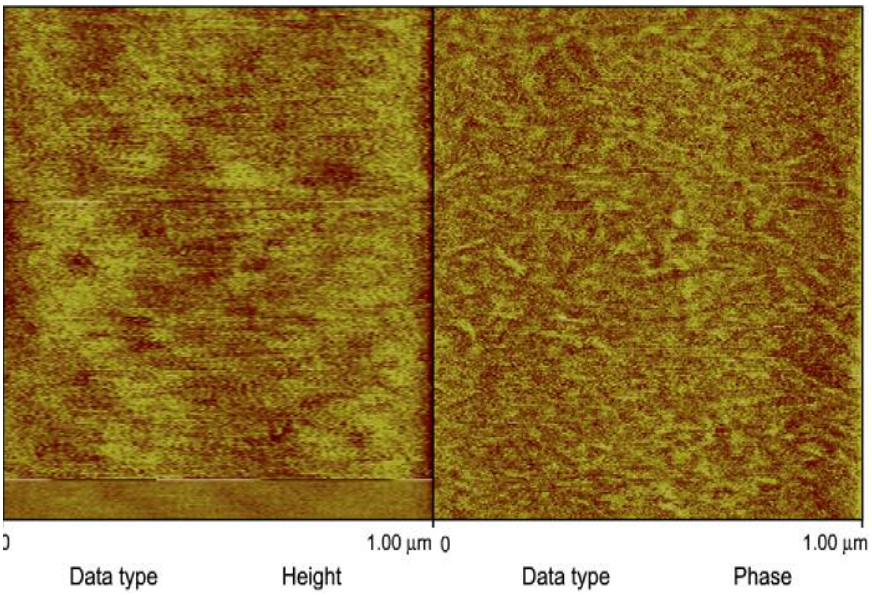

Figure 5.8 - AFM height (left) and phase (right) images of lithium doped PI– PEO block copolymer at room temperature.

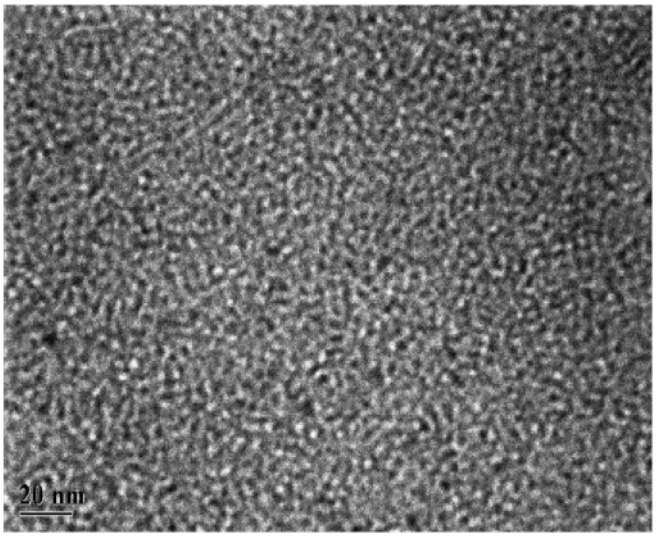

Figure 5.9 - TEM observation of the lithium doped PI–PEO block copolymer after RuO_4 staining.

5.3.3 Transport studies

Early studies of PEO-based electrolytes suggested a crystalline phase transport mechanism involving ionic conduction through the PEO helices [84], however, the vast majority of subsequent investigations have shown that the ion transport occurs primarily in the amorphous phase [99]. On the other hand, under certain conditions for comparable compositions, the crystalline phase cation transport can exceed that of the amorphous phase [100], and the crystalline phase transport can be significantly augmented when the polymer is aligned through mechanical [101] or magnetic means [85]. However, in randomly oriented systems (as in the present case), it can be assumed that the amorphous phase transport mechanism is the dominant one.

Arrhenius plots of NMR linewidth, spin-lattice relaxation (T_1), and self-diffusion coefficients (D), corresponding to both cations and anions (^{7}Li and ^{19}F, respectively), are displayed in Fig. 5.10, Fig. 5.11 and Fig. 5.12, respectively. The cation- and anion-associated linewidths (Fig. 10) exhibit similar activation energies, suggesting a common factor that influences their dynamical behavior, i.e. segmental motion of the PEO phase. Spin-lattice relaxation is most sensitive to motional processes near the reciprocal angular NMR frequency, in fact more rapid than those probed by the linewidth measurements. The T_1 results in Fig. 5.11 revealed different behaviors for the cations and anions, partly due to the higher ^{19}F resonance frequency as compared to ^{7}Li, but also attributed to other factors. In particular, the ^{7}Li T_1 exhibits a minimum near 345 K, whereas the ^{19}F T_1 minimum is less apparent due to the limited temperature range at the lower end, but possibly occurring at around 295 K. Efficient spin-lattice relaxation could in fact be achieved through rotation of the CF_3 group on the anion, which is independent of translational motion.

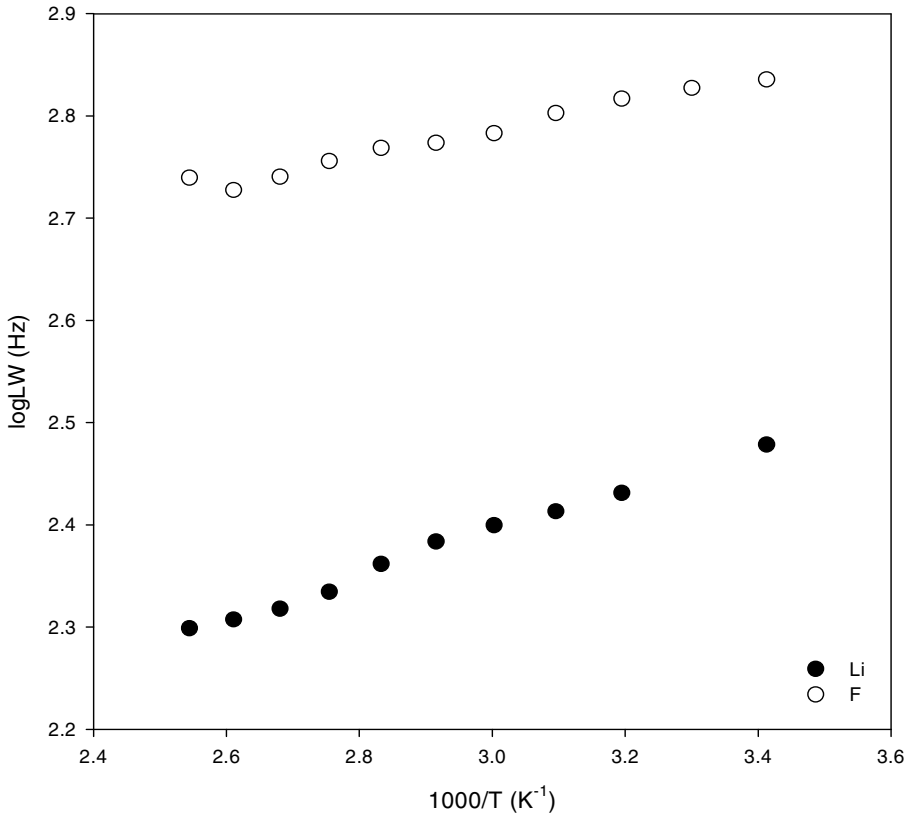

Figure 5.10 - Arrhenius plot of ^{7}Li and ^{19}F NMR linewidths in lithium doped PI–PEO block copolymer.

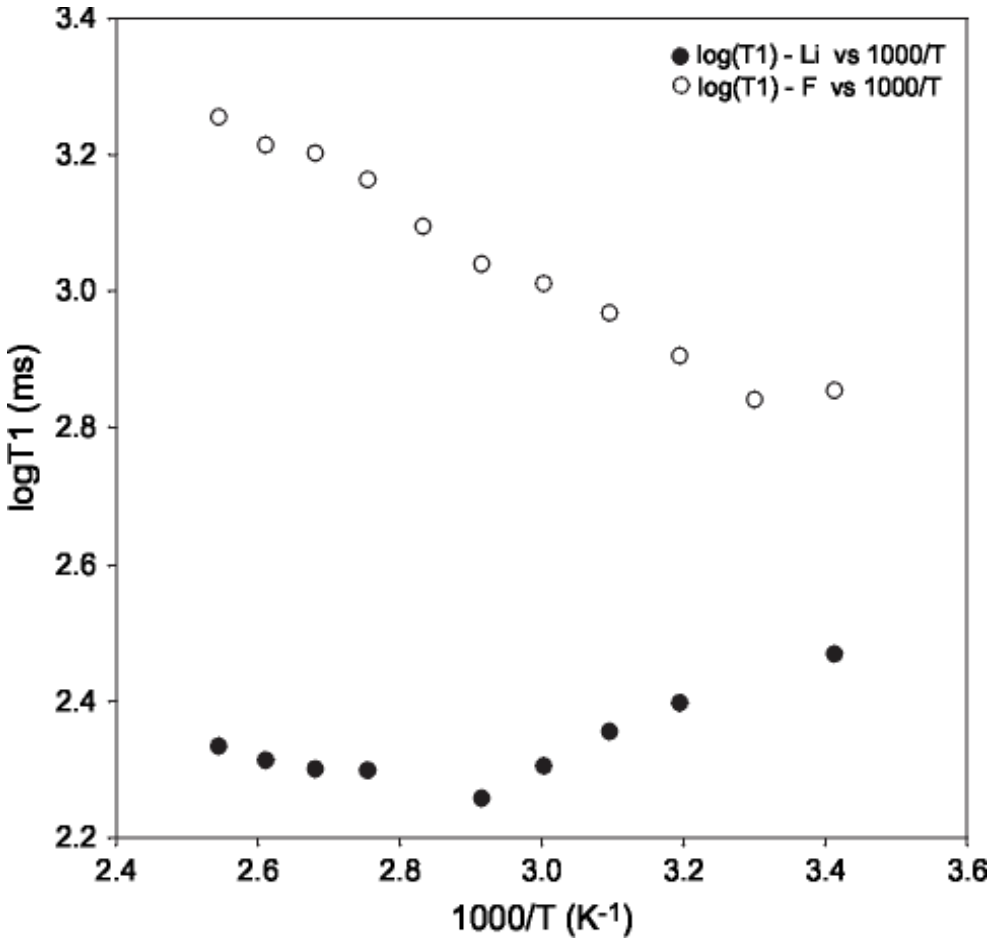

Figure 5.11 - Arrhenius plot of ^{7}Li and ^{19}F NMR spin-lattice relaxation times in lithium doped PI–PEO block copolymer.

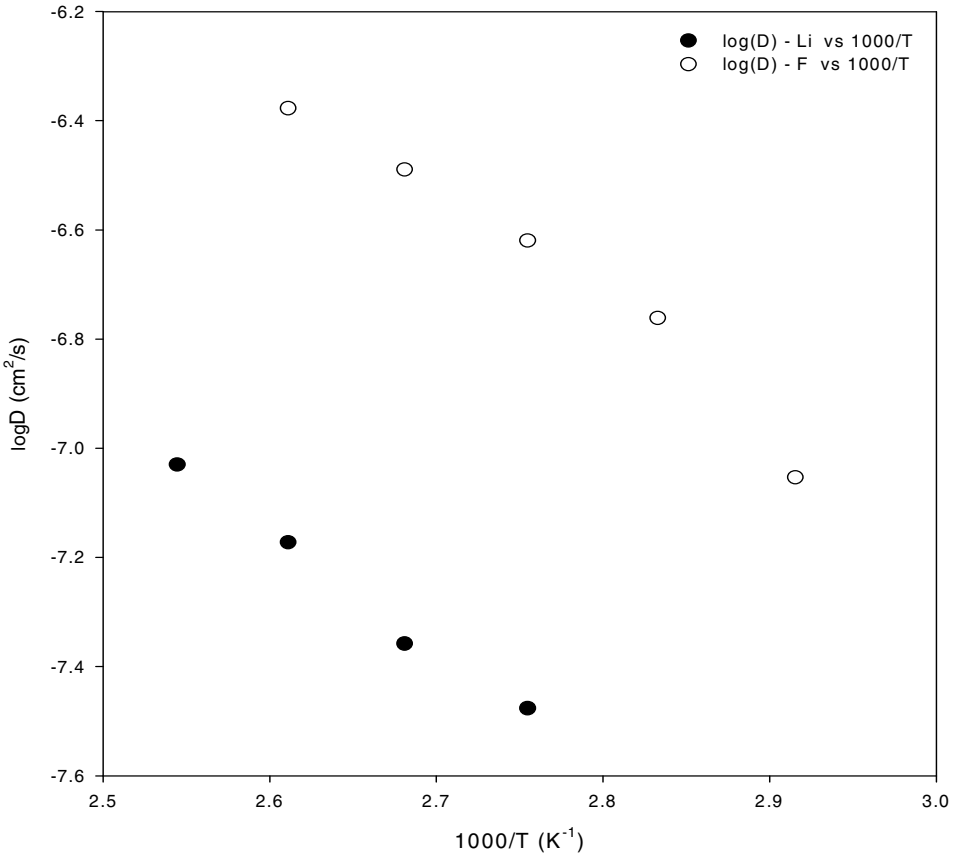

Figure 5.12 - Arrhenius plot of ^{7}Li and ^{19}F NMR self-diffusion coefficients in lithium doped PI–PEO block copolymer.

Finally, the cation and anion diffusion results in Fig. 5.12 indicate similar temperature dependencies, again suggesting that both ionic mobilities are linked

to the common mechanism of polymer segmental motion in the amorphous phase. The anion diffusion is significantly higher than the cation diffusion despite its larger size, consistent with behavior observed for the vast majority of polyether-based polymer electrolytes, and again, a consequence of amorphous phase transport [88], [95] and [99]. In oriented polymer electrolyte systems involving crystalline phase transport, cation conductivities tend to be somewhat higher [100] and [101].

5.4 Conclusions

In summary, the structural analysis via SAXS and AFM combined with the molecular conformation determined by WAXD and DSC experiments have provided experimental evidence to determine the inter- and intra-molecular phase separation of the rod-coil block copolymer from the solution state. It is clear that the nano-confined environment formed by the rods will control PEO melting and crystallization behavior, and most likely helps to maintain an amorphous state for lithium ion conduction in the doped polymers.

Acknowledgements

We thank the Advanced Battery Program of the NASA Glenn Research Center for support of this project. Financial support to Hunter College from the MBRS-RISE (NIH) program and an RCMI (NIH) Infrastructure grant (#RR-03037) are gratefully acknowledged.

Chapter 6: Gel Polymers Incorporating LiBETI Salt and Ionic Liquids*

Abstract

Multinuclear NMR spectroscopy has been used to investigate the structure and mobility of gel polymer electrolytes for applications to lithium-ion batteries and possibly fuel cells. Seven gel electrolytes were studied and each contained a mixture of lithium bis(perfluoroethylsulfonyl)imide (LiBETI) salt and various organic solvents, i.e. ethylene carbonate and gamma butyrolactone. Poly(vinylidene fluoride-co-hexafluoropropylene) (PVDF-HFP) was used as the gel forming polymer. Two of the samples consisted of an ionic liquid component, i.e. 1-n-butyl-3-methylimidazolium (BMI), which had been hypothesized to improve lithium ion mobility. Although wide variations in sample composition were present, we were able to conclude that the addition BMI correlated with a restriction in ionic motion, both cationic and anionic. Further studies need to be carried out preferably with a more selective distribution of solvent and ionic liquid components.

.

*This chapter includes work that is currently unpublished, and is part of a collective study by A. Khalfan, S.G. Greenbaum, F. Croce, and M. Salomon.

6.1 Introduction

Lithium polymer (Li-Poly) batteries have technologically evolved from the conventional Li-Ion batteries. The Li-Poly batteries are currently being used in cellular phones, PDAs and laptops. In a true Li-Poly battery, the electrolyte is a lithium salt complexed in a solid polymer (a plastic-like film) whereas in the Li-Ion battery the electrolyte is a liquid held in a porous separator material. Gel polymer electrolytes for lithium batteries, however, are composed of the lithium salt, various organic solvents, as well as a polymer. In these gel samples, the liquid electrolyte is trapped in a gelled polymer. Gel electrolytes can yield high and stable ionic conductivity values, and they possess fairly good mechanical properties [102].

In all, seven gel electrolytes were investigated. The samples are listed on the next page by composition as received from Dr. Fausto Croce of the Chemistry Department in the University of Rome in Italy.

Table 6.1 – Composition of gel samples.

Sample #	Composition
1	BMITF (ionic liquid), GBL, VC, LiBETI, PVDF 2801
2	EC, GBL, LiBETI, PVDF 2801
20S	EC, GBL, VC, LiBETI, PVDF 2801
25S	EC, PC, VC, GBL, LiBETI, PVDF 2801
26S	GBL, TMP (trimethyl phosphate) VC, LiBETI, PVDF 2801
6	BMITF (ionic liquid), EC, EMC triflate, LiBETI, PVDF
29S	PC, GBL, VC, LiBETI, PVDF

Propylene carbonate (PC or $C_4H_6O_3$), ethylene carbonate (EC or $C_3H_4O_3$), vinylene carbonate (VC or $C_3H_2O_3$), ethyl methyl carbonate (EMC or $C_4H_8O_3$), and GBL (or gamma butyrolactone) or various mixtures of them are all liquid electrolyte components in which the lithium salt (i.e. LiBETI or $LiN(SO_2CF_2CF_3)_2$) is dissolved [103]. PVDF (poly(vinyledene fluoride)) is the host polymer matrix. Samples #1 and #6 both contain BMI (1-n-butyl-3-methylimidazoliumbis(trifluoromethylsulfonyl)imide) triflate or BMITF. BMITF is an ionic liquid, or room temperature molten salt, which offers low volatility and high thermal stability (above 300˚C) [104]. Making comparisons among the samples is difficult because of the limited number of samples made available and the wide variations in composition among the materials.

6.2 Sample Preparation

The gel samples were stored and prepared inside a drybox under argon gas. The gels were somewhat sticky. Each sample was cut into strips and packed into 5 mm (outer diameter) Pyrex tubes that were then flame-sealed. Variable temperature NMR measurements were performed on the CMX-300 MHz spectrometer as previously described. The resonance frequencies used were 116.988 MHz, 283.219 MHz, and 301.021 MHz for ^{7}Li, ^{19}F, and ^{1}H, respectively. The reason for investigating ^{1}H nuclei is to understand the behavior of the solvent molecules. The temperature range investigated for each sample was typically from -50˚C to 60˚C (usually in increments of 10˚C). Samples were allowed to equilibrate for about twenty minutes between temperature changes.

6.3 Results and Discussion

6.3.1 ^{7}Li NMR Measurements

We will begin by discussing the results for the ^{7}Li (I =3/2) measurements. A reference sample of lithium triflate (LiTFSI or $LiCF_3SO_3$) solution was used. Shown in Figure 6.1 are the ^{7}Li spectra of all the samples at room temperature (~22^{o}C) as well as the diffusion values for each sample at that temperature. As can be seen, all ^{7}Li spectra exhibit a single peak and no splittings. The single peak represents the lithium ions in LiBETI.

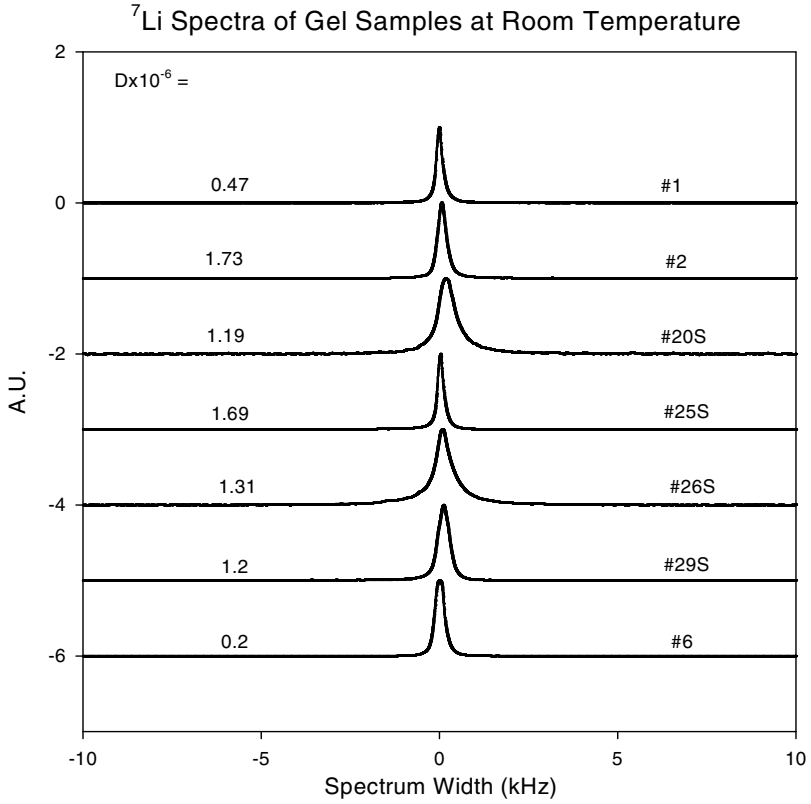

Figure 6.1 – ^{7}Li spectra of gels at room temperature with diffusion coefficients associated with the peaks displayed.

In Figure 6.2, linewidth measurements for the ^{7}Li spectra are shown. All the samples exhibit very little temperature dependence for their linewidths, with the exception of sample #26S which exhibits modest motional narrowing. Magnetic interactions such as dipole-dipole interaction are being averaged out by rapid cation motion. Sample #26 is the only sample from the list that contains TMP, which may be a major factor contributing to the narrowing.

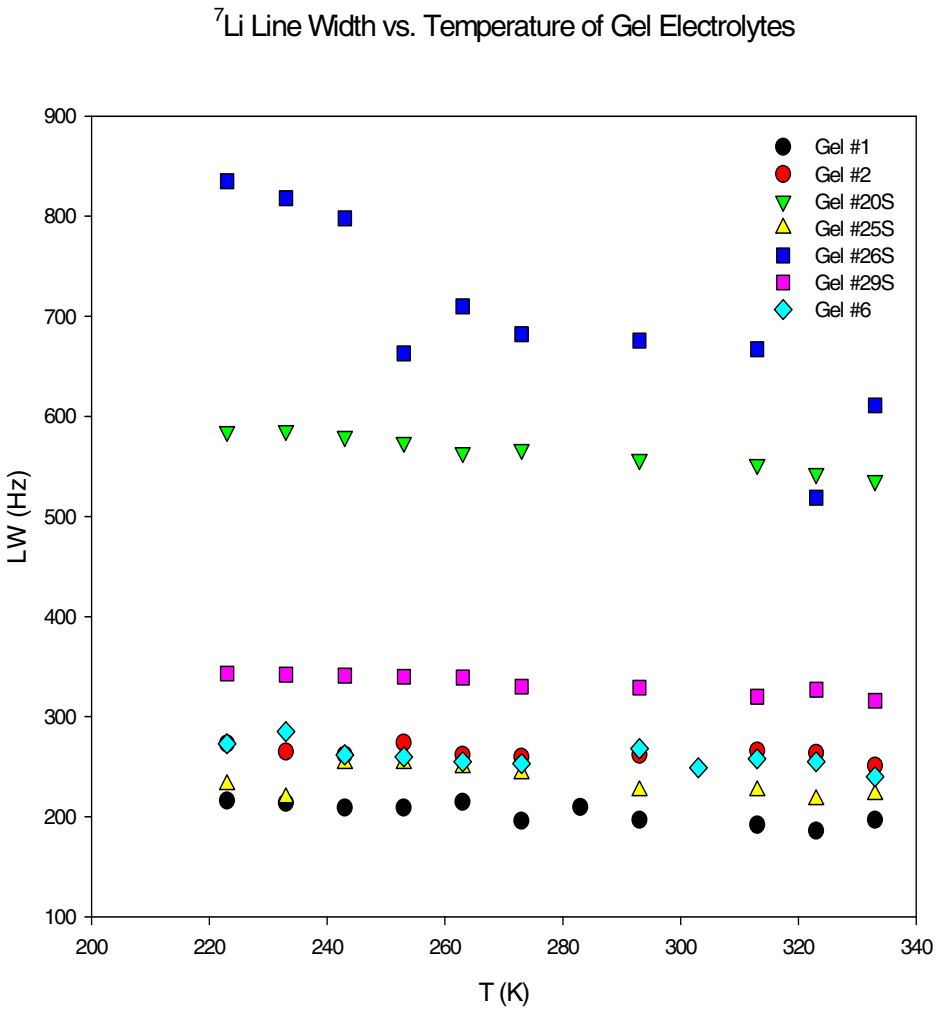

Figure 6.2 – ^{7}Li linewidth measurements for gels.

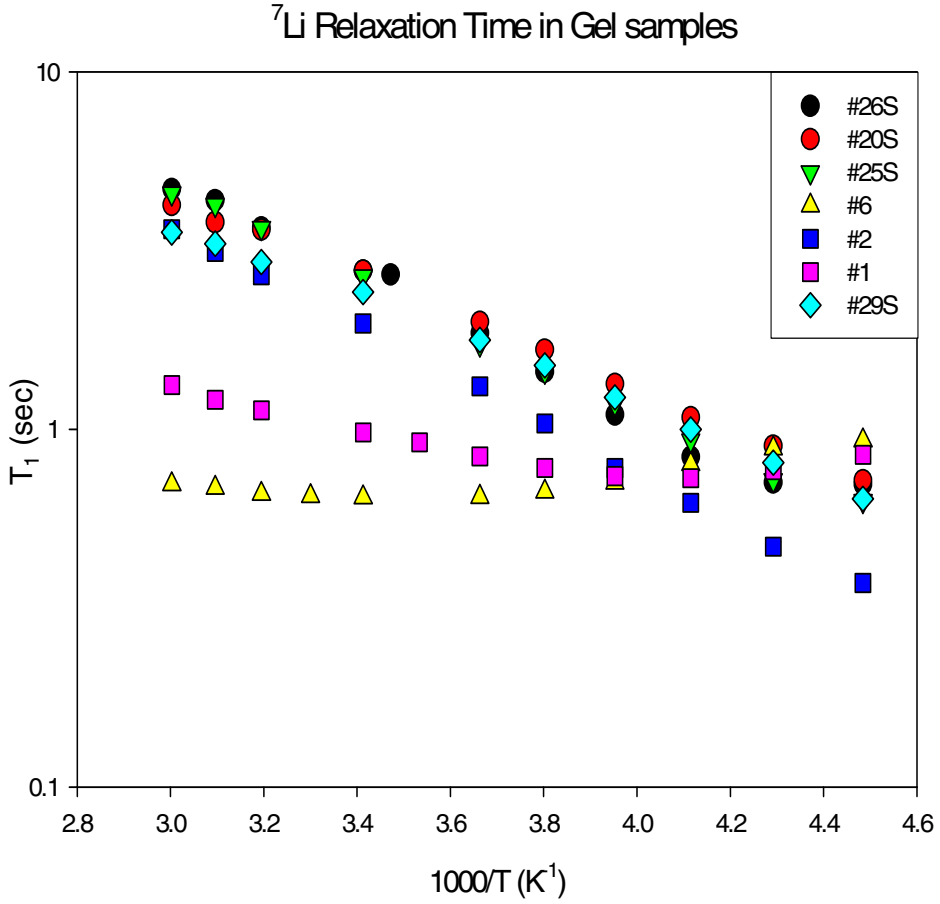

Figure 6.3 – ^{7}Li T_1 in semilog format versus 1000/Temperature.

Figure 6.3 is an Arrhenius plot of the temperature dependence of the spin-lattice relaxation time T_1 for the lithium cation. For all samples other than sample #6, it appears that the T_1 minimum occurs below -50 ° C. Sample #6 does not exhibit a clear minimum suggesting a broad distribution of correlation times. Samples #1 and #6 exhibit the lowest values of T_1. Of the samples examined, only samples #1 and #6 contain the BMI triflate ionic liquid, which apparently plays a dominant role in the lithium relaxation mechanism. The low values of T_1, even at the highest temperatures, imply that

ionic motion is restricted. That is, the other materials show increasing T1 with increasing temperature as $\omega\tau_c$ decreases. Samples #20S, #25S, and #26S have comparable T_1 values throughout the investigated temperature range, and therefore have similar activation energies.

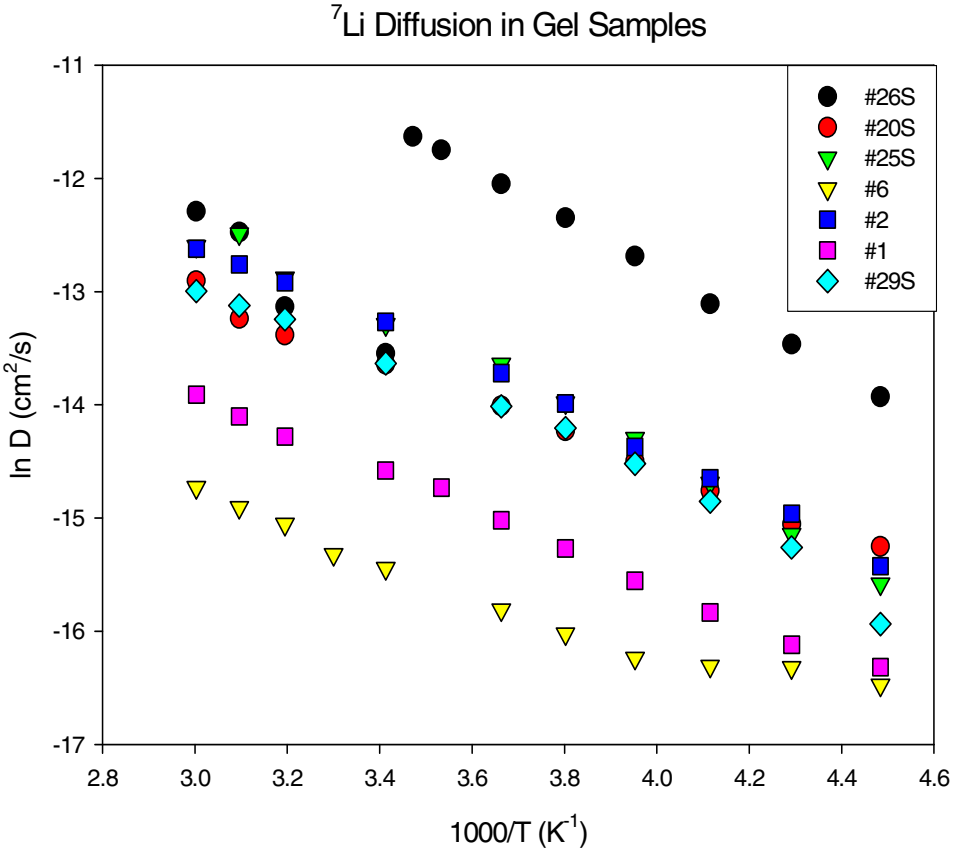

Figure 6.4 – Arrhenius plot of ^{7}Li self-diffusion coefficients in gel electrolytes.

In Figure 6.4, we observe that the lithium ion diffusion of samples #1 and samples #6 are the lowest. At -50 ° C, the diffusion coefficients for both samples #1 and #6 are about the same (around 8 x10^{-8} cm^2/s). As temperature increases, the diffusion coefficient for #1 grows by almost a factor of two in relation to #6, but both yield *D* values on the order of 10^{-7}. *D* values for

samples #20S, #29S, #2, and #25S are fairly comparable in the temperature range investigated although towards 60 ° C, *D* values for #20S and #29S are closer to one another than to the diffusion coefficients for #2 and #25S. Something quite interesting is observed for sample #26S. From -50 ° C to 15 ° C, the lithium cation diffusion is the highest in #26S , but between 15 ° C and 20 ° C , *D* drops sharply and significantly which is probably a result of the TMP component of sample #26S, the only sample to contain TMP. This sudden change in the diffusion coefficient suggests that phase separation occurs in the material at around room temperature.

6.3.2 ^{19}F NMR Measurements

In the ^{19}F (I = ½) room temperature spectra (See Figure 6.5), at least three peaks can be distinguished, except for sample #6. The peak with chemical shift (referenced to aqueous lithium triflate solution) between 0 to 1 kHz (rightmost peak) represents the fluorine atoms of the CF_3 group in LiBETI. The leftmost peak observed for all samples except sample #6 represents the fluorine atoms of the CF_2 group in LiBETI since the BETI anion has been shown to have two widely separated peaks (around 10.5 KHz apart at 282 MHz) [105]. Sample #6 does not have the BETI component, and is therefore consistent with our peak assignments. The smaller and somewhat broader peak with chemical shift between 4-10 kHz (middle peak) arises from the PVDF polymer backbone [106].

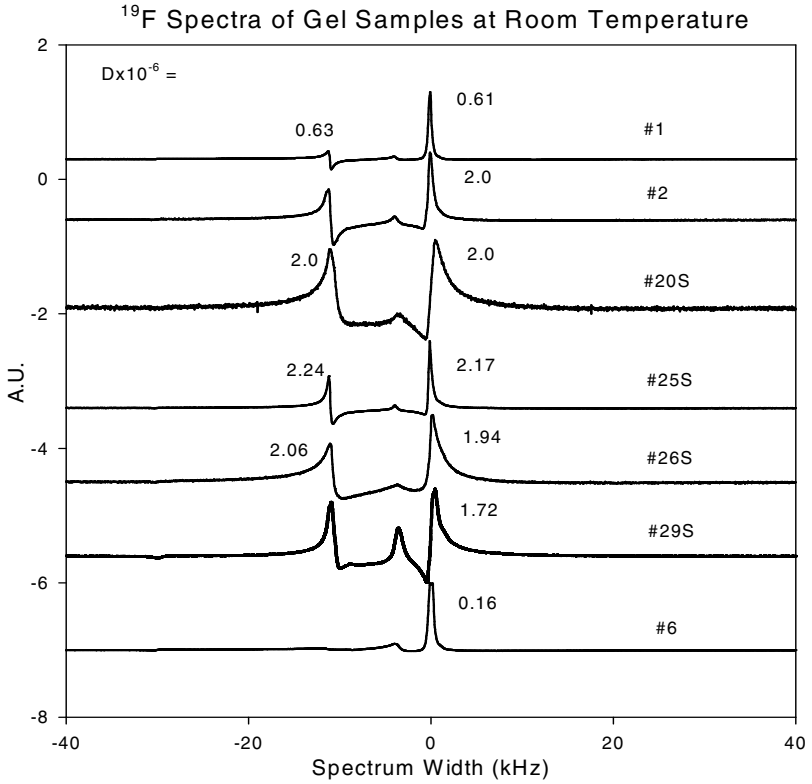

Figure 6.5 – ^{19}F spectra of gels. The diffusion coefficient associated with each peak measured ~22^{o}C is indicated next to the peak.

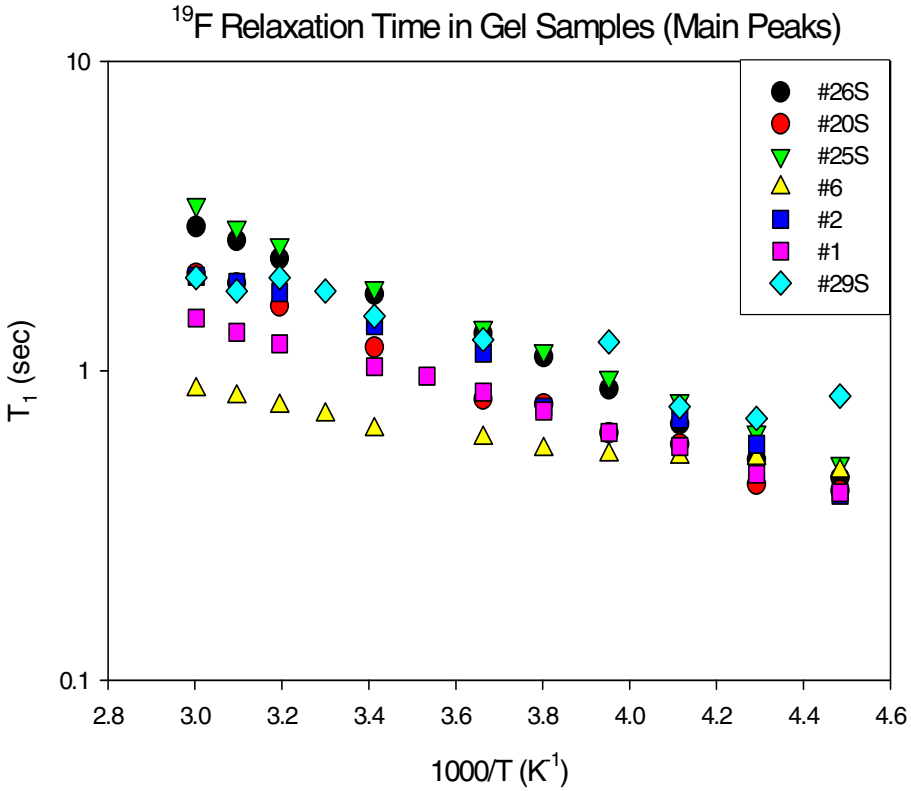

Figure 6.6 – ^{19}F anion spin-lattice relaxation measurements.

T_1 measurements of the fluorine anion, corresponding to the rightmost peaks in Figure 6.5, are shown in Figure 6.6. Once again, samples #1 and #6 have the shortest T_1 values, which is once again indicative of a restriction on molecular motion. On the other extreme, samples #25S and #26S exhibit the longest values for T_1, and they reveal somewhat similar relaxation behavior. These values for T_1 suggest rapid motion due to fast CF_3 rotation. The T_1 behavior for sample #29S seems anomalous since it rises and falls twice.

As for the ^{19}F anion diffusion measurements (See Fig. 6.7), the lowest diffusion value is seen for sample #6. Sample #1 yields a higher diffusion

trend than that of #6. The rest of the samples have comparable diffusion constants and also strongly resemble the diffusion behavior for ^{7}Li ions. From -50 ° C to 20 ° C, the ^{7}Li cation diffusion value for sample #26S is higher than that of any of the fluorine anions, probably in part due to the addition of TMP which may act as an anion receptor. This is significant in that most electrolytes have higher anion than cation diffusion rates.

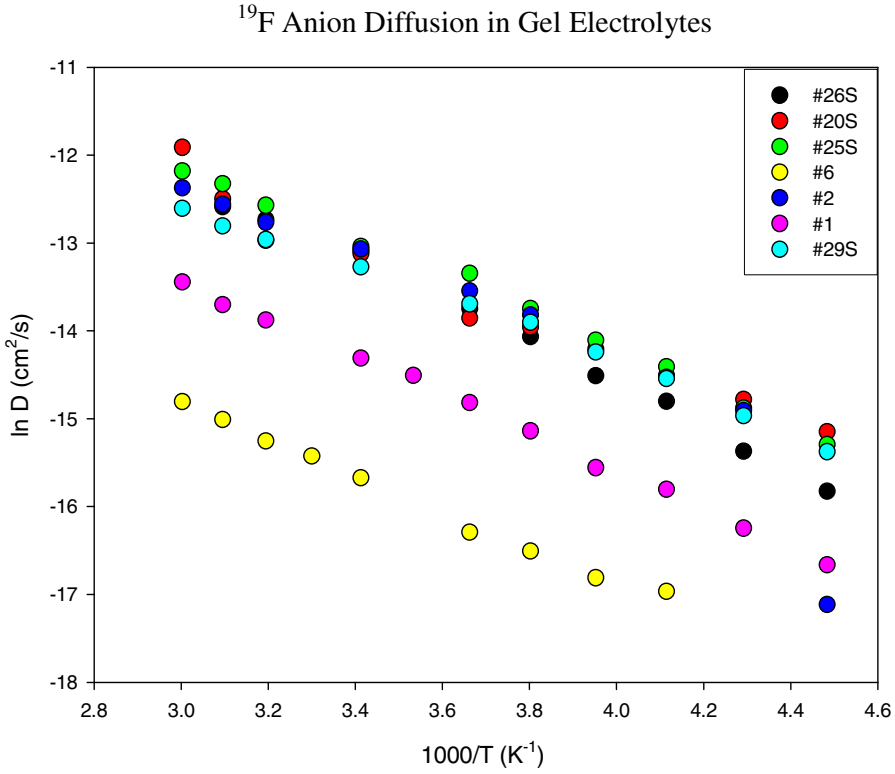

Figure 6.7 - ^{19}F anion diffusion measurements.

6.3.3 ^{1}H NMR Measurements

A reference sample of distilled water was used for ^{1}H measurements. In the ^{1}H NMR spectra, samples #1 and #6 both exhibit a small and somewhat

broad peak at a chemical shift of around 1.2 kHz (Figure 6.8). At around 0 Hz, there seems to be overlapping of spectra due to the different mixtures of solvents. In samples #1, #2, #25S, and #6, the overlapping peaks centered at 0 arise from the protons in the EC, VC and/or GBL solvents. In samples #20S, #26S and #29S, there is even greater broadening. In general, the peaks are broad and unresolved which suggests that there is restricted molecular motion in the gel.

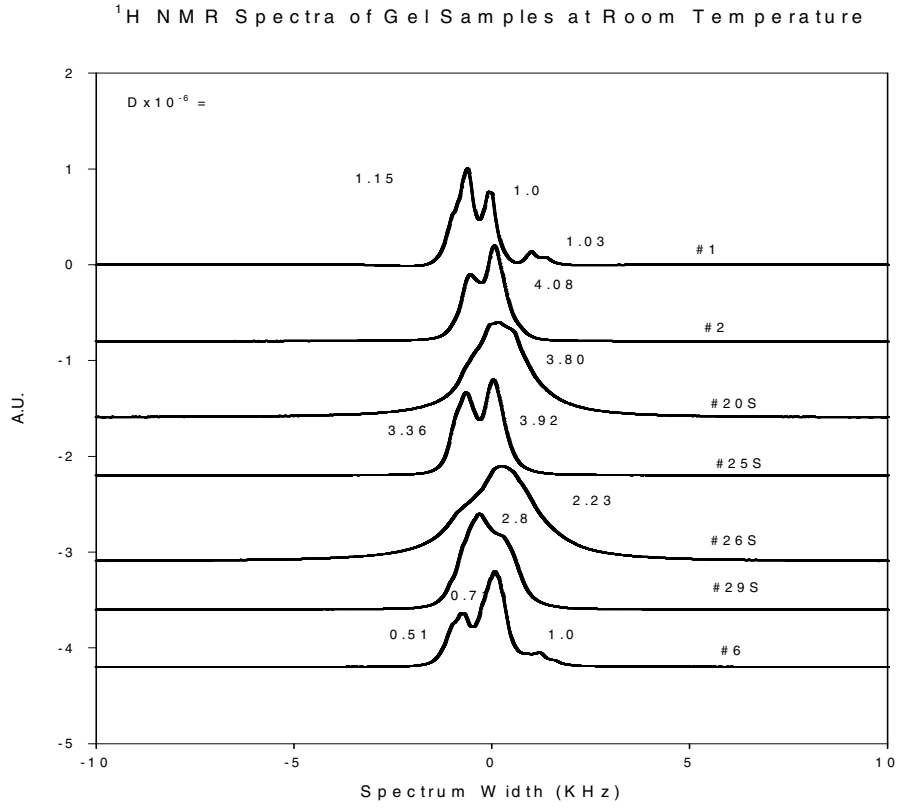

Figure 6.8 - ^{1}H spectra for gel electrolytes with diffusion coefficients associated with each peak listed.

Plotted in Figure 6.9 is the T_1 data for the main peaks (or main contributions to the spectrum, i.e. corresponding to peaks arising between 0-1 kHz). Samples #1 and #6 have the fastest relaxation values again implying relatively low molecular mobility. Samples #26S and #29S exhibit similar relaxation behavior. Samples #2 and #25S also exhibit similar relaxation behavior.

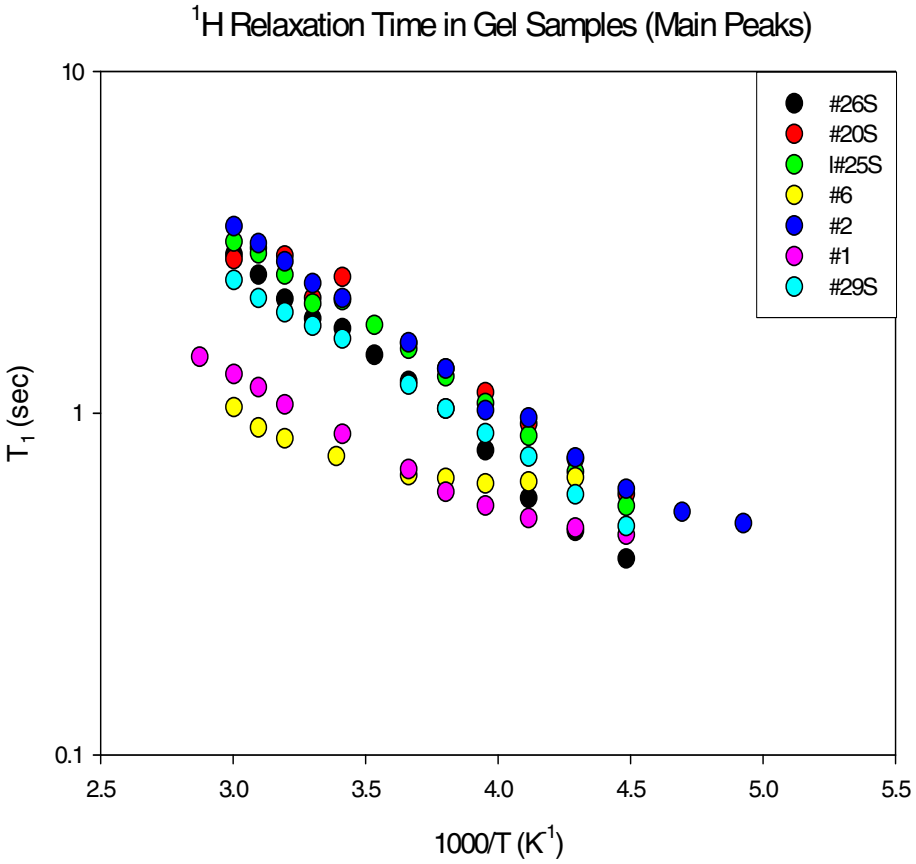

Figure 6.9 - ^{1}H spin-lattice relaxation measurements of main peaks.

For the ^{1}H diffusion data, samples #25S and #2 yield the highest diffusion values, higher than any of the cation and anion diffusion measurements.

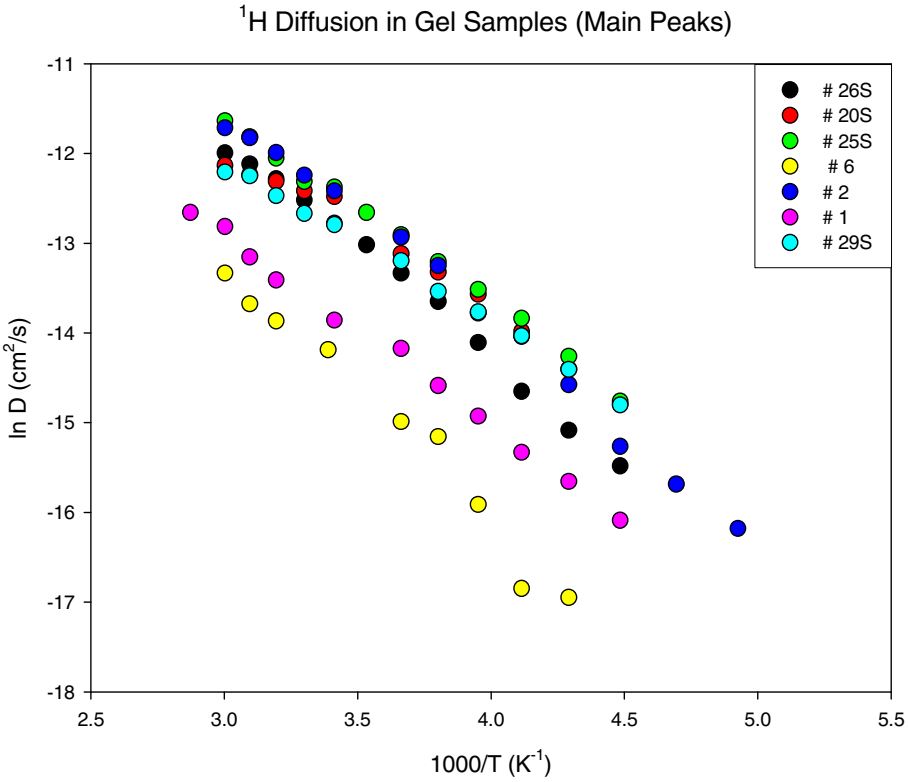

Figure 6.10 – Arrhenius plot for ^{1}H diffusion coefficients.

6.4 Conclusion

Despite the differences in composition with each gel electrolyte, we can conclude that samples #1 and #6 exhibit restricted molecular motion due to their relatively short T_1 values across each nuclei investigated, and this is further evidenced by the low diffusion coefficients (for each nucleus) in both these samples. We may infer that the BMI ionic liquid component is the cause for the observed behavior of samples #1 and #6. In addition, sample #26 possesses the highest lithium cation diffusion rate from -50 ° C to just below room temperature, which is greater than any of the fluorine anion diffusion rates. This behavior is unusual yet desired for purposes of lithium battery

operation. As for the sudden drop in the Li^+ diffusion coefficient in sample #26, we believe there may be a phase separation that arises but are unsure as to the exact source of it.

Chapter 7: Novel Li Ion Conducting Polymer Gel Electrolytes Based on Ionic Liquid / PVDF-HFP Blends*

Abstract

Ionic liquids thermodynamically compatible with Li metal are very promising for applications to rechargeable lithium batteries. 1 -Methyl-3 Propylpyrrolidinium bis(trifluoromethanesulfonyl)imide (P_{13}TFSI) is screened out as a particularly promising ionic liquid in this study. Dimensionally stable, elastic, flexible, non-volatile polymer gel electrolytes (PGEs) with high electrochemical stabilities, high ionic conductivities and other desirable properties have been synthesized by dissolving Li imide salt (LiTFSI) in P_{13}TFSI ionic liquid and then mixing the electrolyte solution with poly(vinylidene-co-hexafluoropropylene) (PVDF-HFP) copolymer. Adding small amounts of ethylene carbonate (EC) to the polymer gel electrolytes dramatically improves the ionic conductivity, net Li ion transport concentration, and Li ion transport kinetics of these electrolytes. They are thus favorable and offer good prospects in the application to rechargeable Li batteries including open systems like Li/air batteries, as well as more "conventional" rechargeable lithium and lithium ion batteries.

*This work constitutes a paper that has been approved for publication in the Journal of the Electrochemical Society with A. Khalfan, S.G. Greenbaum, H. Ye, J. Huang, and J.J. Xu as contributing authors.

7.1 Introduction

As it is well known, Li is the most electropositive and lightest metal, and thus has the greatest theoretical specific capacity of 3860 Ah/kg [107], [108]. This has attracted worldwide efforts of researchers and manufacturers to develop advanced battery technologies based on lithium. To date, the rechargeable lithium ion battery has already been one of the best choices in view of specific capacity and cycle stability [107]. However, rechargeable lithium metal batteries with even higher specific capacities are still unavailable in the market, especially lithium/air batteries which possess the highest theoretical specific energy (as high as 13,000 Wh/g, excluding the oxygen from the air). Conventional Li/air batteries based on aqueous electrolytes suffer from fast capacity loss due to corrosion of lithium by water and are also non-rechargeable. Abraham and Jiang [109] first reported a rechargeable lithium/oxygen cell using organic polymer gel electrolytes and demonstrated its advantages such as an all solid state design, rechargeablity and a high capacity. Read [110] studied the effect of electrolyte and air cathode formulation on the electrochemical properties of an Li/O_2 organic electrolyte cell and found that electrolyte composition has the largest effect on discharge capacity and rate capability. Both groups incorporated common organic solvents in the electrolyte, i.e. ethylene carbonate (EC), propylene carbonate (PC), 1,2-dimethoxyethane (DME), diethyl carbonate (DEC), dimethyl carbonate (DMC), γ-butyrolactone (γ-BL), tetrahydrofuran (THF) or tetrahydropyran (THP) [109], [110]. The highly reactive lithium metal cannot, however, be thermodynamically compatible with common organic solvents. The fact that the air cathode of Li/air cells must be open to the ambient

environment poses considerable additional challenges in improving the properties of the electrolytes being used, such as meeting the requirements of little to no volatility, moisture insensitivity and air stability. Our efforts are concerned with developing suitable electrolytes with good lithium interface stability, high electrochemical stability, high ion conductivity and low-volatility for not only lithium/air batteries but also the more "conventional" rechargeable lithium and lithium ion batteries.

Recently, the resurgence of ionic liquids, especially those that are air stable, has drawn the attention of researchers in the electrochemical field [111-119]. Ionic liquids are room-temperature molten salts typically consisting of bulky, asymmetric organic cations and inorganic anions. The important attributes of ionic liquids include a wide electrochemical window, high ionic conductivity, and high thermal stability [114], [120]. In addition, it is evident that employing ionic liquid as a solvent can safely enhance the performance of lithium based cells, particularly large-scale batteries and Li/air batteries, because of the liquid's nonflammable and nonvolatile nature. Webber et al. have enumerated the advantages of ionic liquids for lithium-ion and related batteries [114]. More significantly, some ionic liquids with a certain combination of cation and anion have recently been reported as being electrochemically stable in the presence of lithium metal, as opposed to conventional organic solvents. Ionic liquids that have been determined as such include quaternary ammonium salts [115], [121], [122], pyrrolidinium salt [115], [116], [123], [124], piperidinium salts [115], and some multi-substituted imidazolium salts [125], [126] as well. Furthermore, most investigated ionic liquids of these salts consist of the bis(trifluoromethanesulfonyl)imide anion

($TFSI^-$). Coulombic cyclic efficiency of Li plating/stripping close to 100% has been obtained from using these ionic liquids as electrolyte solvents [115], [116], [124]. A $Li/LiCoO_2$ cell prototype containing the piperidinium-TFSI salt [115] and another containing quaternary ammonium-TFSI salt [122] both show very good performance and large utilization of the positive electrode material at the same time [115]. $Li/LiFePO_4$ and Li/V_2O_5 cells incorporating polymer gel electrolytes consisting of poly(ethylene oxide), LiTFSI and pyrrolidinium-TFSI salt also demonstrated exceptional performance (at 40 ^oC) [127], [128]. Concerning the characteristics of electrochemical stability and ionic conductivity, the work of this paper will screen out pyrrolidinium-TFSI salt as a promising solvent and focus on the application of this ionic liquid to the electrolyte of lithium batteries.

The investigated Li-salt/ionic liquid electrolyte consists of three ions, i.e. Li ion, the cation of the ionic liquid and the same anion from both the Li salt and ionic liquid. It needs to be emphasized that in this system, all ions being transported contribute to the ionic conductivity, but only Li ion transport is relevant for the charge/discharge of Li (ion) batteries. Unfortunately, NMR studies have shown that the self-diffusion coefficients of the cation of the ionic liquid are equal to or higher than those of the anion depending on the anion [129]. And in the system of $LiBF_4/EMIBF_4$, the smallest Li ion diffuses slowest, while the EMI cation always diffuses fastest [130]. There is still no clear explanation of this phenomenon. Hayamizu et al. proposed that the Li^+ and BF_4^- form ion complexes and diffuse together while EMI^+ becomes relatively freer to move [130]. Be that as it may, the transport of other ions may lead to cell polarization, which will reduce high rate performance of the

batteries. It is very important to increase Li ion transport in these new Li-salt/ionic liquid complexes. Interestingly, Zwitterion studied 1-butylimidazolium-3-(n-butanesulphonate), which is a type of salt similar to ionic liquid but with a higher melting point (152 ^{o}C), and found that the addition of the salt can improve lithium-ion transport dramatically in the LiTFSI/1-methyl-3-propylpyrrolidinium imide (P_{13}TFSI) electrolyte[131], [132]. In this paper, we investigated the effect of ethylene carbonate (EC) as an ion dissociation enhancer to improve Li ion transport due to its high dielectric constant and relatively good thermal stability (EC has a boiling point above 240^{o}C). In fact, ethylene carbonate is used as a co-solvent in commercial electrolytes for lithium ion batteries because it can provide an effective protective layer on the surface of graphite to prevent continuous electrolyte reduction [107]. The formed SEI (Solid Electrolyte Interphase) film also prevents the co-intercalation of the organic cation of the ionic liquid, another potential problem in the application of ionic liquid [133], [134]. It is reasonable to expect the addition of EC will also facilitate the formation of a protective film on the carbon black of the cathode, allowing Li ions to pass through while protecting the catalyst layer on the air-electrode side from the ionic liquid organic cation.

Currently most research regarding the applications of ionic liquids is on lithium-ion or lithium batteries based on liquid electrolyte systems, yet polymer electrolytes are preferable for suppressing dendrite growth and meeting all-solid state requirements of the cells. And it has been noted that ionic liquids have strong interactions with many polymers [116], [135-138]. Shin et al. have reported that the dry solid polymer electrolyte consisting of

high molecular weight polyethylene oxide (PEO), LiTFSI and P_{13}TFSI reaches an ionic conductivity of ~10^{-4} S/cm at 20 ^{o}C, almost two orders of magnitude higher than that of ionic-liquid-free PEO-LiTFSI electrolyte [116]. However, the hydrophilicity of PEO will preclude its application to the Li/air cell in which PEO will be in direct contact with moisture. PVdF-based polymer electrolytes are expected to be highly anodically stable when one considers ~~of~~ the strongly electron-withdrawing functional group (-C-F) that is present [139]. A copolymer of vinylidene fluoride with hexafluoropropylene (PVDF-HFP) is capable of trapping large amounts of liquid electrolyte while retaining the advantage of PVDF by sustaining sufficient mechanical integrity for the processing of freestanding films. Moreover, PVDF-HFP possesses good hydrophobicity. In fact, PVDF-HFP is the polymer choice for Bellcore's plastic Li-ion batteries [140]. Furthermore, dimensionally stable, elastic, flexible, polymer gel electrolytes with desirable mechanical strength and properties can be readily synthesized by mixing ionic liquids with PVDF-HFP [135], [136], [141].

In this paper, P_{13}TFSI has -first been screened out as a promising solvent from four ionic liquids (as shown in Scheme 1), i.e. 1-Ethyl-3-Methylimidazolium bis(trifluoromethanesulfonyl)imide (EMITFSI), 1-Propyl-2,3-Dimethylimidazolium bis(trifluoromethanesulfonyl)imide (PMMITFSI), 1-methyl-3-propylpyrrolidinium bis(trifluoromethanesulfonyl)imide (P_{13}TFSI), and 1-Methyl-3-Propylpiperidinium bis(trifluoromethanesulfonyl)imide (PP_{13}TFSI) through cyclic voltammetry testing. Then, polymer gel electrolyte membranes with different LiTFSI/P_{13}TFSI concentration have been prepared through blending with

PVDF-HFP polymer. Ionic conductivity and ion transport properties as a function of LiTFSI concentration have been characterized for these membranes. The effect of small amounts of EC on the lithium ion transport and other electrochemical properties will also be discussed subsequently in the 1M LiTFSI/*x*EC+(1-*x*)P_{13}TFSI/PVDF-HFP complex systems. Thermal analysis and pulsed gradient spin-echo (PGSE)-NMR was undertaken to understand the mechanism of ionic transport in these novel polymer gel electrolytes. Moreover, preliminary solid-state, thin-film Li/oxygen cells were constructed using the investigated polymer gel electrolyte membrane and their performances were analyzed.

7.2 Experimental

7.2.1 Materials

1-Methylimidazole, 1,2-Dimethylimidazole, N-Methylpyrrolidine, N-Methylpiperidine, 1-Bromopropane, 1-Bromoethylane, anhydrous acetonitrile, anhydrous ethylene carbonate, anhydrous acetone were purchased from Sigma-Aldrich and used as received. Battery grade Lithium foil is from FMC. Poly(vinylidene fluoride-co-hexafluoropropylene) (PVDF-HFP), KYNAR 2801, was kindly provided by ATOFINA Chemicals. Lithium bis(trifluoromethylsulfonyl)imide (LiTFSI) was kindly provided by Minnesota Mining and Manufacturing Company and dried under vacuum at 90℃ for 24 hours prior to use.

7.2.2 Synthesis of Ionic Liquids

All hydrophobic ionic liquids were prepared according to a two-step procedure, quaternization and then anion-exchange reaction [111], [141], [142]. The synthesis of P_{13}TFSI has been shown in Scheme 7.1 as an example. First N-Methyl pyrrolidine is reacted with the 1-bromopropane to obtain N-Methyl-N-Propyl pyrrolidinium bromide. Then room temperature ionic liquids were obtained by anion exchange reactions of N-Methyl-N-Propyl pyrrolidinium bromide with lithium imide. The ionic liquid product was purified by recrystallization, active carbon treatment, and then dried under vacuum at 70℃ for 24 hours before using.

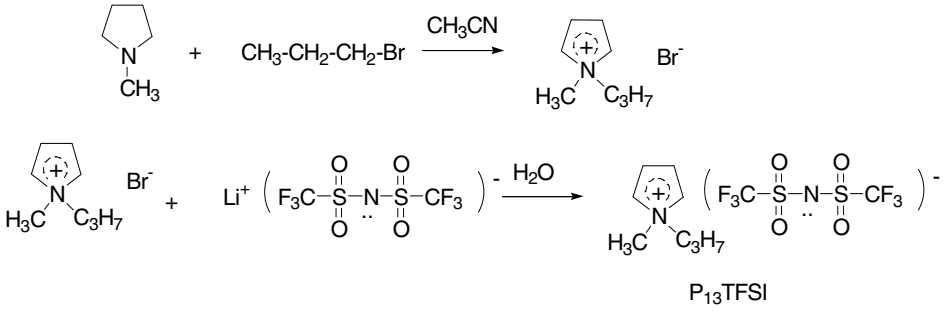

Scheme 7.1 - Schematic illustration of the synthesis process of P_{13}TFSI ionic liquid.

7.2.3 Preparation of Polymer gel electrolyte Membranes

Polymer gel electrolyte membranes were prepared by the solution casting method. First, LiTFSI salt was dissolved into ionic liquid or ionic liquid/EC solution to form liquid electrolyte with proper lithium salt concentration. The resulting ionic liquid solution was then mixed with 7.5 wt% PVDF-HFP acetone solution resulting in a viscous mixture. The weight ratio of the Li

salt/ionic liquid (w/EC) solution to PVDF-HFP was set at 7:3. Finally the mixture solution was cast over a Teflon tray, and the acetone was subsequently evaporated under vacuum to result in a freestanding polymer gel electrolyte membrane. All preparation steps were carried out in an argon-circulating glove box.

7.2.4 Measurements

The ionic conductivity of ionic liquids and Li salt/ionic liquid solutions were measured by Oaklon Conductivity Meter (with nominal cell constant of 1.0). Electrochemical characterizations were carried out by using the Solartron 1287 electrochemical interface combined with 1260 impedance/gain-phase analyzer. The electrochemical stability windows of ionic liquids and Li salt/ionic liquid (w/EC) solutions were determined by cyclic voltammetry test with a scan rate of 10 mV/s while using Pt as both the working electrode and the counter electrode with AgCl/Ag as the reference electrode. The AgCl/Ag electrode was prepared by electrochemical depositing an AgCl layer on a polished Ag rod from saturated NaCl solution. The temperature dependence of ionic conductivity was determined by ac impedance with a frequency range from 10 Hz to 1 MHz with an amplitude of 5 mV. A conductivity testing cell was set up by sandwiching the polymer gel electrolyte membrane (12.7 mm in diameter and approximately 150 μm thick) between two stainless-steel (SS) discs and sealing the configuration inside of the Hohsen Test Cell (Hohsen Corporation, Japan). The measurements were performed from 80℃ to -20℃ using an environment chamber (B-M-A, Inc.) as the temperature control. Cyclic voltammetry tests were carried out by using either a symmetric cell -

Li/polymer gel electrolyte/Li, or an asymmetric cell - SS/polymer gel electrolyte/Li, to demonstrate the reversible equilibrium of Li/Li^+. The scanning rate was 10 mV/s between 1.0 V and -1.0 V vs. Li^+/Li, in which the SS working electrode was a freshly polished stainless steel disc. The electrochemical stability of the polymer gel electrolyte was evaluated by means of a linear potential sweep using the SS/polymer gel electrolyte/Li cell, in which SS acts as the working electrode and a Li disc acts as both the counter electrode and reference electrode. The scanning range is from an open circuit potential to 6.5 V vs. Li^+/Li with a scan rate of 1.0 mV/s.

The thermal stability of polymer gel electrolytes was measured by Thermal Gravimetric Analysis (Perkin-Elemer TGA7). The measurement was carried out from room temperature to 200 ^oC under N_2 flow environment with a heating rate of 10 ^oC/min. Differential Scanning Calorimetry (DSC) was performed with a Q1000 DSC System from TA Instruments, Inc. The measurement was carried out from -50 ^oC to 150 ^oC at a heating and cooling rate of 10 ^oC /min. A cooling-heating-recooling cycle was carried out first, and DSC data were collected during the subsequent heating step.

^1H, ^7Li, and ^{19}F NMR techniques were used to investigate the ion transport of polymer gel electrolytes over the temperature range of 20 ^oC to 120 ^oC. Here ^1H, ^7Li, and ^{19}F were detected as NMR-sensitive nuclei corresponding to the P_{13}, Li, and TFSI ion components of the polymer gel electrolyte. NMR measurements were performed on a Chemagnetics CMX-300 spectrometer in conjunction with a JMT superconducting magnet of field strength 7.1 T. The Larmor frequencies for ^1H, ^7Li and ^{19}F were 300.0, 116.9 and 283.2 MHz, respectively. Measurements were carried out on ~500-mg samples which were

inserted and packed into 5-mm Pyrex tubes in a very low humidity (<5 ppm) dry-box (VAC). The Pyrex tubes were flame sealed under vacuum to prevent any contamination from outside air and moisture. Self-diffusion coefficients of different ions (P_{13}, Li, and TFSI) were obtained by the pulse gradient spin-echo (PGSE) technique (PGSE-NMR), which uses the Hahn spin-echo pulse sequence [143] but with the inclusion of gradient pulses. Gradient strengths (g) ranged from 10 to 200 G/cm. Pulse widths were ~5 μs for ^{7}Li and ~10 μs for ^{1}H and ^{19}F. A Nalorac Z-Spec gradient probe and also a Doty gradient probe were used to facilitate diffusion measurements. The experimental parameters Δ (gradient delay) and δ (gradient duration) ranged from 45 to 100 ms and 15 to 25 ms, respectively, for ^{7}Li, and from 25 to 350 ms and 1 to 7 ms, respectively, for ^{19}F and ^{1}H. Gradient calibration was accomplished using pure distilled water at 25°C at which $D=2.29\times10^{-5}$ cm^2/s. The frequency reference used for both ^{7}Li and ^{19}F was a saturated $LiCF_3SO_3$ aqueous solution, and distilled water served as the ^{1}H reference. The value of the self-diffusion coefficient was calculated by plotting the echo attenuation (E) according to Equation (3-1) for a single diffusing species in an isotropic medium [144],

$$E=\exp(-\gamma^2 g^2 \delta^2 D(\Delta-\delta/3)) \quad (7.1)$$

where γ is the gyromagnetic ratio, g is the gradient strength, δ is the duration of the gradient pulse, and Δ is the interval between the gradient pulses.

7.2.5 Fabrication and Testing of Li/O_2 Cells

The Li/oxygen cell was fabricated by sandwiching a LiTFSI/P_{13}TFSI/PVDF-HFP polymer gel electrolyte membrane between a Li foil and an air electrode. The air electrode was prepared by spraying a catalyst/carbon black ink onto a wet-proof E-TEK carbon paper followed by heat treatment. The prepared air electrode consisted of 2.12 wt% cobalt phthalocyanine, 82.88 wt% Vulcan carbon black and 15 wt% PTFE as binder. The Li anode side of the cell was sealed, and the air electrode side open to flowing oxygen (flow rate about 25 ml/min). The current density used for discharge and charge of the cell was 0.05 mA/cm^2 air electrode. The cutoff voltage for discharge and charge were 2.0 and 4.1 V, respectively.

7.3 Results and Discussion

7.3.1 Screening of the Ionic Liquids

As mentioned in the introduction section, in most cases, the investigated Li-salt/ionic liquid electrolyte has the same anion in both the Li salt and ionic liquid. This is due to solubility issues. In our preliminary study, it was found that the solubility of Li salt in the ionic liquid incorporating the same anion is much higher than those systems with different anions. For example, N-Ethyl-Methyl imidazolium trifluoromethanesulfonate (EMITf) can dissolve only 0.3 mol/l of LiTFSI, EMITFSI can dissolve around 0.2 mol/l of Lithium trifluoromethanesulfonate (LiTf), whereas EMITFSI can dissolve up to 2 mol/l of LiTFSI. Moreover, the solubility of LiTf in the EMITf is also rather low, about 0.3 mol/l, which highlights the advantage of using highly dissociable LiTFSI salt. In this paper, our study begins with four hydrophobic ionic liquids, all with TFSI anion, i.e. EMITFSI, PMMITFSI, P_{13}TFSI and

$PP_{13}TFSI$ as shown in Scheme 7.2, to select a suitable ionic liquid for further study.

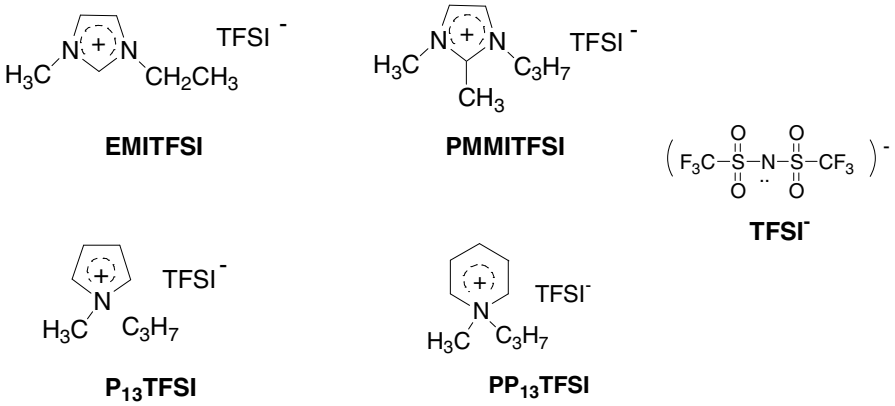

Scheme 7.2 - Molecular structure of four investigated ionic liquids.

Having a wide electrochemical stability window is a pre-requisite property of the solvent for lithium batteries, especially good cathodic stability in view of highly active lithium. Cyclic voltamogram tests have been carried out to determine the stability window for different kinds of ionic liquids. Fig. 7.1 (a) shows the electrochemical stability windows of these four ionic liquids. The abnormal current fluctuation of $P_{13}TFSI$ at potentials more negative than -3.5 V (vs. AgCl/Ag) may be due to the fast and unstable decomposition of the ionic liquid. The weak anodic current around 0.9 V for $PP_{13}TFSI$ in the forward scan may be due to some impurity or a decomposition product resulting from the reduction reaction of the ionic liquid. Fig 7.1(b) gives the electrochemical window of pure ionic liquid $P_{13}TFSI$, 1 M LiTFSI / $P_{13}TFSI$ electrolyte solution, and electrolyte solution with 20 wt% EC (percentage corresponding to total weight of EC and $P_{13}TFSI$). The cathodic stability limit and anodic stability limit are defined as the potential point corresponding to

cathodic current density or anodic current density up to 1mA/cm^2, respectively. The values of them are listed in Table 7.1**.** From best to worst, the order of cathodic stability is: $PP_{13}TFSI$ > $P_{13}TFSI$ > PMMITFSI > EMITFSI. The anodic stability from best to worst is: $P_{13}TFSI$ > $PP_{13}TFSI$ > PMMITFSI >EMITFSI. Both $PP_{13}TFSI$ and $P_{13}TFSI$ have very wide electrochemical stability windows with values around 5.9 V. As far as the cathodic stability limit is concerned, these values are -3.25 V and -3.07 V vs. AgCl/Ag for $PP_{13}TFSI$ and $P_{13}TFSI$, respectively. Fig 7.1 (b) shows Li^+/Li reduction at -3.11 V vs. AgCl/Ag in the 1M LiTFSI/$P_{13}TFSI$ and at -3.04 V vs. AgCl/Ag in the 1M LiTFSI/0.2EC+0.8$P_{13}TFSI$ electrolyte. If we include the possibility of over-potential delay of Li^+/Li reduction in the investigated electrolyte, the redox potential of Li^+/Li would be more positive than -3.04 V vs. AgCl/Ag in the investigated ionic liquids. Both $PP_{13}TFSI$ and $P_{13}TFSI$ are therefore stable enough for Li^+/Li reduction reaction. It is clearly shown in Fig 7.1 (a) that the reduction stability of EMITFSI is insufficient for the Li batteries, about 1.1 V positive against Li/Li^+. This result is consistent with the literature [115], [145]. It was reported that the proton at the C2-position of imidazolium cation is subject to chemical reduction [126]. Alkyl substitution of this proton can improve its reduction ability as reported by Sutto et al [126]. Here PMMITFSI shows improved reduction stability, but still cannot meet the reduction limitation of Li^+/Li.

Table 7.1 Electrochemical stability limit and ionic conductivity of different ionic liquids and electrolyte solutions.

Ionic liquids	σ (mS/cm)	$E_{cathodic}$ (V vs. AgCl/Ag)	E_{anodic} (V vs. AgCl/Ag)
EMITFSI	8.52	-1.90	2.31
PMMITFSI	2.55	-2.16	2.38
P_{13}TFSI	3.62	-3.07	2.82
PP_{13}TFSI	1.73	-3.25	2.68
1M LiTFSI/P_{13}TFSI	-	-3.11	2.73
1MLiTFSI/0.2EC+0.8P_{13}TFSI	-	-3.04	2.52

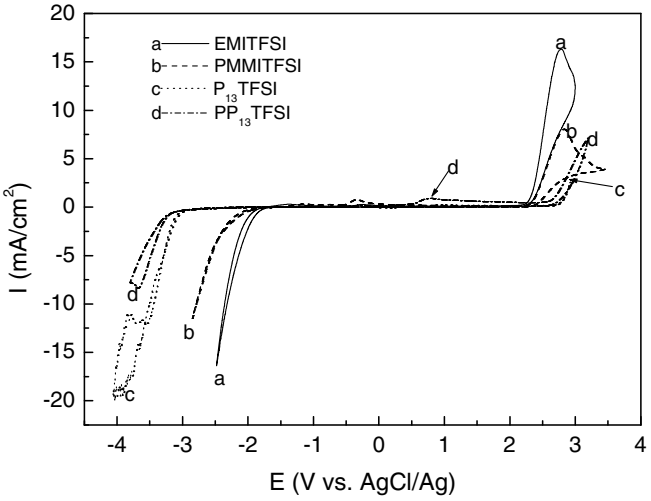

(a)

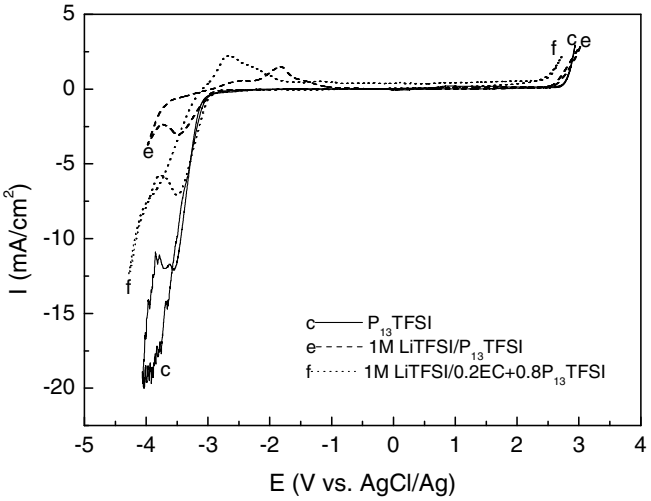

(b)

Fig. 7.1 Electrochemical stability windows of ionic liquids or electrolyte solution (a) Cyclic Voltammograms for different ionic liquids; (b) Cyclic Voltammograms for P_{13}TFSI, 1M LiTFSI/P_{13}TFSI, and 1M LiTFSI/0.2EC+0.8P_{13}TFSI).

As shown in Fig 7.1(b), adding LiTFSI slightly increases the reduction stability of P_{13}TFSI, the lithium deposition process occurs before the decomposition of P_{13}TFSI. The peak around -3.50 V vs. AgCl/Ag is due to a Li plating reaction, which has corresponding stripping peak at -1.82 V vs.

AgCl/Ag. The following current increase at a potential below -3.76 V vs. AgCl/Ag may be ascribed to the decomposition of the ionic liquid itself. There are also two shoulders appearing at ~ -2.47 V and ~ -1.44 V vs. AgCl/Ag corresponding to a Li stripping process. Multi stripping peaks may imply different characteristics of Li layers plated on the Pt rod (0.5 mm diameter). However, the continuous reduction current increase below -3.07 V vs. AgCl/Ag for P_{13}TFSI can be attributed to its decomposition and no anodic peak shows up at the potential above -3.0 V vs. AgCl/Ag. Adding a small amount of EC does not change the reduction stability of electrolyte significantly but slightly decreases the anodic stability of the electrolyte as shown in Fig. 7.1 (b). More interestingly, adding a small amount of EC also more than doubles the Li plating/stripping peak current density (also around -3.50 V vs. AgCl/Ag), which demonstrates that the addition of EC can enhance the Li ion transport in the electrolyte. The stripping of lithium in the electrolyte with EC is also facilitated. The stripping peak appears around -2.66 V vs. Ag^+/Ag with one shoulder at -2.23 V *vs.* Ag^+/Ag, thus showing lower over potentials than those of the electrolyte without EC.

7.3.2 LiTFSI/P_{13}TFSI/PVDF-HFP Polymer gel electrolytes

Dimensionally stable, elastic, flexible, polymer gel electrolytes with desirable mechanical strength and other desirable properties can be readily synthesized by mixing Li salt/ionic liquids with PVDF-HFP. Polymer gel electrolyte membranes with different LiTFSI concentrations show similar morphologies and mechanical properties. Fig. 7.2 gives a representative picture of 1M LiTFSI/P_{13}TFSI/PVDF-HFP polymer gel electrolyte membrane.

PVDF-HFP copolymer matrix retains the LiTFSI/P_{13}TFSI very well, up to 70 wt%, and the liquid electrolyte in the membranes is difficult to squeeze out under pressure. Good mechanical properties of the PVDF-HFP based electrolyte membrane also benefits the battery assembly process.

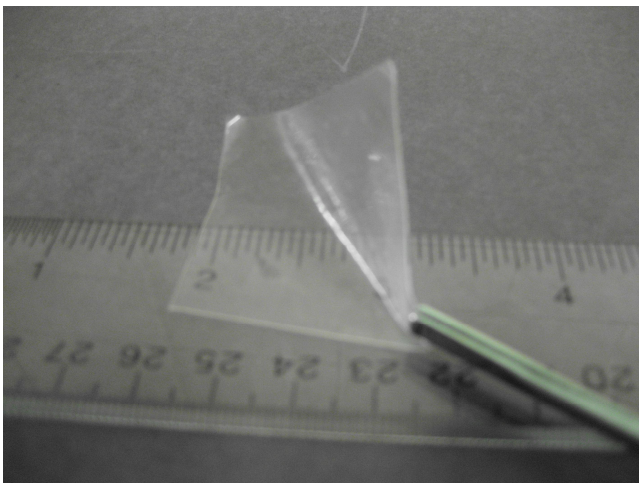

Fig. 7.2 Photograph of 1M LiTFSI/P_{13}TFSI /PVDF-HFP polymer gel electrolyte membrane.

Fig. 7.3 shows the temperature dependence of the ionic conductivity of P_{13}TFSI/PVDF-HFP and *x* M LiTFSI/ P_{13}TFSI /PVDF-HFP (*x* = 0.1, 0.2, 0.5, and 1) membranes. LiTFSI/P_{13}TFSI/PVDF-HFP polymer gel electrolytes show good ionic conductivities above 0^{o}C albeit lower than those of P_{13}TFSI/PVDF-HFP. For example, the ionic conductivities of 0.5M LiTFSI/P_{13}TFSI/PVDF-HFP reaches 0.05 mS at 0^{o}C, 0.27 mS at room temperature, and larger than 1.1 mS above 60 ^{o}C. These data are two orders of magnitude higher than conductivity values of PEO-Li salt complex, and these membranes uphold the same advantage of containing no volatile solvents.

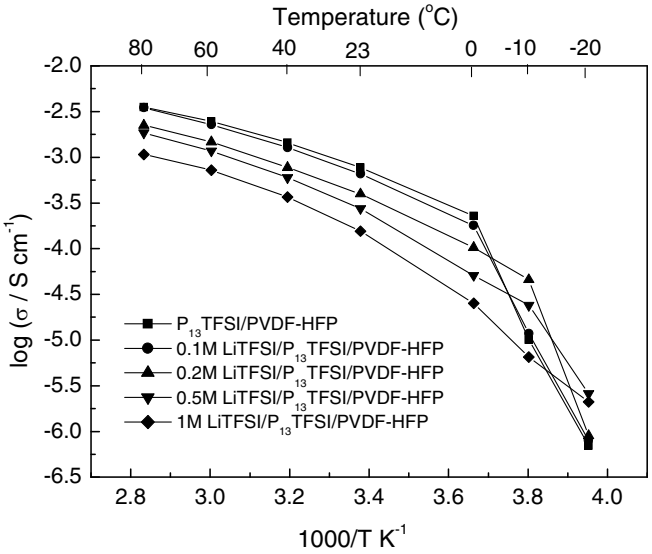

Fig. 7.3 Temperature dependence of the ionic conductivity of P_{13}TFSI/PVDF-HFP and *x*M LiTFSI/ P_{13}TFSI /PVDF-HFP (*x*=0.1, 0.2, 0.5, and 1) membranes.

As seen in Fig. 7.3, the higher Li salt concentration leads to lower ionic conductivity of the membrane at the temperatures above 0°C. The temperature dependent ionic conductivity of the polymer gel electrolyte with pure ionic liquid (i.e. P_{13}TFSI/PVDF-HFP) is very similar to that of the polymer gel electrolyte with very low LiTFSI concentration (0.1M LiTFSI/P_{13}TFSI/PVDF-HFP). These results are widely reported for liquid electrolytes, the explanation being that adding Li salt increases the viscosity of the liquid electrolyte. For the polymer gel electrolyte membrane containing the highest content of liquid electrolyte, here P_{13}TFSI ionic liquid functions as both a plasticizer for the polymer matrix (note: LiTFSI can also plasticize the polymer due to its high charge delocalization feature) and a solvation medium for electrolyte salt. PVDF-HFP provides mechanical support and dimensional stabilization through polymer chain entanglements and/or chemical cross-linking. Polymer

(gel) electrolytes possess both the cohesive properties of solids and the diffusive transport properties of liquid electrolytes at the same time due to their unique hybrid network structure [139]. Fig. 7.3 also shows that temperature dependent ionic conductivities (logσ vs. 1/T) of the polymer gel electrolytes exhibit non-Arrhenius VTF behavior at temperatures $\geq 0^{o}$C. This behavior is similar to that of PEO-based lithium ion conducting polymer gel electrolytes, in which ion transport is related to the segmental motion of the polymer chain [146]. At temperatures below 0^{o}C, however, the polymer gel electrolyte without Li salt or with lower Li salt concentration ($\leq$ 0.5 mol/l) shows an abrupt conductivity drop. The presence of more Li salt concentration moves this sudden drop to a lower temperature. This phenomenon becomes insignificant for the polymer gel electrolyte with 1mol/l LiTFSI in P_{13}TFSI. The conductivity drop may result from the ionic liquid or Li salt/ionic liquid undergoing a freezing transition. Additional evidence of this can be observed from DSC measurements, which will be discussed later. The drop in conductivity indicates that incorporating LiTFSI can suppress the recrystallization/melting process of Li salt/ionic liquid, as has been found for Zn salt/ionic liquid complex [141]. To extend the application temperature range of Li batteries, it is preferable to use a high Li salt concentration.

Fig. 7.4 shows the cyclic voltammograms of symmetric Li/PE/Li cells for the membranes with different Li salt concentration. CV test starts with reduction scanning, i.e., Li plating first. The first cycle shows a slightly lower plating current density, which may be due to an activation step and/or the formation of metal lithium. Highly reversible Li plating/stripping at the Li/PE interface was observed for all membranes after the second cycle. Reversible Li

plating/stripping clearly indicate that Li^+ ions are mobile in the PE membranes containing Li salts, and Li is capable of dissolution into and deposition from these membranes. As seen in Fig. 7.4, the increase of Li salt concentration leads to the increase of plating/stripping peak current densities. The appearance of the current density peak is due to a balance between a high over potential driving force and the concentration diffusion limit. High peak current densities ensure a high rate discharge/charge capability, so high Li salt concentration in the membrane is beneficial for the rate capability of lithium batteries. Although higher Li salt concentration leads to lower ionic conductivity as shown in Fig. 7.3, it is surmised that the increase of Li salt concentration improves the Li ion transport number. However, Li salt concentration cannot be too high because it leads to low conductivity due to high ionic association. Furthermore, Li salt cannot dissolve homogenously in P_{13}TFSI at a concentration above 1.5mol/l as experimentally observed.

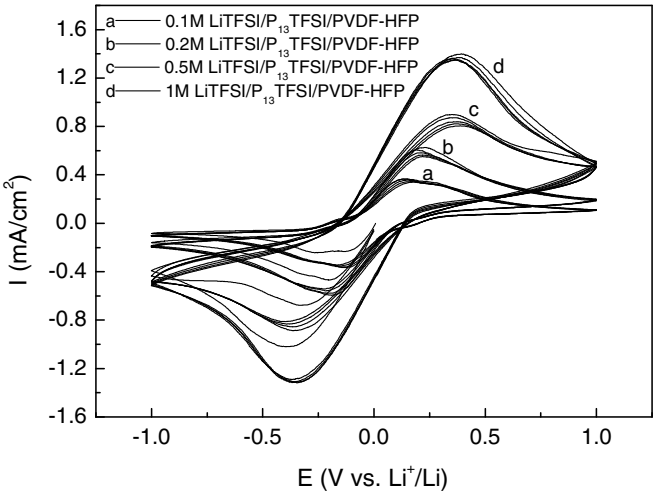

Fig. 7.4 Cyclic voltammograms of symmetric Li/PE/Li cells for the *x*M LiTFSI/P_{13}TFSI/PVDF-HFP (*x*=0.1, 0.2, 0.5, and 1) membranes, scan rate: 10mV/s.

The fundamental understanding of the ionic transport mechanism of Li salt/ionic liquid complex, especially in the polymer gel electrolyte, is still not well understood. NMR has been reported as a powerful method in determining the ionic diffusion coefficient and the degree of ionic association in the liquid system of ionic liquid or $LiBF_4$/$EMIBF_4$ [129], [130]. Arrhenius plots of the self-diffusion coefficient of Li (D_{Li}), both in the Li salt/ionic liquid and in the polymer gel electrolyte membranes with different Li salt concentration, are shown in Fig. 7.5 (a). Arrhenius plots of the self-diffusion coefficient of the different ions in the underscored 1M LiTFSI/P_{13}TFSI/PVDF-HFP polymer gel electrolyte are shown in Fig. 7.5 (b).

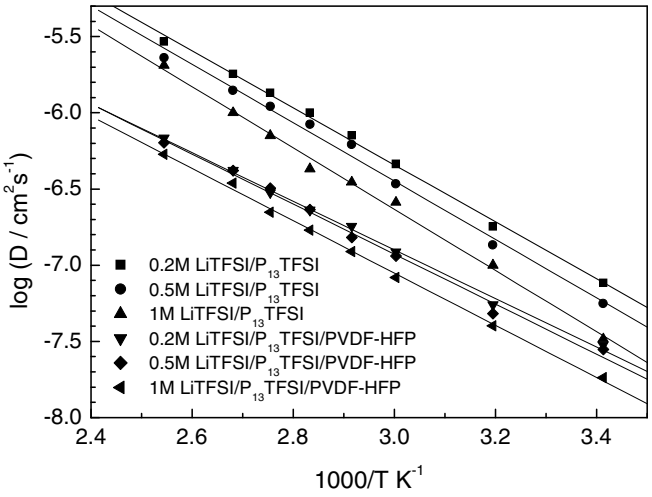

(a)

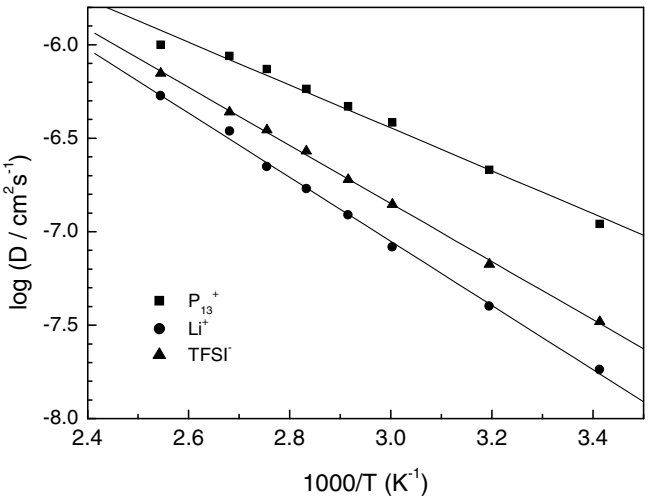

(b)

Fig. 7.5 Arrhenius plots of the self-diffusion coefficient of Li, P_{13}, and TFSI ((a) Self-diffusion coefficient of Li in *x* M LiTFSI/P_{13}TFSI solution and in *x* M LiTFSI/P_{13}TFSI/PVDF-HFP membranes (*x* = 0.2, 0.5, and 1); (b) Self-diffusion coefficient of Li, P_{13}, and TFSI in the 1 M LiTFSI/P_{13}TFSI/PVDF-HFP membrane).

As shown in Fig. 7.5 (a), Li^+ ions are mobile both in the LiTFSI/P_{13}TFSI solutions and in the membranes blended with PVDF-HFP although the value of D_{Li} is smaller in the polymer gel electrolytes than in the binary ionic liquids for any specific Li salt concentration. There is a linear relationship between

$\log(D_{Li})$ and 1/T either binary ionic liquid or polymer gel electrolyte in the temperature range of 20 ^{o}C to 120 ^{o}C. In both the binary ionic liquids and the corresponding polymer gel electrolytes, increasing the Li salt concentration leads to a decrease in the self-diffusion coefficient of Li ion. The behavior suggests, once again, that an increase of Li salt concentration increases the viscosity of the electrolyte. The investigated LiTFSI/P_{13}TFSI systems follow an inverse correlation between the self-diffusion coefficient of Li ion and viscosity as described by Stokes-Einstein equation [129].

$$D=kT/c\pi\eta r \tag{7.2}$$

where k is Boltzmann's constant, T is the absolute temperatures, c is a constant, and r is the effective hydrodynamic or Stokes radius. The activation energy of Li self-diffusion slightly increases with Li concentration. Also, the results of the binary ionic liquid systems are in agreement with results obtained by Hayamizu and co-workers [130].

Fig. 7.5 (b) compares the self-diffusion coefficient of the different ions in the specified 1M LiTFSI/P_{13}TFSI/PVDF-HFP polymer gel electrolyte. Unfortunately, the smallest Li ion diffuses the slowest and the biggest organic cation P_{13} diffuses faster than TFSI, which is similar to results reported in the literature [129], [130]. These results are, however, somewhat different to results most recently reported by Nicotera et al [147], who show that TFSI moves faster than P_{13}, and P_{13} moves faster than Li. Referring to the work of Hyamizu et al [130], a possible explanation for the observed diffusive behavior in Fig. 7.5(b) is that the small Li^+ ion has strong attraction with $TFSI^-$ anion, and may be coordinated with multiple $TFSI^-$ ions, at the same time, P_{13}^+ cations are freed from the $TFSI^-$ anion. As a result, P_{13}^+ motion is less

encumbered by $TFSI^-$ association than Li^+. Further study of the ion transport mechanism of these polymer gel electrolytes is underway. From a practical point of view, it is very important to improve the Li ion transport properties so as to improve the rate capability of the lithium batteries because other ions will polarize the electrode. Suppose all ionic species are free, i.e. no ion-pairs and no ion association exist, the NMR transference number for Li in the polymer gel electrolyte can be calculated by the following equation [130]:

$$t_{Li} = \frac{N_{Li}D_{Li}}{N_{Li}D_{Li} + N_{TFSI}D_{TFSI} + N_{P_{13}}D_{P_{13}}} \tag{7.3}$$

where N denotes number of charge carriers. In the case of 1M LiTFSI/P_{13}TFSI/PVDF-HFP, at 20 ^oC, the calculated $t_{Li+,NMR}$ is only 0.034, too low for battery application. Of course, the ion transport mechanism is not the same under NMR testing as under the battery charge/discharge cycling. In the NMR experiment, we attain an average self-diffusion coefficient of the ions and associated ions. In the battery, only net ions contribute to the conductivity. It is important to improve the Li ion transport in these novel polymer gel electrolytes. Adding EC into the electrolyte should improve the dissociation of Li ion in view of its very high dielectric constant (89.79) [148]. Moreover, Fig. 7.1(b) already shows that adding small amounts of EC more than doubles the Li plating/stripping peak current density. It is worthwhile to study the effect of EC on the performances of this polymer gel electrolyte system.

7.3.3 Effect of EC on the Performances of 1M LiTFSI/P_{13}TFSI/PVDF-HFP

As discussed above, the polymer gel electrolyte with high Li salt content provides high plating/stripping peak current densities, in other words, high concentration of active working ion. In this section, we fix the LiTFSI concentration at 1mol/l of P_{13}TFSI or of P_{13}TFSI + EC co-solvent (5 wt%, 10 wt%, and 20 wt% of EC in the co-solvent). The content of PVDF-HFP is still fixed at 30 wt% of the total polymer gel electrolyte membrane. The actual calculated percentages of EC in the investigated membranes are then 0 wt%, 2.9 wt%, 5.8 wt%, and 11.6 wt%. The physical appearance of the membranes with EC is the same as the membrane without EC, i.e. freestanding, elastic, flexible, translucent polymer membranes.

Arrehnius plots of the ionic conductivity of the polymer gel electrolyte with different content of EC are shown in Fig. 7.6. The ionic conductivity of the polymer gel electrolyte increases with an increase of the EC content. For example, the ionic conductivities of the polymer gel electrolyte with 11.6 wt% EC reaches 0.01 mS/cm at -20 ^{o}C, 0.5 mS/cm at room temperature and about 1 mS/cm at 40 ^{o}C. These values are typical of polymer gel electrolytes with common organic solvents PC, EC, DEC, and others [139].The increase in ionic conductivities of the polymer gel electrolytes can be ascribed to the high dielectric constant of EC, which enhances the ionic dissociation of the LiTFSI and P_{13}TFSI and thus improves the concentration of free ions contributing to conduction. Moreover, the value of log(σ) decreases smoothly from 80^{o}C to -20^{o}C, i.e. no abrupt dropping occurs, and all plots exhibit VTF behavior. The

behavior also reflects that EC functions as a plasticizer in the polymer gel electrolyte.

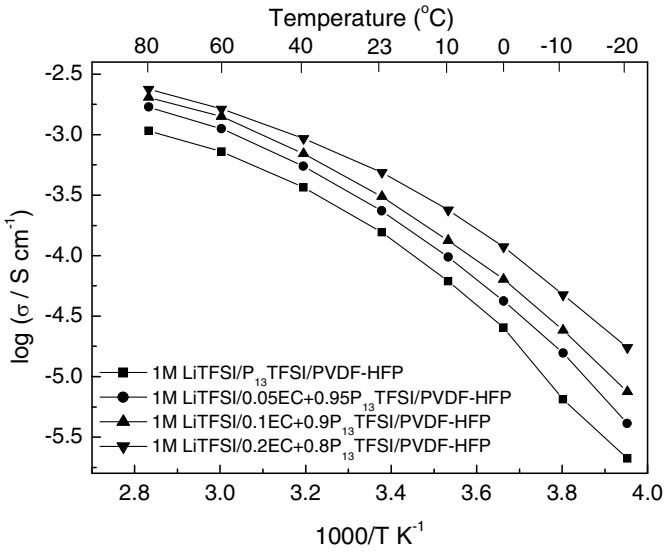

Fig.7. 6 Temperature dependence of the ionic conductivity of 1 M LiTFSI /*x*EC+(1-*x*)P_{13}TFSI / PVDF-HFP (*x*=0, 0.05, 0.1, and 0.2) membranes.

To clearly demonstrate the plating/stripping of Li, polished stainless steel (SS) was implemented as the working electrode of the cyclic voltammogram test cell, with Li foil serving as the counter electrode and reference electrode. Fig. 7.7 (a) shows the cyclic voltammograms of asymmetrical SS/PE/Li cells for the membranes with different EC content. All polymer gel electrolyte membranes show reversible Li plating/stripping. Adding EC improves the Li plating/stripping current densities. Higher EC content correlates with a higher plating/stripping current density of the polymer gel electrolyte ~~is~~. The highest plating/stripping current densities for the film with highest EC content are 2.0 mA/cm^2 and 2.2 mA/cm^2, respectively, almost a factor of three time greater

than those values of the membrane without EC. Fig. 7.7 (b) is a plot of the first ten cyclic voltammograms (Li plating/stripping) cycles of the polymer gel electrolyte, shown as charge density vs. time. For comparative purposes, only 1M LiTFSI/0.2EC+0.8P_{13}TFSI/PVDF-HFP and 1M LiTFSI/P_{13}TFSI/PVDF-HFP are plotted. For both polymer gel electrolytes, the coulombic efficiency increases gradually in the initial cycles and reaches a stable efficiency at the sixth cycle. The stable coulombic efficiency of the 1M LiTFSI/0.2EC+0.8P_{13}TFSI/PVDF-HFP is ~83%, a little lower than that of 1M LiTFSI/P_{13}TFSI/PVDF-HFP (about 92%). However, there is a continuous increase of the plating charge (Q_p) of 1M LiTFSI/0.2EC+0.8P_{13}TFSI/PVDF-HFP in the first ten cycles. The Q_p of 1M LiTFSI/P_{13}TFSI/PVDF-HFP, on the other hand, decreases slightly during the first five cycles, and then reaches a constant after the fifth cycle. And the Q_p of 1M LiTFSI/0.2EC+0.8P_{13}TFSI/PVDF-HFP is almost six times that of the polymer gel electrolyte without EC at fifth cycle. The coulombic loss during each plating/stripping cycle may due to poor contact between inter deposited Li layer on the SS and polymer gel electrolyte, as evidenced by a thin gray-black layer on the SS after dissembling the CV test cell. The formation of SEI film on the SS is also a possible reason and needs to be further investigated. Fig. 7.7 (a) and (b) clearly demonstrate that adding EC enhances the Li ion transport dramatically.

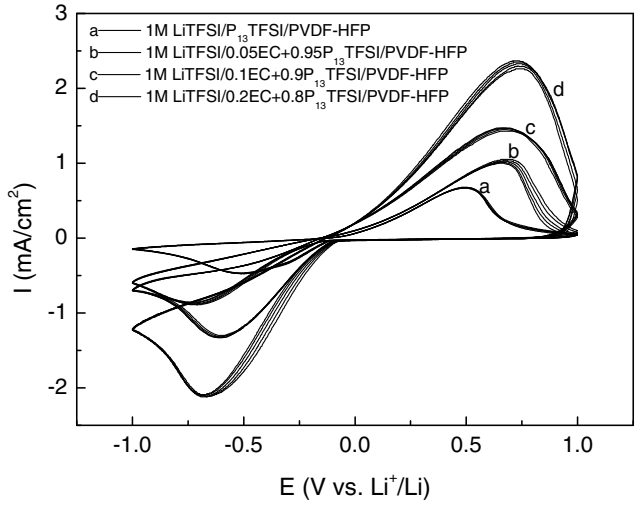

(a)

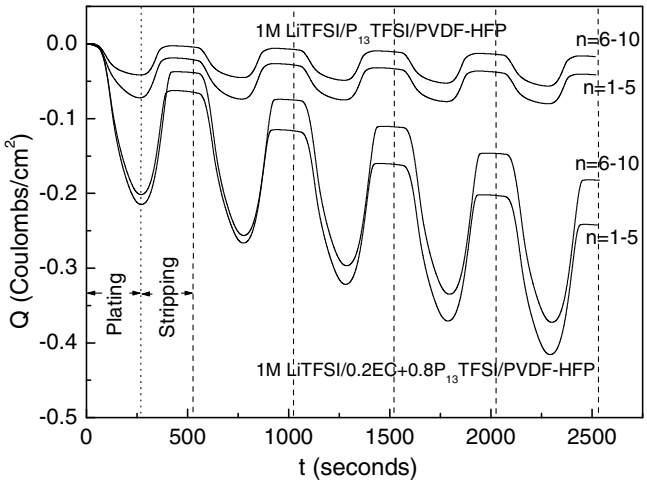

(b)

Fig. 7.7 Cyclic voltammograms of asymmetrical SS/PE/Li cells, 1M LiTFSI/*x*EC+(1-*x*)P_{13}TFSI/PVDF-HFP (*x*=0, 0.05, 0.1, and 0.2) membranes ((a) I vs. E plots of the 6th to 10th cycles, (b) Q-t plots of the first 10 cycles for selected two polymer gel electrolytes).

Fig. 7.8 compares the self-diffusion coefficient of different ions (D_{Li}, D_{P13} and D_{TFSI}) in the 1M LiTFSI/0.2EC+0.8P_{13}TFSI/PVDF-HFP and 1M LiTFSI/P_{13}TFSI/PVDF-HFP polymer gel electrolytes. It is interesting to see that adding EC can remarkably increase the kinetics of Li ion transport. The

mobility of Li ions are highest in the membrane with 20%EC while they move slowest in the membrane without EC, clearly indicating that adding EC improves the Li ion transference number in the polymer gel electrolyte. The value of D_{Li} of the 1M LiTFSI/0.2EC+0.8P_{13}TFSI/PVDF-HFP polymer gel electrolyte is more than three times that of the polymer gel electrolyte without EC. Adding EC also increases the mobility of TFSI ions but has no significant effect on P_{13} ions.

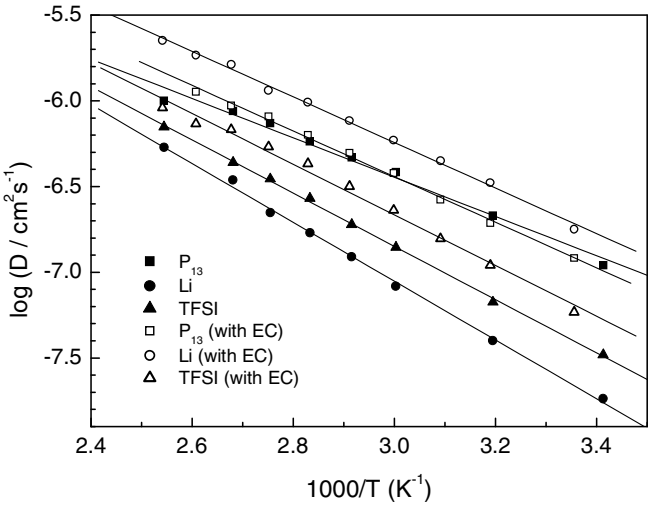

Fig. 7.8 Arrhenius plots of the self-diffusion coefficient of Li in the 1M LiTFSI/P_{13}TFSI/PVDF-HFP and 1M LiTFSI/0.2EC+0.8P_{13}TFSI/PVDF- HFP polymer gel electrolyte membranes

In order to gain additional dynamic information on the effect of EC incorporation, spin-lattice relaxation time (T_1) measurements, which are sensitive to rates of molecular/ionic motion occurring in the ~10^8 s^{-1} frequency range, were carried out by use of the inversion recovery method [149]. The uncertainties in the values obtained are 3-5 %. In the T_1 plot shown in Fig. 7.9,

we readily notice that the T_1's for the different ions in the polymer gel with EC are higher than the corresponding values in the gel without EC**.** The only exception to this are the ^{7}Li T_1's at low temperature, a point we will explore in detail later. The protons associated with the P_{13} ions do not exhibit a minimum in T_1 as this most likely occurs below the lowest temperature of the present set of measurements. Further reduction of motional correlation times at temperatures above the T_1 minimum give rise to increasing T_1 values. Thus the addition of EC increases the short-range motion of the P_{13} ion. However, the change in T_1 values upon adding EC is still relatively small. The reason for the leveling-off of P_{13} T_1 in the gel without EC is not understood. The ^{19}F from the TFSI ions also do not exhibit a clear T_1 minimum and, as in the case of P_{13} indicate enhanced motion (longer T_1) with the addition of EC. This effect is still relatively small, although somewhat larger than in the case of P_{13}. In both of these cases, it is likely that rotational mechanisms contribute to relaxation, and the addition of EC apparently enables freer rotation of methyl and trifluoromethyl groups, although the EC effect is a little less pronounced for P_{13} than for TFSI. Most importantly, from Fig. 7.9, we observe a minimum occurring for the Li ions at substantially lower temperature for the sample with EC than for the sample without it, providing a clear measure of enhanced motional correlation time upon addition of EC. This is in accord with conductivity and diffusion data (Fig. 7.6 and Fig. 7.8).

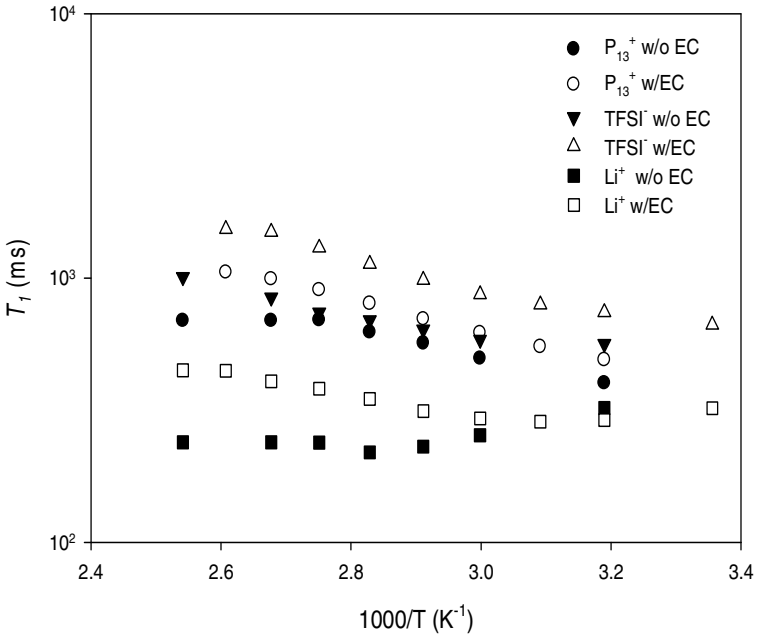

Fig. 7.9 Temperature dependence of NMR spin-lattice relaxation measurements of the different ions in 1M TFSI/P_{13}TFSI gels (with and without EC).

Linear sweep voltammetry (LSV) was performed on SS/PGE/Li cells to study the electrochemical stability of the membranes with varying content of EC as shown in Fig. 7.10. All the membranes possess good anodic electrochemical stability. The anodic stability limit (here the potential was set at a current density up to 10 μA/cm^2) of 1M LiTFSI/P_{13}TFSI/PVDF-HFP is as high as 5.75 V vs Li^+/Li. Adding EC decreases anodic stability slightly, but all are wide enough for Li/air batteries. In the fact, the membrane with highest EC content is still stable up to 5.1 V vs Li^+/Li, making this series of polymer gel electrolytes suitable for most high voltage Li intercalation cathode materials too.

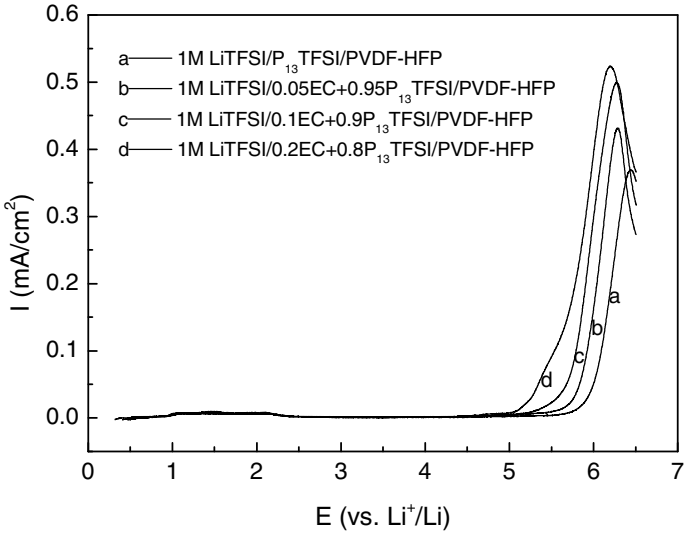

Fig. 7.10 Linear sweep voltammograms of 1 M LiTFSI / *x* EC+(1-*x*) P_{13}TFSI / PVDF-HFP (*x* = 0, 0.05, 0.1, and 0.2) membranes using SS/PE/Li cell; Scan rate is 1 mV/s.

Fig. 7.11 shows TGA results of the membranes containing the ionic liquids or Li salt/ionic liquid with different EC content. There is essentially no weight loss for the membranes with pure ionic liquid and Li salt/ionic liquid without EC when they are heated from room temperature to 200^{o}C, which clearly indicates that no component is volatile inside these membranes. Adding EC slightly decreases the thermal stability of the membranes above 100^{o}C. The weight loss above 100^{o}C is mainly due to the runaway of EC as supported by the TGA results of pure EC which is shown in the inserted plot in Fig. 7.11. The thermal stability of all investigated membranes is still good (weight loss less than 0.5 wt%) below 100^{o}C. The non-volatility or low-volatility of the polymer gel electrolyte is especially important for potential applications in open systems such as solid-state, thin film Li-air batteries.

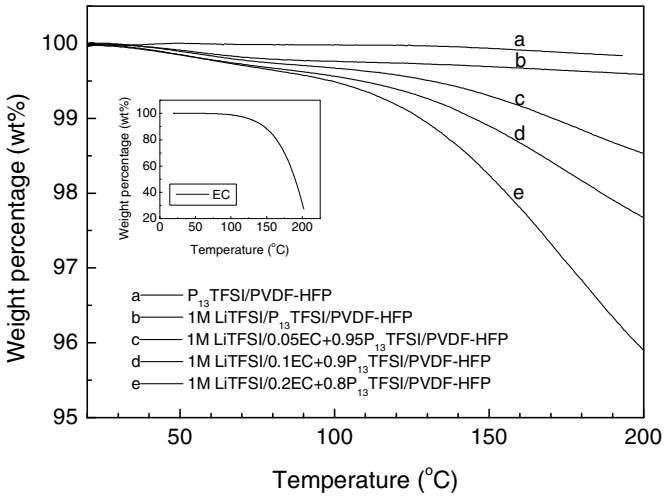

Fig. 7.11 TGA of P_{13}TFSI/PVDF-HFP and 1M LiTFSI / *x* EC+(1-*x*) P_{13}TFSI/PVDF-HFP (*x* = 0, 0.05, 0.1, and 0.2) membranes.

In order to understand the thermal properties as well as interactions among the various components of the polymer gel electrolyte membranes, DSC tests were performed on the polymer membranes containing pure ionic liquids and Li salt/ionic liquid with different EC content. Fig. 7.12 shows DSC curves of the investigated polymer gel electrolyte membranes, with data collected during the second heating step. All membranes show a wide endothermic peak above 100°C which may be ascribed to the melting of polymer. As a reference, the recast PVDF-HFP film has the melting peak at 139.5°C [141]. The melting peak for P_{13}TFSI/PVDF-HFP is 110 ^{o}C which may be due to the plasticization effects of ionic liquid. After adding 1M LiTFSI, the melting peak of the polymer membrane increases to 128 ^{o}C. Adding a small amount of EC will decrease the melting peak of the polymer membrane slightly, 126 ^{o}C, 124 ^{o}C, and 121 ^{o}C for the polymer membrane with 2.9 wt% EC, 5.8 wt% EC and 11.6 wt% EC, respectively. This can contribute to the plasticization effect of EC.

The EC is well dispersed inside the membranes as evidenced by the lack of an EC melting feature.

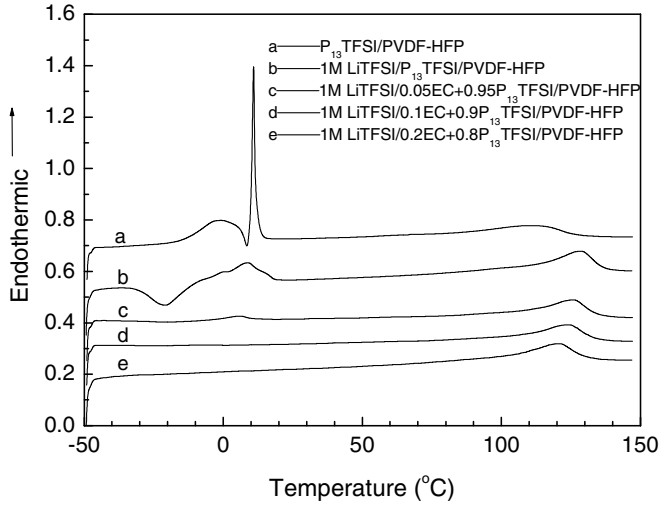

Fig. 12 DSC of P_{13}TFSI/PVDF-HFP and 1M LiTFSI / *x* EC+(1-*x*) P_{13}TFSI /PVDF-HFP (*x* = 0, 0.05, 0.1, and 0.2) membranes.

As shown in Fig. 7.12, there is a sharp endothermic peak at 11 ^{o}C following a wide endothermic peak around 1 ^{o}C for P_{13}TFSI/PVDF-HFP. The sharp endothermic peak can be ascribed to the melting peak of phase-separated P_{13}TFSI, which is close to the T_m of pure ionic liquid P_{13}TFSI (12 ^{o}C) reported by MacFarlane et al [17]. There is no recrystallization peak corresponding to this melting peak for pure ionic liquid shown in Fig. 7.11 probably due to the test temperature limitation. As reported, there is an exothermic peak around -67 ^{o}C for pure P_{13}TFSI [123]. The metastable phase transformation around -18 ^{o}C [123] for pure P_{13}TFSI does not show up in the investigated membrane either. The wide peak around 1 ^{o}C can be ascribed to the melting of polymer-solvated P_{13}TFSI because there are only two components in this polymer membrane and recast PVDF-HFP does not show

any thermal transform around this temperature [141]. There is only one wide endothermic peak for the membrane containing 1M LiTFSI/P_{13}TFSI at 9 ^{o}C coupled with a wide exothermic peak around -21^{o}C. This indicates that incorporating LiTFSI improves the solubility of P_{13}TFSI in the PVDF-HFP and makes the whole complex more homogeneous. Adding LiTFSI significantly suppresses the recrystallization process of P_{13}TFSI and decreases the melting of polymer-solvated P_{13}TFSI, reflecting the interaction among Li salt, ionic liquid and PVDF-HFP, as reported in the Zn salt/ionic liquid/PVDF-HFP system [141]. It is interesting to see that adding a small amount of EC can further suppress the recrystallization/melting of P_{13}TFSI. As shown in Fig. 7.11, 2.9 wt% EC decreases the melting of polymer-solvated P_{13}TFSI to 6 ^{o}C (the small endothermic peak) and totally suppresses the recrystallization process of the membrane. For the membrane with 5.9 wt% EC and 11.6 wt% EC, there is no distinct phase transformation from -45 ^{o}C to the melting point of polymer gel electrolyte. This feature of the polymer gel electrolyte with EC $\geq$ 5.8 wt% is particularly advantageous for potential applications of the batteries, such as military and aerospace applications as well as civil electric and hybrid vehicle applications.

The above DSC results indicate that the ionic liquids and Li salt/ionic liquid with or without EC most likely blend with the PVDF-HFP polymer at the molecular level and there must be strong interactions among the components, leading to the suppression of the individual thermal properties associated with the components. Further analysis of the interaction among different components in the polymer gel electrolyte by different spectroscopy methods is underway.

7.3.4 Preliminary Li/O_2 cells

Fig. 7.13 shows the charge/discharge curves of a preliminary Li/O_2 cell based on the 1M LiTFSI/ P_{13}TFSI /PVDF-HFP polymer gel electrolyte membrane. The capacity of the first discharge is about 900 mAh/g (carbon plus catalyst) and the voltage plateau is around 2.5 V. The capacity of the first charge is 625 mAh/g (carbon plus catalyst). These data are encouraging considering that the engineering aspects of the air electrode and the cell assembly has not been optimized. The fact that electrocatalytic oxygen reduction can take place with the ionic liquid as the electrolyte solvent is also scientifically interesting, suggesting possible applications of ionic liquids not only for metal/air batteries but also fuel cells. However, subsequent discharge/charge capacities are rather low. AC impedance tests were carried out after the cell setup and after each discharge. The interface resistance between the air electrode and polymer gel electrolyte membrane ($R_{O2/Elyte}$) and that between the Li foil and membrane ($R_{Li/Elyte}$) as determined by the tests are listed in Table 7.2. It was found that $R_{O2/Elyte}$ did not increase dramatically upon cycling, suggesting basic stability of the air electrode for repeated discharging/charging in the solid-state cell based on the polymer gel electrolyte membrane. However, $R_{Li/Elyte}$ increased dramatically upon cycling, preventing further discharge. A thick lithium oxide layer on the Li anode was observed after discharge/charge cycling. A similar thick lithium oxide layer was also observed when the Li/O_2 cell was kept in the open circuit state but the air electrode side was exposed to O_2 flow for one week. Oxygen crossover from the cathode to the anode to react with Li is likely the cause for the

dramatic increase of $R_{Li/Elyte}$. It appears necessary to suppress the oxygen crossover to achieve rechargeability and improve cycle life of the Li/O_2 cells.

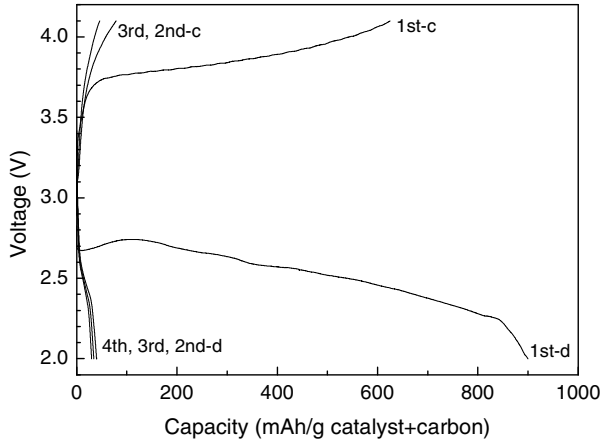

Fig. 7.13 Discharge/charge curves of a preliminary Li/O_2 cell based on the 1M LiTFSI / P_{13}TFSI /PVDF-HFP polymer gel electrolyte membrane; Current density is 0.05 mA/cm^2 air electrode.

	$R_{O2/Elyte}$	$R_{Li/Elyte}$
Initial setup state	-	180
After 1st discharge	69	1958
After 2nd discharge	80.6	2936
After 3rd discharge	125	2571
After 4th discharge	127	2560

Table 7.2 Interfacial resistances upon cycling of the Li/O_2 cell.

7.4 Conclusions

The ionic liquid 1-Methyl-3-Propylpyrrolidinium bis(trifluoromethanesulfonyl)imide (P_{13}TFSI) is a promising solvent for the

electrolyte of Li batteries because it possesses a wide electrochemical stability window and relatively low viscosity and is stable with respect to Li reduction reaction. Dimensionally stable, elastic, flexible, non-volatile polymer gel electrolyte with desirable properties can be readily synthesized by mixing LiTFSI/P_{13}TFSI solution with PVDF-HFP copolymer.

NMR indicates that the smallest Li ion shows the lowest self-diffusion coefficient among Li^+, P_{13}^+, and $TFSI^-$, which is possibly ascribed to high degree association of Li^+-*x*$TFSI^-$ ion. Ethylene carbonate (EC) has been demonstrated as a good Li ion transport enhancer in the LiTFSI/P_{13}TFSI/PVDF-HFP polymer gel electrolyte. Adding small amount of EC can improve ionic conductivity, net Li ion transport number, and Li ion transport kinetic dramatically. The EC with low volatility only slightly decreases the thermal and anodic stability of polymer gel electrolytes which are still stable enough for practical application. Polymer gel electrolytes LiTFSI/P_{13}TFSI/PVDF-HFP added small amount of EC are promising for the application of Li batteries including open system like Li/air cell, as well as conventional Li ion batteries. Preliminary discharge/charge results of Li/O_2 cell are encouraging for further improvement. Problem of oxygen crossover in the cell needs to be solved or alleviated for further progress.

Chapter 8: NMR investigation of water and methanol transport in sulfonated poly(areylenethioether) sulfones for fuel cell applications*

Abstract

We report an investigation of water and methanol transport in polymer electrolyte membranes based on highly sulfonated polyare-lenethioethersulfones (SPTES) for direct methanol fuel cell (DMFC) applications. Measurements of both water and methanol self-diffusion coefficients of SPTES polymer as well as in a reference sample of Nafion-117 equilibrated in 2 M methanol solution have been carried out, using the pulsed gradient spin echo technique, over a temperature range of 20–140°C. The selectivity of the membrane, defined as (D_{OH}/D_{CH3}), decreased from 6 to 2.4 as temperature increased from 20 to 140 °C in SPTES sample while in Nafion, the value decreased from 3.2 to 1.4 as temperature increased from 20 to 100°C. These results indicate significantly lower fuel molecular permeability in SPTES compared to that of Nafion. All results suggest high-temperature stability in these materials, offering the possibility of fuel cell operation at temperatures >120°C. High pressure NMR diffusion measurements were also carried out for three different water contents (between 20 and 55 wt.%) in a static field gradient in order to get supplemental information regarding water transport in SPTES materials. The calculated activation volume increased from

*This chapter constitutes the paper entitled "NMR investigation of water and methanol transport in sulfonated polyareylenethioethersulfones for fuel cell applications," by A. Khalfan, J.R.P. Jayakody, E.S. Mananga, S.G. Greenbaum, T.D. Dang and R. Mantz in *Journal of Power Sources* Volume 156, Issue 2, 1 June 2006, Pages 195-199.

1.54 to 8.40 cm^3/mol as the water content decreased from 55 to 20%. This behavior is qualitatively similar to previously reported results for Nafion-117.

8.1 Introduction

The development of high-performance polymer electrolyte membrane fuel cells (PEMFC) is critically dependent upon the transport properties of the polymer electrolyte membrane available [150]. At present, Nafion, which is a perflurosulfornated membrane with a hydrophobic fluorocarbon backbone and hydrophilic sulfonic pendent side chain, is the only commercially available and successfully used membrane in PEMFC applications [151]. However, since the performance of these membranes highly depends on their hydration levels, use of Nafion is limited to a temperature regime below 80°C [152], yet significantly higher temperatures (~120°C) are considered optimum for operation of the PEMFC [153].

Other disadvantages include the high cost of Nafion and its high permeability to methanol, which is used as a fuel in direct oxidation fuel cells (DOFC) [154] and [155].

Over the last decade, several new proton conducting polymer electrolyte membranes have been investigated [156], [157] and [158]. Among these are high-performance sulfonated polyarylenether and polyaryleneether sulfone polymers, which have been described in the literature due to their exceptional thermal stability, good mechanical properties, and proton conductivity [159], [160] and [161]. Advantages of DOFC include low cost, reduced weight and volume compared with indirect fuel cells in which the fuel is reformed into hydrogen before use. The most widely used fuel for DOFC is

methanol. Methanol is of low cost and has easy storage capabilities. Nonetheless, it has a low boiling point (~65°C) and permeates proton conduction membranes in fuel cells rather easily. This fuel permeability directly correlates with crossover, which refers to the transport of the intact fuel molecules to the cathode compartment, where the fuel molecules react with oxygen to produce water, carbon dioxide and heat. The result is the consumption of fuel without the production of electricity, thus, reducing the overall efficiency of the fuel cell. Methanol crossover is especially high in Nafion. Thus extensive effort has been made towards finding new low cost, solid polymer electrolytes with high ionic conductivity, high temperature operation capability (i.e. high temperature water retention), and low methanol permeability.

One potential solution is the synthesis of new high performance polymer electrolyte membrane materials using a wholly aromatic polymer backbone along with a high sulfonic acid content that enhances water retention and can consequently allow elevated temperature operation. Moreover, endcapping of these new highly sulfonated polymers takes advantage of a bulky aromatic end group to eliminate water solubility of these polymers without adversely affecting their proton conductivity. These materials offer the possibility of fuel cell operation at temperatures >120°C [161].

In this paper, highly sulfonated polyarylenethioethersulfone (SPTES) polymer membrane were investigated, with particular emphasis on water and methanol transport. Self-diffusion coefficients were measured using nuclear magnetic resonance pulse gradient spin-echo (NMR-PGSE) [162]. In cases

where the different nuclear (proton) environments can be resolved in the NMR spectrum, it is possible to measure distinct diffusion coefficients, for example those of water and methanol.

Greater understanding of the mechanism of ion and molecular transport in polymers can be greatly assisted by employing pressure as the thermodynamic variable. Previous NMR and electrical conductivity investigations have been carried out in PEM materials as a function of applied pressure [157], [158], [163] and [164]. Variable pressure measurements can probe molecular motion and ionic diffusion processes associated with volume fluctuations. It is of interesting to compare new results taken from SPTES samples in this investigation with previous work reported for Nafion [157], [158], [163] and [164].

8.2 Experimental details

Synthesis of the SPTES polymers has been described in detail elsewhere [161]. The SPTES membranes were cut into thin (~4 mm × 10 mm) rectangular strips, dried in a vacuum oven at 50 °C for 24 h and then saturated in 2 M methanol/deionized water for 2 days. Nafion-117 membranes were purchased from DuPont, boiled in 5% H_2O_2 solution and then 5% H_2SO_4 solution, rinsed on deionized wtrer, and then dried over P_2O_5. Total solution uptake was determined by using a microbalance and recorded as (weight of saturated film − weight of dry film)/weight of dry film) × 100%. For NMR measurements, samples were packed into 5 mm(o.d.) × 20 mm NMR tubes and flame-sealed under ambient atmosphere. The temperature

range investigated were 20–140 °C, with equilibration times of 20–25 min between each temperature change.

NMR measurements were performed on a Chemagnetics CMX-300 spectrometer with ^{1}H operating frequency of 301.02 MHz. Spectra were obtained by transforming the resulting free-induction decay (FID) of single $\pi/2$ (13 μs) pulse sequence. Self-diffusion coefficients (D) were obtained by the NMR–pulse gradient spin-echo technique (NMR–PGSE). This technique involves the use of the Hahn spin-echo pulse sequence ($\pi/2$–τ–π) and the simultaneous application of square-shaped magnetic gradients of magnitude g and duration δ. Diffusion results in attenuation of the echo amplitude A given by $A(g) = \exp[-\gamma^2 g^2 D\delta^2(\Delta - (\delta/3))]$ [165], where γ, D and Δ represents the nuclear gyromagnetic constant, self-diffusion coefficient, and interval between gradient pulses, respectively. Applied gradient strengths ranged from 0.2 to 2.2 T/m, δ and Δ ranged from 0.5 to 2.0 and 8–15 ms, respectively. The resulting echo profile versus gradient strengths is fitted to the above equation and D is extracted. Uncertainties in self-diffusion coefficient measurements are $\sim$5%.

For the high pressure NMR measurements samples were first dried in a vacuum oven at 50 °C for 24 h and then saturated in water for another 2 days. Water uptake (without methanol) was determined in the same manner as described above. Variation of the water uptake in samples was achieved by slowly drying the saturated sample in a dry N_2 atmosphere for a limited time until the desired water percentage was reached. Stack samples were made from five rectangular strips of film with dimensions 6 mm × 5 mm × 1.5 mm.

For NMR measurements, the samples were hermetically sealed in thin polyethylene bags, which were shown to produce a negligible proton NMR background signal compared to the signal from the sample. This was necessary in order to isolate the sample from the pressure transmitting fluid (hydrogen-free FLUORINERT electronic fluid, FC-77 manufactured by 3M Company).

The naturally existing field gradient of a conventional 7.3 T superconducting magnet was used for the measurements. The central field and gradient strength were varied continuously, within the limits of the magnet, by moving the NMR probe head within the bore of the magnet. The position of the NMR coil (which contains the sample) determines both the resonant frequency and the magnetic field gradient. A home-built computer controlled motorized stage, capable of moving the probe in precise steps of 0.25 mm, was used to center the coil at a field gradient strength ($G = dB_z/dz$) of 0.26 T/cm. This value was determined experimentally using the standard self-diffusion coefficient of water [166]. Accurate variation of the pressure (0–2.5 kbar) was carried out using an ENERPAC 11–400 hydraulic system fitted to a sealed Cu–Be alloy high-pressure chamber (bomb) inside of which resides the NMR radiofrequency coil and sample. Electronic connection between the coil (high pressure side) and external (ambient pressure side) matching and tuning capacitors was achieved by sealing the wire feedthroughs with an epoxy/ceramic composite. A homebuilt broadband NMR spectrometer operating at 69.35 MHz (the central field value corresponding to the position of the sample in the fringe-field) and utilizing a phase cycled spin-echo pulse sequence ($\pi/2$–τ–π–τ, *acquire*) was used to detect the proton echo signal from

the sample. Pulse widths ($\pi/2$) were typically of 2.5 μs duration. This value was chosen on the basis of the maximum signal amplitude obtainable for a given pulse separation.

8.3 Results

A typical proton spectrum of an SPTES sample equilibrated in 2 M methanol is shown in Fig. 1. The sample chosen is denoted SP50 which is an endcapped 50/50 blend of sulfonated polyarylenethioethersulfone sulfite/polyarylenethioethersulfone sulfite. The two distinct proton environments namely that of water (OH) and (CH_3) are clearly resolved, even in the membrane, allowing one to determine the equilibrium methanol concentration in the film and to measure self-diffusion coefficients separately for each component. Self-diffusion measurements were made as a function of temperature for SPTES and Nafion-117 samples, both equilibrated in 2 M MeOH aqueous solutions. Diffusive decay of the main peak (OH) of the spectrum represents the water self-diffusion because the water OH groups far outnumber the methanol OH groups for the present MeOH concentration.

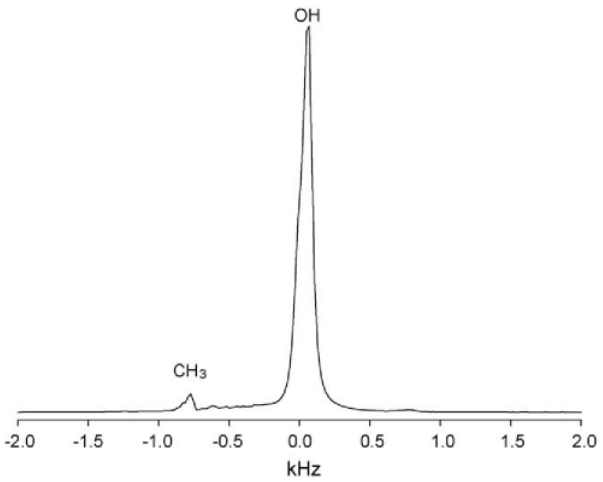

Fig. 8.1 ^{1}H NMR spectrum of SPTES equilibrated in 2 M MeOH at 313 K.

The ratio of the integrated intensities of the CH_3 to OH proton NMR peaks is approximately proportional to the methanol concentration in the membrane (at low methanol concentration), and thus can provide a direct measure of selective methanol uptake (i.e. partitioning), if the equilibrium concentration in the membrane is not equal to that of the solution. The CH_3/OH percentage NMR intensity ratio is plotted in Fig. 8.2. The integrated CH_3/OH intensity ratio in a 2 M solution was determined to be about 6%, in agreement with the calculated value. This is close to the values measured for Nafion below about 80 °C. From these results it is clear that the SPTES membrane takes up considerably less methanol from the 2 M starting solution than Nafion, especially at low temperature.

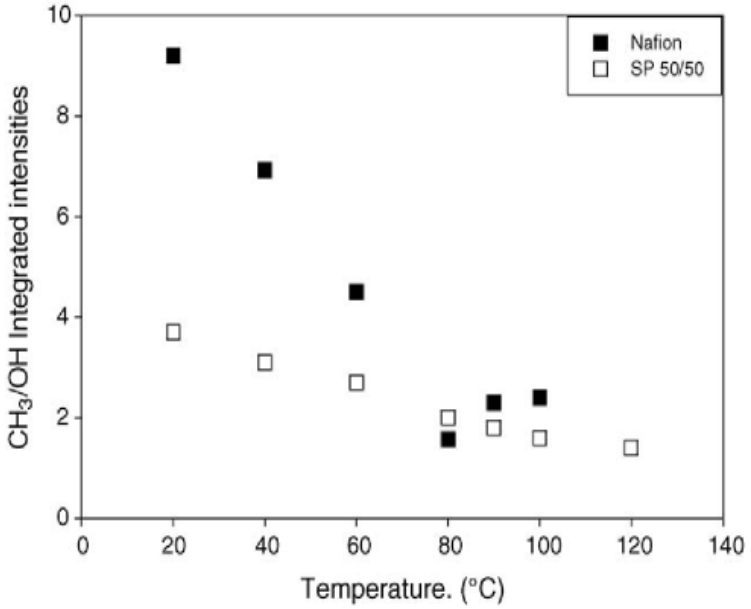

Fig. 8.2 Integrated proton NMR intensity as percentage of methanol to water peaks in SPTES and Nafion membranes equilibrated in 2 M MeOH.

The direct comparison of self-diffusion coefficients as a function of temperature between SPTES and Nafion is shown in Fig. 8.3. The water diffusion coefficients in both membranes are quite comparable up to 80°C, as are previously reported conductivity measurements [161]. However above 80°C, the water diffusion coefficient in Nafion is reduced whereas it is increased in SPTES all the way up to the highest measurement temperature, 140°C. This result provides indirect but nevertheless compelling evidence that water is well retained in SPTES at temperatures up to 140°C. The drop in water diffusion in Nafion above 80°C has been previously attributed to membrane dehydration [151].

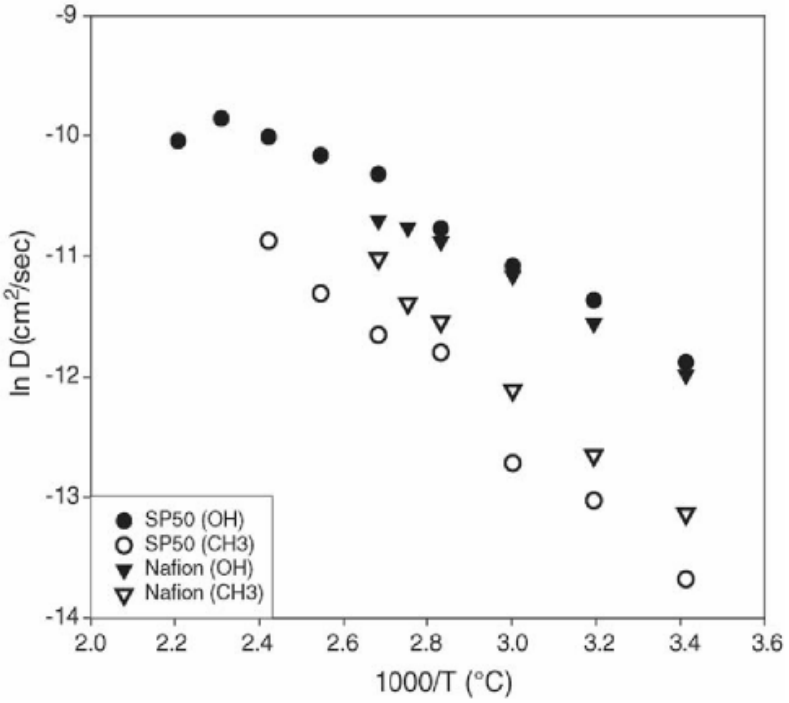

Fig. 8.3 ^{1}H self-diffusion coefficients of 2 M MeOH saturated SPTES and Nafion membranes.

Results of the diffusion coefficient of CH_3 in both samples are also included in Fig. 8.3. Methanol diffusion is clearly lower in SPTES than in Nafion, but in order to obtain more meaningful results with respect to operation in a DMFC, we define the membrane selectivity as the ratio $D(OH)/D(CH_3)$. The rationale for this definition is that $D(OH)$ is correlated with proton conductivity and $D(CH_3)$ is correlated with methanol permeability and hence crossover. It is thus desirable to have a proton conduction membrane with high selectivity. Variable temperature selectivity results for the two membranes are plotted in Fig. 8.4. The selectivity ratio of SPTES is about a factor of two higher than that of Nafion, although both membranes exhibit a decrease in selectivity with increasing temperature.

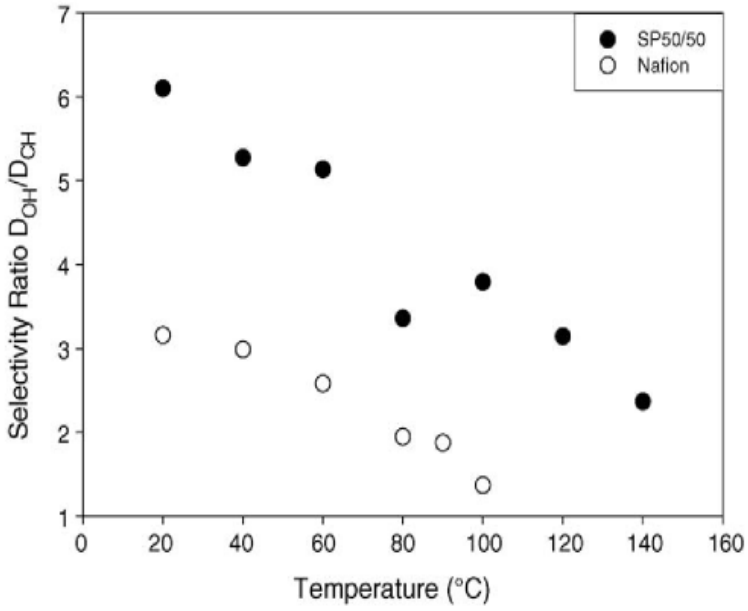

Fig. 8.4 ^{1}H selectivity ratio of 2 M MeOH saturated SPTE and Nafion membranes.

For high-pressure NMR measurements we used SPTES60 (SPTES 60/40) and SPTES50 (the latter being the same material discussed above) membranes for three different water contents. Because of the large magnetic field inhomogeneity, characteristic of the high pressure diffusion apparatus, it is impossible to resolve water and methanol peaks. Therefore, membranes equilibrated in only water were investigated. Proton spin echo intensities $M(\tau)$ were measured as a function of the pulse separation, τ, and self-diffusion coefficients D were extracted from the data using Eq. (8.1) [162].

$$M(\tau) = M_0 \exp\left\{\frac{-2}{3}\left[\frac{3\tau}{T_2} + \gamma^2 g^2 D\tau^3\right]\right\} \qquad (8.1)$$

In this expression, M_0 is the maximum magnetization (extrapolated to $\tau = 0$). To assist in the analysis, proton transverse relaxation times T_2 were measured independently and the data were fit to a linearized version of Eq. (1) with slope, $2(\gamma G)^2 D/3$ and intercept, $2/T_2$. In this way, the diffusion coefficients were gathered with respect to applied pressure. The self-diffusion coefficients were extracted from the above graphs as a function of pressure for four different water contents in SPTES 60 are plotted in Fig. 8.5.

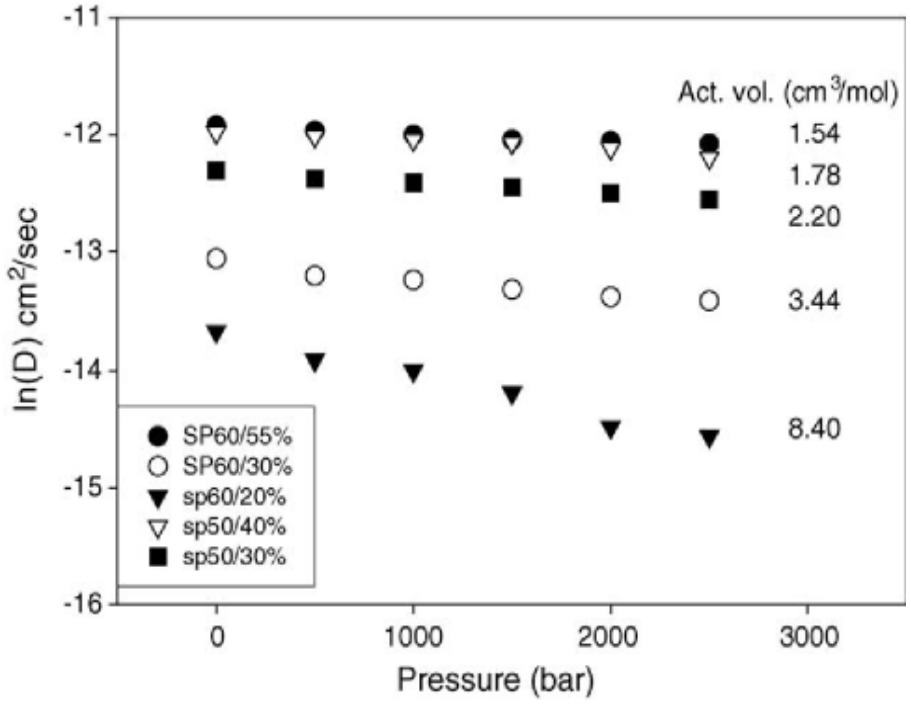

Fig. 8.5 ^{1}H diffusion coefficients of SPTES50 and SPTES60 membranes as a function of pressure for different water concentrations.

The data in Fig. 8.5 can be further analyzed to yield the activation volume Δv associated with the diffusing water molecules according to Eq. (8.2).

$$\Delta v = -kT\left(\frac{\partial \ln D}{\partial P}\right)_T \tag{8.2}$$

The activation volumes for four different water contents in SPTES 60 are listed on the same plot. The self-diffusion coefficient generally decreases with decreasing water content and also with increasing pressure as this reflects greater restrictions for water molecular motions. In addition, the membranes with higher water content have smaller Δv than those with lower water content. A relatively large Δv of 8.4 cm^3/mol is observed for 30% water content in SPTES60 membrane. Similar behavior has been observed from diffusion and electrical conductivity measurements of hydrated Nafion-117 films with lower water content [157], [158], [163], [164] and [167]. The observation that high activation volumes are often associated with solvent-free polymer electrolytes suggests that ion transport in these cases is controlled by polymeric segmental motion [157] and [166]. The highest activation volume we have seen here is lower than the values usually associated exclusively with segmental motion. It is surmised that significantly higher values of Δv would be observed for nearly dry membranes (<10% water), but the proton NMR signal strength is insufficient to verify this. At high water contents, Δv is relatively small in both membranes and does not vary much with increasing water content. In a previous paper [163], it was suggested that the diffusion in

this region is controlled by bulk water more than by the polymer. Zawodzinski et al. has also pointed out that the conductivity mechanism at high water content is expected to approach that of bulk water due to the large number of pores within the polymer that are filled with water [151].

8.4 Conclusions

Water and methanol mobility in Nafion and SPTES membranes equilibrated in 2 M MeOH were studied by PGSE–NMR diffusion techniques. The new membranes exhibit significantly higher water diffusion than Nafion, especially for temperatures above 80°C. Diffusivity remains high even beyond 140°C, providing evidence of water being well-retained at higher temperatures. We have also defined a selectivity criterion $D(\mathrm{OH})/D(\mathrm{CH_3})$ and SPTES exhibits a higher one than Nafion.

High-pressure NMR measurements of the water self-diffusion coefficient in SPTES60 and SPTES50 were conducted in the non-uniform region (fringe) of a superconducting magnet. Activation volumes associated with water mobility have been obtained at several different water contents. The largest activation volume (8.4 cm^3/mol) is found at the lower water content (20%) of SPTES60 membrane. As the water content increases, Δv decreases rapidly and only gradually thereafter. This indicates that the transport mechanism in low-water content films is controlled to an extent by segmental motions of the polymer. At higher water content, the Δv values are comparatively small, suggesting that the transport mechanism in high-water content membranes is dominated by bulk water. These results, which are in good agreement with the previous studies of spin-lattice relaxation, diffusion

and electrical conductivity of Nafion, illustrate how the pressure dependence of self-diffusion coefficients can be a useful tool in characterizing molecular motion for new fuel cell membranes.

Acknowledgments

This work was supported by the US Air Force Office of Scientific Research, and Wright Patterson Air Force Base, and an RCMI Infrastructure grant from the National Institutes of Health.

Chapter 9: Fluorinated Poly (arylenethioethersulfone) Polymers with Sulfonic Acid Pendants for Applications to Proton Exchange Membrane Fuel Cells*

Abstract

In the present study, we examine the water and proton transport properties of hexafluorinated sulfonated poly (arylenethioethersulfone) (6F-SPTES) copolymer membranes for applications to proton exchange membrane fuel cells (PEMFCs). The 6F-SPTES copolymer membranes build upon the structures of previously studied sulfonated poly (arylenethioethersulfone) (SPTES) copolymer membranes to include CF_3 functional groups in efforts to strengthen water retention and extend membrane performance at elevated temperatures (above 120^{o}C). The 6F-SPTES copolymer membranes sustain higher water self-diffusion and greater proton conductivities than the commercial Nafion® membrane. Water diffusion studies of the 6F-SPTES copolymer membranes using the pulsed field gradient spin-echo NMR technique reveal, however, the fluorinated membranes to be somewhat unfavorable over their non-fluorinated counterparts as high temperature membranes. In addition, proton conductivity measurements of the fluorinated membranes up to 85^{o}C show comparable results with the non-fluorinated SPTES membranes.

*This chapter includes work that is in the process of being published in the Journal of Power Sources with the following as authors: A. Khalfan, S.G. Greenbaum, L.M. Sanchez, C. Kodiweera, Z. Bai, T.D. Dang.

9.1 Introduction

Fuel cells offer an alternative means of providing electrical energy to power homes and cars as well as portable devices such as notebook computers. Proton exchange membrane fuel cells (PEMFCs) operate at relatively low temperature and use reformed hydrogen or methanol as a fuel. This leads to, among other problems, CO poisoning of the anode catalyst [168].

High temperature (120 – 140^{o}C) fuel cell operation offers several advantages in addition to CO tolerance, including faster proton transport kinetics, better water management and heat rejection. Although Nafion exhibits high proton conductivity (e.g. around 80 mS/cm at room temperature and 100% R.H), above 80^{o}C the conductivity drops due to water being driven out of the membrane [169]. Studies have shown that the proton transport mechanism in sulfonated polymer membranes is strongly correlated with water mobility [170]. Water retention is therefore an issue of main concern in synthesizing viable PEMs. At higher temperatures, degradation of the membrane may also occur due to condensing water vapor that acts to swell and shrink the membrane repeatedly [171]. Furthermore, at an operating temperature above the glass transition temperature of Nafion (between 100^{o}C-110^{o}C), structural changes can arise and thus lower membrane stability and lifetime [172]. A great deal of research in PEM's today is concerned with searching for a membrane material, other than Nafion, which can withstand high temperature operation, and at the same time provide high proton conductivity.

Highly sulfonated polyarylenetheriosulfone (SPTES) copolymers with endcapping have been synthesized by the Air Force Research Lab as possible alternatives to Nafion. The SPTES copolymer incorporates highly sulfonated regions attached to an aromatic hydrocarbon polymer backbone as depicted in Fig. 9.1. The use of hydrocarbon groups is believed to offer greater structural and thermal stability than the fluorocarbons of Nafion**.** The SPTES copolymers are also cheaper to synthesize than Nafion. The high degree of sulfonation in these membranes serves to enhance water uptake and thereby increase proton conduction. Endcapping of the copolymers was carried out to minimize excessive swelling or even the potential for water solubility. Also, the aromatic polymers are characteristically high in molecular weight to ensure polymer chain entanglements that can produce durable membrane films when inserted into the fuel cell assembly [173].

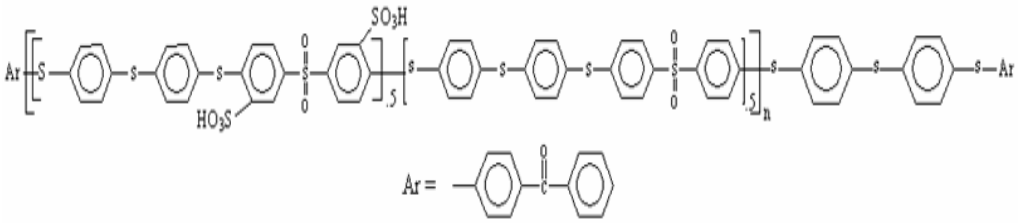

Fig. 9.1– Endcapped SPTES copolymer structure.

In a previous study, SPTES-50 (‘50’ referring to percentage of sulfonated polymer in a blend of sulfonated and unsulfonated polymer) copolymer saturated in 2M methanol solution (in consideration of possible direct methanol fuel cell applications) was shown to retain water well as water diffusivity of the membrane remained high at higher temperatures (up to 160^{o}C) [174].

The proton and water transport properties of hexafluorinated SPTES copolymers, labeled 6F-SPTES-50 and 6F-SPTES-70, (structures shown in Fig. 9.2) are the subjects of this investigation. Modeled after the morphology of Nafion, the replacement of the central thioether group in the original SPTES copolymer structure by the addition of two hydrophobic CF_3 functional groups per repeat polymer unit had been hypothesized to enhance proton transfer by facilitating the formation of ionic clusters, which link together and provide a channel for transport [170]. Another reason for the inclusion of the CF_3 groups was to balance the hydrophilicity and hydrophobicity of the polymer backbone in an attempt to preserve the membrane structure as water is absorbed. Samples of 6F-SPTES-50 and 6F-SPTES-70 copolymers were studied as a function of only water (not methanol) content. The structural and dynamical measurements performed in this work include molecular weight measurements via gel permeation chromatography, ^{1}H NMR spin-relaxation and diffusion measurements, and proton conductivity measurements by means of AC Impedance Spectroscopy.

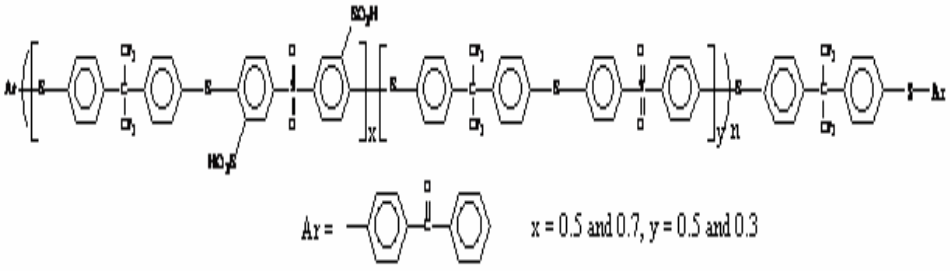

Fig. 9.2 - The chemical structure of hexafluorinated sulfonated poly (arylenethioethersulfone) endcapped copolymers.

9.2 Experimental

9.2.1 Materials

4-Fluorophenylsulfone (99%, Sigma-Aldrich Co.), Potassium carbonate (99%, ACS reagent, Sigma-Aldrich Co.), Tetramethylene sulfone (Sulfolane, 99%, Sigma-Aldrich Co.), 4-Chlorophenylsulfone (98%, Sigma-Aldrich Co.), 4-Fluorobenzophenone (97%, Sigma-Aldrich Co.), 4-Chlorobenzophenone (99%, Sigma-Aldrich Co.), Sulfuric acid (Fuming, 30% SO_3, Sigma-Aldrich Co.), 2-Propanol (Fisher Scientific), N, N-dimethylacetamide (DMAc, Anhydride, 99%, Sigma-Aldrich Co.), were used as received. Other chemicals were of commercially available grade and used as received unless otherwise mentioned. 4, 4-(hexafluoroisopropylidene)-diphenol (6F-BPA) was obtained from TCI America, 4, 4'-[2, 2, 2-trifluoro-1-(trifluoromethyl) ethylidene] bisbenzenethiol (Hexafluorobisphenylthiol A) was prepared in AFRL/MLBP Lab. Sulfonated monomer, 3, 3'-disulfonate-4, 4'-difluorodiphenylsulfone, was prepared following the procedures in the literature [173], [175].

9.2.2 Synthesis and fabrication of 6F-SPTES copolymer with endcapping group

The 6F-SPTES-50 copolymer was prepared by the following procedure. 3, 3'-Disulfonate-4, 4'-difluorodiphenylsulfone (1.8333g, 4.0mmol), 4-fluorophenylsulfone, (1.0068g, 3.96mmol), hexafluorobisphenylthiol A (2.9468g, 8.0mmol), and potassium carbonate (2.8748g, 20.8mmol) were charged into a 100 ml round-bottom flask

maintained under a back pressure of nitrogen and equipped with a magnetic stirrer and an oil bath on a hot plate. 50 ml of sulfolane was added into the flask, stirred for 45 min at room temperature and at 100°C for an overnight. This was followed by the addition of 4-fluorobenzophenone (0.008g, 0.04mmol) as an endcapping agent into the reaction solution. The reaction mixture was heated to 160-180^{o}C for 6 hours, then cooled down to room temperature, quenched with acetic acid, and precipitated in methanol/acetone. The polymer was filtrated and air-dried, then, soxhlet-extracted with methanol for 48 hours, and dried in vacuum at 80^{o}C overnight to afford a yield of 89%.

The fluorinated sulfonated poly (arylenethioethersulfone) copolymers (salt form) with the endcapping group were dissolved in the DMAc at 100°C to a clear solution, and filtered at room temperature. The membranes were directly cast in a flat dish at 80°C in vacuum for 24 hours. The clear films were converted to the corresponding sulfonic acids in the presence of dilute sulfuric acid (4M) at room temperature for 48 hours. The films were dried at room temperature, then at 100°C in vacuum for 24 hours. Tough, clear and flexible films of the 6F-SPTES copolymers were fabricated.

9.2.3 Instrumentation

Gel permeation chromatography (GPC) was used to determine molecular weights and molecular weight distributions, $\mathbf{M_w}$ and $\mathbf{M_n}$ respectively, of synthesized polymer samples with respect to polystyrene standards. MW measurement was performed on TriSEC Version 3.00 at 70°C in NMP containing 0.5% (wt) LiBr. Intrinsic viscosity (IV) was measured at 30°C in NMP, which contained 0.5% (wt) LiBr, by using an Ubbelohde

Viscometer. Thermogravimetry (TGA) was conducted using an Auto TGA 2950HR V5.4A instrument in air at a heating rate of 10°C/min.

The conductivity of 6F-SPTES copolymer membranes was measured using AC Impedance Spectroscopy and utilized a standard 4-electrode measurement setup to eliminate electrode and interfacial effects. The proton conductivity was calculated using $\sigma = l/Rdw$, where l is the distance between the electrodes, d and w are the thickness and width of the films, respectively, and R was derived from the low intersect of the high frequency semi-circle on a complex impedance plane with the abscissa axis.

A CMX-300 MHz spectrometer in conjunction with a JMT superconducting magnet of field strength B_0 = 7.1T was used to characterize structural and dynamical properties of hydrated 6F-SPTES-50 copolymer. The same spectrometer but in operation with a different magnet (for availability purposes), of field strength B_0 = 7.2T, was used to investigate hydrated 6F-SPTES-70 copolymer.

The spin-lattice relaxation times (T_1's) of the water protons as well as structural polymer protons were measured as a function of temperature by implementing the inversion recovery pulse sequence ($\pi - \tau - \frac{\pi}{2}$). T_1 gives crucial information regarding the local environment of a nuclear species on the timescale of 10^{-10} to 10^{-8} s [176]. Quoted values of T_1 are subject to ±3% uncertainty.

The self-diffusion coefficient, D, is useful in measuring long-range ion and molecular transport. Temperature dependent D values of water in the 6F-SPTES copolymers were measured using the pulsed gradient spin echo (PGSE) method. The method consists of enacting the Hahn spin-echo pulse

sequence ($\pi/2 - \tau - \pi$) with the inclusion of two square-shaped gradient pulses [177]. Equation (9.1) was used to make a Gaussian fit of the echo amplitude and determine the self-diffusion coefficient *D*.

$$A(g) = \exp[-\gamma^2 D g^2 \delta^2 (\Delta - \delta/3)] \tag{9.1}$$

where *A* is the echo amplitude as a function of the gradient strength *g*, γ is the gyromagnetic ratio, δ is duration of each gradient pulse, and Δ is the time delay between gradients. For the diffusion experiments conducted on the 6F-SPTES-50 membranes, a Doty broadband diffusion probe was used with applied gradient values reaching 200 G/cm while δ and Δ values ranged from 0.8 - 2.5 ms and 10 - 13 ms, respectively. A Nalorac Z-Spec diffusion probe was used in performing *D* measurements on the 6F-SPTES-70 membranes with gradient strengths of up to 60 G/cm**.** δ and Δ values, using the Nalorac Probe, ranged from 3 - 4 ms and 8 - 10 ms, respectively**.** The uncertainty in measuring *D* is ±3 - 6% for either probe**.** For both T_1 and *D* measurements conducted at variable temperature, at least 20 minutes was allowed for equilibration after setting the temperature.

9.2.4 Water Uptake Measurements

Preceding ^{1}H NMR experimentation, the 6F-SPTES-50 copolymer was prepared with three different water contents. The water content in terms of percentage uptake by weight for the 6F-SPTES- 50 samples were 11.5%, 18.3%, and 29.9%. The method of preparation involved first placing small, rectangular strips of the polymer material over P_2O_5 in a desiccator at room

temperature. After allowing the strips to dry for 3-5 days, they were inserted into beakers placed over a reservoir of distilled water in a sealed larger vessel. The strips were left in the vessel to absorb water vapor for about 1-3 days. This procedure of hydration was, however, not undertaken for sample 6F-SPTES-50/29.9% wt., which stayed immersed in water for 1-3 days so as to reach a fully hydrated level. The other set of membranes, 6F-SPTES-70, were prepared with water contents of 17.4, 46.4, and 76.5 wt%.

The wet membrane strips (swollen to some degree) were padded dry on the surface before being densely packed into 5 mm o.d. pyrex® tubes that were subsequently flame-sealed. Packing of the membrane material was done rather quickly to ensure minimal possible changes in the desired hydration level. Additionally, a teflon® plug was placed just above the sample to keep water from reaching the top portion of the tube since the loss of water remained a possibility in the high temperature experiments that were to follow. Similar methods of preparation were used for the 6F-SPTES-70 coploymer membranes, which tended to take up more water due to the presence of the higher content of sulfonic acid.

The following formula was used to compute water uptake in wt. %:

$$\text{Water uptake} = \frac{m_{wet} - m_{dry}}{m_{dry}} \times 100 \qquad (9.2)$$

where m_{wet} and m_{dry} are the masses of the wet and dry membranes, respectively. An error of ± 0.004 g was determined to be present in using the microbalance. The measured water uptake of 6F-SPTES was found to be somewhat higher than that of SPTES at a comparable level of sulfonation, compared to the non-fluorinated SPTES. This is expected of the polymer

system in which the central thioether group was replaced by hexafluoroisopropylidene groups (6F), with the intent of enhancing backbone hydrophobicity. Our qualitative explanation for this observation is somewhat based on the 'cluster network model' description in the literature [178], [179] of the microscopic structure of Nafion membrane in which the ion-exchange sites are separated from the perfluorocarbon backbone resulting in the formation of pores which are connected by short narrow channels. In the case of 6F-SPTES, the higher water uptake relative to SPTES is presumably due to the fact that the enhanced hydrophobicity of the backbone containing hexafluoroisopropylidene groups can cause more effective sequestration of the sulfonic acid-containing hydrophilic domains in the polymer microstructure. As will be discussed later, however, the high initial water uptake does not necessarily imply that this water is well retained at elevated temperature.

9.3 Results and Discussion

9.3.1 ^{1}H NMR Spectra of Fluorinated SPTES Copolymers

^{1}H NMR room temperature spectra, obtained after Fourier transformation of the free induction decay following a single $\frac{\pi}{2}$ pulse sequence, for the three different water contents of 6F-SPTES-50 copolymer are displayed in Fig. 9.3. Distilled water was used as the zero reference with a ^{1}H resonance frequency of 301.020 MHz. The relative intensities of the peaks for each sample are shown in Fig. 9.3. All spectra reveal a strong absorption peak shifted downfield, falling somewhere in the range of 330 – 410 Hz (~ 1

to 1.3 ppm) relative to the reference. The peak can be mainly attributed to water in the membrane since the largest concentration of protons can be found there. As for the observed shift, a plausible explanation is the effect of deshielding from the external field that the OH protons in water experience from the SO_3^- groups. The acid proton dissociated from the SO_3^- cannot be detected by itself as the total proton NMR signal is completely dominated by water protons.

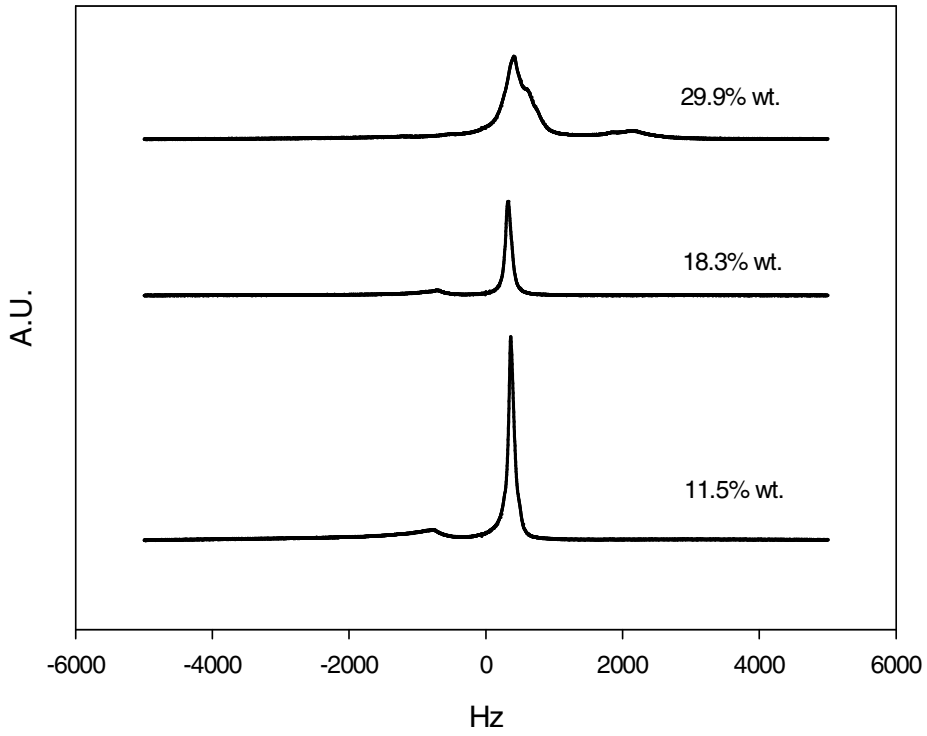

Fig. 9.3– ^{1}H room temperature spectra of 6F-SPTES-50 copolymer membranes.

In samples 6F-SPTES-50/11.5% wt. and 6F-SPTES-50/18.3% wt., we clearly see a smaller and somewhat broad peak, which is upshifted about 2.4

ppm from the reference. The spectrum for sample 6F-SPTES-50/29.9% wt. also seems to show such a peak, but it is nearly buried under a much larger water signal. The water resonance signal for 6F-SPTES-50/29.9% wt. is, as expected, noticeably stronger (greater area under the spectral curve) than for the two 6F-SPTES-50 samples of lower water uptake, but it's also considerably broader. We may assign this secondary peak to the aromatic protons making up the backbone of the 6F-SPTES-50 membrane. In support of this claim, diffusion data reveals no observable attenuation of these secondary peaks with increasing gradient strength, i.e. these protons don't diffuse. The shift between water and aromatic ring protons is generally around 3 ppm, which also supports this assignment [180], [181]. Lastly, the spectrum of 6F-SPTES-50/29.9% wt. features a broad component shifted downfield (~ 6.7 ppm) and arises due to anisotropy of water in the membrane, i.e. the water is spread out in different parts of the sample. In fact, variable temperature T_1 data for this peak was separately found to resemble T_1 values measured for the main water peak and thus support this peak assignment. It may also be of interest to note that the linewidths of the main peaks shown in Fig. 9.4 span from approximately 100 to 150 Hz for the lower water contents while for 6F-50/29.9% wt., a linewidth of ~ 410 Hz is found. The linewidths did not change widely with temperature apart for maybe sample 6F- SPTES-50/18% wt., which exhibited a linewidth of 107 Hz at room temperature and one of 63 Hz at ~ 80^{o}C.

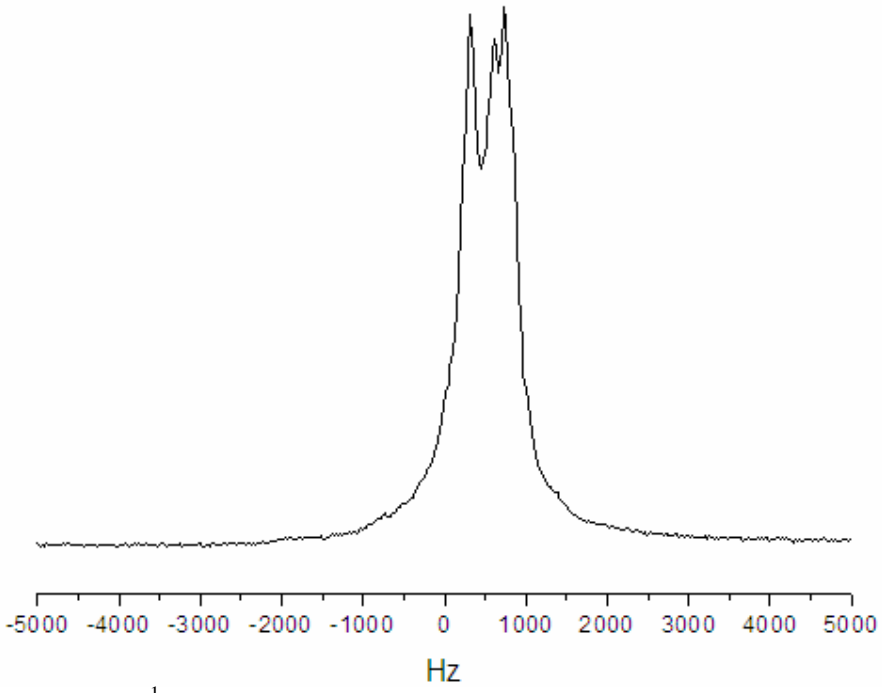

Fig. 9.4– ^{1}H room temperature spectrum of 6F-SPTES-70/45% wt. membrane.

With regard to ^{1}H NMR measurements carried out for hydrated 6F-SPTES-70 membranes, the experimental configuration included a different magnet with greater field inhomogeneity. Thus the spectra arising from this set of samples tended to give somewhat broader peaks. A representative spectrum is shown in Fig. 9.4, which was referenced to distilled water but with a carrier frequency of 307.031 MHz. In this room temperature spectrum for 6F-SPTES-70/45% wt., we observe a water signal at about 1 ppm upfield and another closely spaced doublet at about 2.4 ppm, similar to the shifts in Fig. 9.3. Diffusion data reported for this sample were derived from decay of the 1 ppm peak. The hydrocarbon site cannot be distinguished because of the line broadening feature. The linewidths of the water peaks observed were several hundred Hz.

9.3.2 ^{1}H Spin-Lattice Relaxation Measurements of Fluorinated SPTES Copolymers

Figure 9.5 displays Arrhenius plots of T_1 values of the water protons in hydrated 6F-SPTES-50 and 6F-SPTES-70 membranes. Focusing on the 6F-SPTES-50 membranes first, T_1 clearly increases with temperature throughout the temperature range investigated. The rising T_1 behavior suggests that the rates of tumbling and vibrational motions of the water molecules exceed the NMR (Larmor) angular frequency, characteristic of molecular motion in the high temperature regime [182]. Relatively short motional correlation times can therefore be ascribed to the water molecules. The 6F-SPTES-50 sample with the lowest water content exhibits a broad T_1 minimum around room temperature. Presumably, T_1 minima would be observed for the other samples at lower temperatures. As for 6F-SPTES-70 samples, we also observe an increasing trend in T_1 with temperature, however, the relaxation values drop above 70^{o}C for samples 6F-SPTES-70/17.4% wt. and 6F-SPTES-70/46.4% wt., and above 90-95^{o}C for 6F-SPTES-70/76.5% wt. The fall off in T_1 is associated with the loss of water in the membrane as higher temperatures are reached. This observation will be discussed later in the context of the water diffusion results. Sample 6F-SPTES-70/75% wt. features the highest T_1 values, implying relatively fast molecular motion. This is not unexpected as the water molecules in the higher water content membranes begin to experience an environment approaching that of liquid water. T_1 measurements for water in the 6F-SPTES-70 membranes tended to be greater than that for the 6F-SPTES-50 membranes suggesting faster water mobility in 6F-SPTES-70 membranes, which is supported by higher water diffusion values measured

for the 6F-SPTES-70 membranes discussed next. According to this reasoning, it would appear that the lower T_1 values of the 6F- SPTES-50 membrane with the highest water content are anomalous. However this may be related to the significantly broader linewidth of this sample (Fig. 9.3), which suggests stronger local interactions between water molecules and their environment, leading to enhanced relaxation.

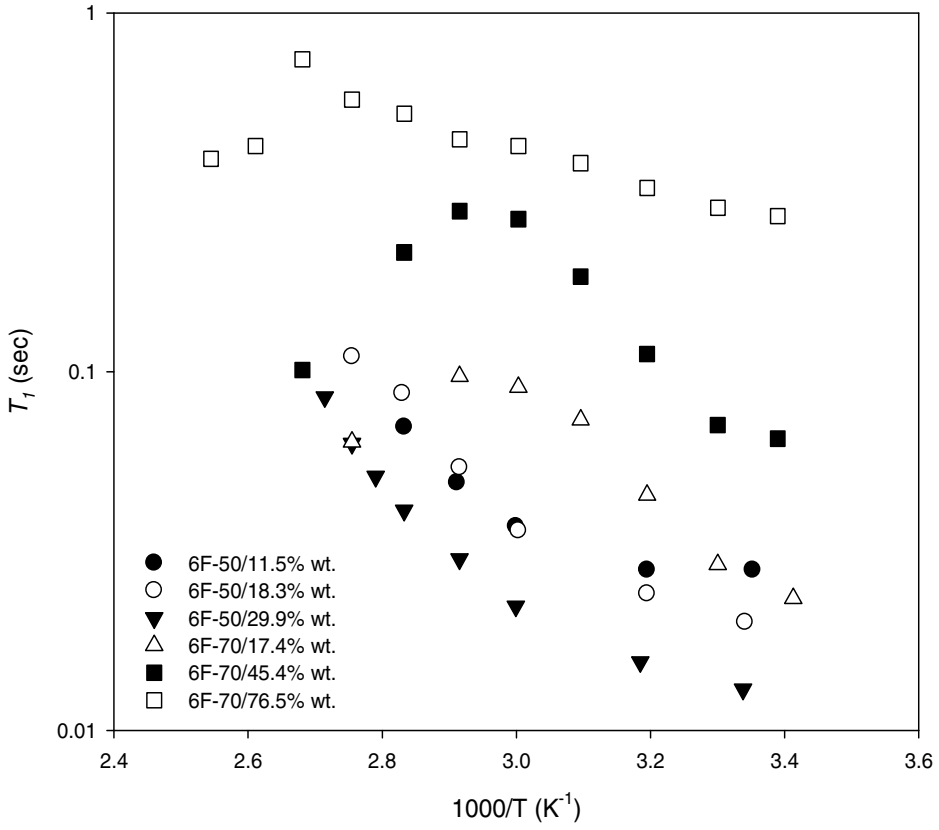

Fig. 9.5 – Semilog Plot of ^{1}H Spin-Relaxation Times of Water Molecules in 6F-SPTES Copolymer Membranes.

9.3.3 Water Self-diffusion Measurements and Proton Conductivity Data of 6F-SPTES Copolymers

Shown in Fig. 9.6 are the Arrhenius diffusion curves for the hydrated 6F-SPTES-50 and 6F-SPTES-70 membranes. We readily observe a common trend through each sample tested, namely, that the water diffusivity rises with temperature yet undergoes a gradual drop as the sample is heated to a temperature lying in the range of 70^{o}C-110^{o}C. The membrane sample begins to dehydrate in the specified range of temperatures. We recall that Nafion experiences water loss at a comparable temperature, approximately 80^{o}C, and special measures must be taken to keep the membrane hydrated when operating in the fuel cell assembly at or above this temperature. It is thus believed that the 6F-SPTES copolymer membranes therefore do not offer a significant advantage over Nafion in terms of membrane performance at elevated temperature, as water is seen not to be retained well in the 6F-SPTES copolymer membranes for temperatures even below the boiling point of water. An exception may be made for sample 6F-SPTES-70/76.5 % wt., in which water diffusivity was observed to be fairly high up to 110^{o}C. At room temperature, D was measured to be 1.30 x 10^{-5} cm^2/s, which is about a factor of two lower than the diffusion value of free water at room temperature (i.e. D ~ 2.29 x10^{-5} cm^2/s). At 100^{o}C, D reached a value of 4.57 x 10^{-5} cm^2/s and then decreased at higher temperature. By observing the highest water diffusivity in this particular highly sulfonated 6F-SPTES-70 copolymer, affirmed is the claim that water mobility is a function of the degree of initial water uptake, which in turn is related to the degree of sulfonation. With such a high level of water uptake in 6F-SPTES-70/76.5% wt., however, issues regarding

membrane integrity may still need to be considered when the membrane is finally put into the cell assembly. The high rate of water diffusion in 6F-SPTES-70/76.5% wt. is consistent with T_1 data for this sample, as short correlation times for the water molecules in the membranes could be inferred from the data in Fig. 9.5. T_1 of water was also shown to decrease at ~100°C, about the same temperature at which water diffusion begins to diminish, thus indicating a reduced molecular mobility over a broad range of time scales.

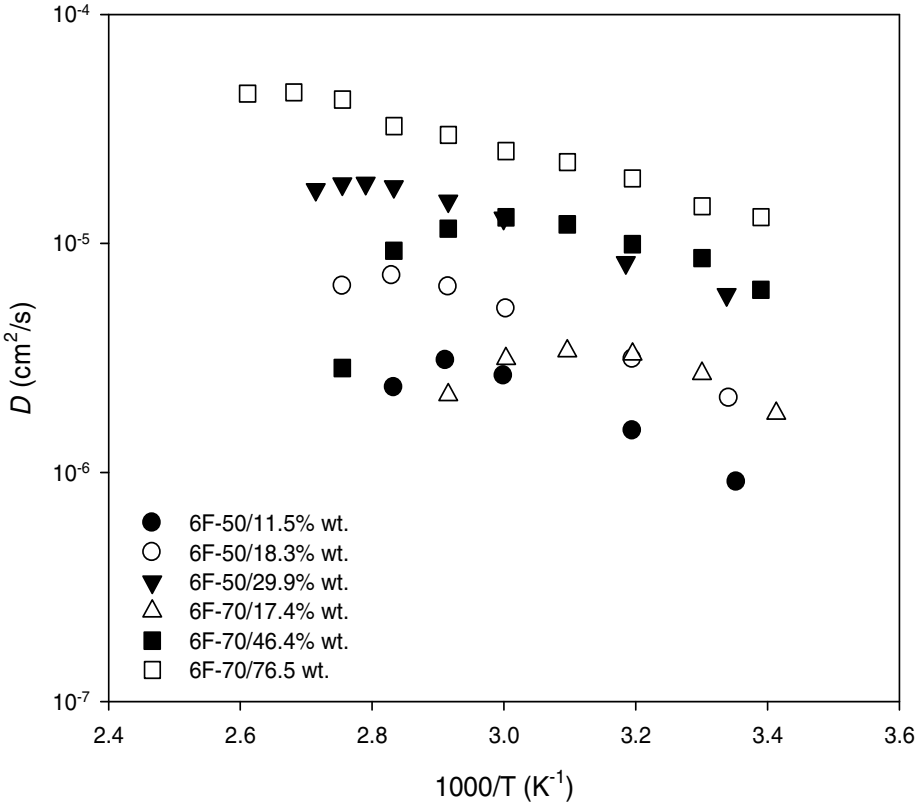

Fig. 9.6– Water Diffusion in 6F-SPTES Copolymer Membranes as a Function of Temperature.

In comparing the 6F-SPTES copolymer membranes, including 6F-SPTES-70/76.5% wt., to SPTES copolymer membranes, we conclude that water retention decreases as a result of inserting the fluorine functionalities in

the backbone structure of SPTES copolymers. We can cite, as evidence, prior diffusion studies performed on SPTES-50 copolymer membranes [174], in which these membrane demonstrated good water retention up to 160^{o}C, where the water self-diffusion coefficient rose to a value of approximately 4.50×10^{-5} cm^2/s. It may be the case that the addition of fluorine groups lowers the glass transition temperature T_g of the polymer matrix, which affects the retention properties of the membrane in a way opposite to what was sought. High degrees of sulfonation in SPTES copolymer membranes can raise T_g of the polymer matrix, which may be an additional factor (besides increased hydrophilicity) for somewhat better water retention in 6F-SPTES-70/76.5% wt. [183]

We can gain more understanding into the mechanism of water retention by drawing a comparison between samples 6F-SPTES-50/18.3% wt. and 6F-SPTES-70/17.4% wt., which both possess comparable water contents. As seen in Fig. 9.6, the samples exhibit similar diffusive behavior for the first few temperatures. However, for 6F-SPTES-70/17.4% wt., water diffusion drops at about 70^{o}C, while for 6F-SPTES-50/18.3% wt., diffusion keeps rising to almost 90^{o}C. Thus higher initial water uptake dictated by a higher degree of sulfonation does not necessarily correlate with water retention capability at elevated temperature, at lower water content. This finding has obvious relevance to fuel cells operating under relatively low relative humidity (RH) conditions. The effect of lower initial water content also produces a similar trend in the 6F-SPTES-50 membranes, where fall-off in the diffusion is observed at lower temperature than for the more hydrated sample.

Proton conductivity data of hydrated 6F-SPTES-50 and 6F-SPTES-70 membranes carried out at 85% RH, are displayed in Fig. 9.7 with molecular weights, inherent viscosities, and conductivity values recorded in Table 9.1. As expected, proton conductivity measurements were higher for the 6F-SPTES-70 membrane in the temperature range investigated (45°C–85°C). Proton conductivity is thus shown to be directly related to the water content of the membrane.

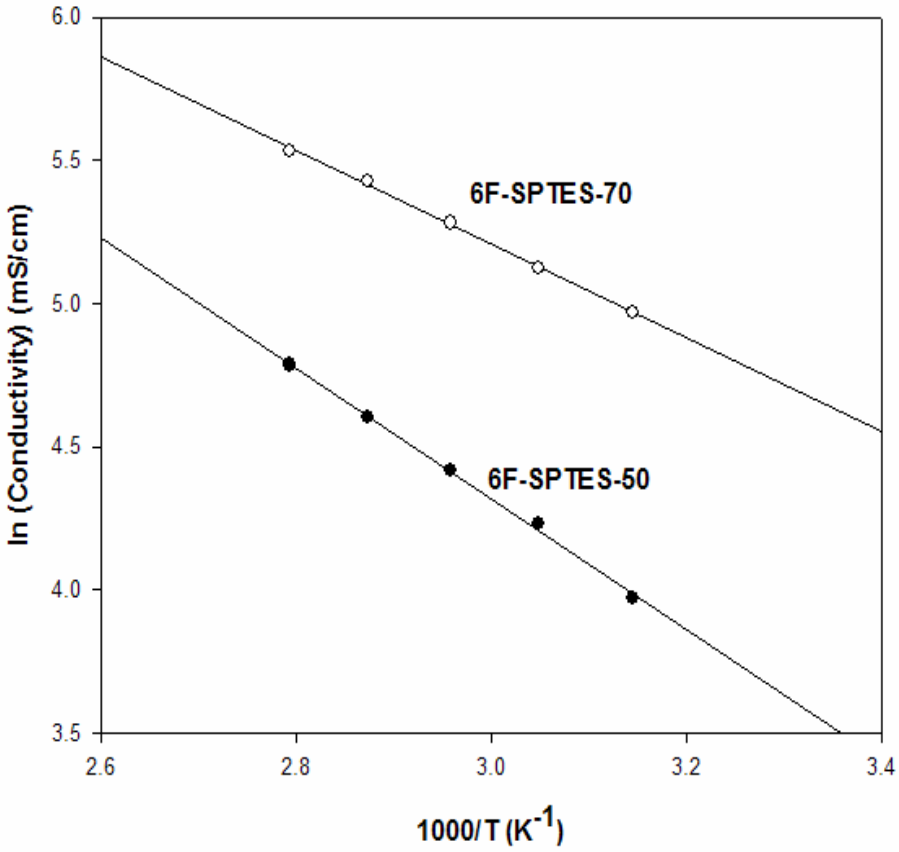

Fig. 9.7 - Proton conductivity of 6F-SPTES membranes at 85% R.H.

Table 9.1 - Properties of 6F-SPTES Copolymers

Polymer	IV (dL/g)	GPC (Mw/Mn)	TGA (Tsd/Td, °C)	Σ (mS/cm)
6F-SPTES-70	1.35	63.8/29.2	308/552	195
6F-SPTES-50	0.92	61.2/25.8	322/565	83

Notes: σ: Proton conductivity was tested at 65°C, 85% relative humidity.

A previous study on SPTES-50 copolymer with 41% water uptake at 65°C and 85% RH, had been reported to generate a proton conductivity of 100 mS/cm, a 25% greater value than that found for hydrated Nafion-117 under similar conditions [173]. With regard to the study contained herein, 6F-SPTES-50 membrane yielded a conductivity of 83 mS/cm, a 17% decrease from the SPTES-50 conductivity measurement. A SPTES-70 copolymer, also at 65°C and 85% R.H. but with 73% water uptake, had been reported to produce a conductivity measurement of 175 mS/cm [173]. 6F-SPTES-70 copolymer provided a modest 11% increase in proton conductivity at the same temperature and relative humidity (see Table 1). It should be noted that replacement of the thioether spacers with the 6F functionalities results in a modest decrease in ion exchange capacity, although this does not appreciably change the interpretation of the results herein.

9.4 Conclusions

The proton and water transport properties of 6F-SPTES copolymers (6F-SPTES-50 and 6F-SPTES-70) were investigated in this study. The

conductivities measured for the 6F-SPTES copolymer membranes were significantly higher than those of commercial Nafion membranes. Although initial water uptake of the 6F-SPTES copolymer membranes was fairly high, they exhibited decidedly inferior water retention capabilities at elevated temperature, compared to their non-fluorinated counterparts.

Acknowledgments

The research at Hunter College was supported by the Air Force Office of Scientific Research and an infrastructure grant from the National Institutes of Health (RR-03037).

Chapter 10: A Summary of Conclusions

The work presented here aims to characterize ion and molecular transport properties of polymer electrolytes for Li-ion batteries and fuel cells. The motivation in conducting such studies is to determine the usefulness, effectiveness, and practicality of a particular polymer electrolyte for possible commercial and domestic applications which include powering laptops to powering and heating our homes. The ability of a polymer membrane to permeate ion or molecular flow with ease is indispensable to a high performing, efficient Li-ion battery or fuel cell. Mechanical strength and thermal stability are other important properties to consider in developing suitable polymer electrolytes for the electrochemical devices discussed.

In our investigation of the NASA rod-coil block copolymer, the NMR temperature-dependent linewidths for the lithium cation and the fluorine containing anion revealed similar activation energies. This suggests that both ions have a common factor in their dynamics, i.e. polymer segmental motion in the amorphous phase of PEO. Linewidth data supported diffusion data, which also revealed similar temperature dependencies for both ions. This again suggests the common link for the ion mobilities - polymer segmental dynamics. The anion diffusion was significantly higher than the cation diffusion in spite of the relatively large size of the anion. Such behavior is typically the case for polyether based polymer electrolytes. In addition, ^{7}Li and ^{19}F T_1 minima were shown to occur at different temperatures. This suggests that ^{7}Li T_1 was largely affected by polymer segmental dynamics, while ^{19}F T_1 was dominated by rotation of the CF_3 group on the anion.

The rod-coil blocks have been shown to be durable, flexible, thermally and mechanically stable up to high temperatures, and predominately amorphous over a broad temperature range. These copolymers are thus very good candidates for fully operable solid polymer electrolytes. In fact, research is currently being undertaken by NASA Glenn where new block copolymers systems are being developed that that improve upon the conductivity of the rod-coil block copolymer systems while maintaining dimensional stability. Such systems have higher degrees of branching to increase conductivity and include greater cross-linking for desired mechanical strength. These effects are achieved by replacing the rigid PI rods with a triazine molecule ($C_3H_3N_3$) that has three reactive sites.

In studying the seven gel polymer electrolytes prepared by collaborators from the University of Rome, labeled #1, #2, #20S, #25S, #26S, #29S, #6, there were considerable variations in composition with each gel sample. Nonetheless, we were able to conclude that samples #1 and #6 exhibit restricted ionic motion as evidenced by their relatively short NMR T_1 values across all nuclei investigated (^1H, ^7Li, ^{19}F) along with low diffusion for each nucleus as well. The BMI ionic liquid component may be the cause for the observed behavior in samples #1 and #6. In addition, sample #26S possessed the highest lithium cation diffusion out of all samples studied, and was even greater than any of the fluorine anion diffusivity. This result is significant in that most electrolytes tend to have higher anion diffusion, yet it is desired for high transference of lithium charge. A reason for lower anion diffusion in sample #26S may be that TMP phosphate is functioning like anion receptor. A sudden drop was observed in the Li^+ diffusion curve for sample #26, which we

believe to be due to a phase separation. Overall, the seven gels studied leave a lot of room for more investigation. The BMI ionic liquid may have been thought to improve ion transport, but it may be the organic solvent mixtures that are causing another mechanism to counter high mobility. In continuing studying these composite materials, it may be reasonable to have the BMI ionic liquid component included in one sample (Sample A) with a certain concentration of organic solvent mixtures, and compare it with another sample having the same concentration of the solvents yet with no BMI component (Sample B). Depending on the results, we can either remove the BMI component from Sample A and replace it with another component, such as TMP, or add to Sample A something else but all throughout keep Sample B (with no BMI) as a reference that is available.

In the LiTFSI/P_{13}TFSI/PVDF-HFP gel polymer electrolytes for potential use in lithium metal batteries, NMR investigations showed that the smallest ion, Li^+, possessed the lowest self-diffusion coefficient among all ions including P_{13}^+ and $TFSI^-$. We may ascribe this behavior to a high degree of association that exists between Li^+ and $TFSI^-$. P_{13}^+, on the other hand, is freed from $TFSI^-$ allowing for it to have a greater motion than Li^+.

Li^+ diffusion is smaller in the gel polymer electrolytes than in the binary ionic liquids for any given lithium salt concentration. In both the binary ionic liquids and the corresponding gel polymer electrolytes, an increase in the lithium salt concentration leads to a decrease in the Li^+ self-diffusion coefficient. The implication therein is that an increase in lithium salt concentration increases the viscosity of the electrolyte. In addition, we did

observe a slight increase in the activation energy of Li^+ self-diffusion with lithium concentration.

Perhaps most important of all in studying these particular gels is that the addition of a small amount of EC, ethylene carbonate, was shown to improve ionic conductivity, net Li^+ transport number, and Li^+ transport kinetics dramatically. The mobility of Li^+ ions was highest in the membrane with 20% EC and slowest in the membrane without EC. This clearly indicates that adding EC improves the Li^+ transference number in the gel polymer electrolyte. ^7Li T_1 data supports this claim, as it reveals a shift in the T_1 minimum to lower temperatures for the membrane with EC. The value of D_{Li} for the 1M LiTFSI/0.2EC+0.8P_{13}TFSI/PVDF-HFP gel polymer sample is more than three times that of the gel without EC. Adding EC was also found to increase the mobility of $TFSI^-$ ions but had no large effect on the mobility of P_{13}^+ ions.

Fundamental understanding of the ionic transport mechanism in a lithium salt/ionic liquid complex of a gel polymer electrolyte is not very well understood. NMR has been a powerful tool in determining the ionic diffusion coefficient as well as the degree of ionic association. Further study of the ion transport mechanism of these gel polymer electrolytes needs to be undertaken in order to elucidate other key factors that can contribute to Li^+ transport besides the addition EC. Practically speaking, it is very important to improve Li^+ transport properties so as to improve the rate capability of Li-ion batteries in general since other ions can act to polarize the electrode.

Water and methanol mobility were studied in Nafion 117 and SPTES-50 membranes which had been equilibrated in 2M MeOH for DMFC

application. SPTES membranes showed higher water diffusion than Nafion, especially above 80^{o}C. Water diffusion remained high up to 160^{o}C, which suggested that water was well retained for elevated temperatures. Furthermore, the selectivity, defined as the ratio of water diffusion to methanol diffusion, was higher for SPTES-50 than for Nafion. In other words, the SPTES-50 shows less permeability to methanol and more permeability to water. The SPTES-50 copolymer membranes have shown to have outstanding thermal and mechanical properties, high proton conductivity, and good electrochemical characteristics. They are excellent candidates for future use as PEMs.

6F-SPTES-50 and 6F-SPTES-70 copolymer membranes were examined for applications as PEMs as well. We found these membranes to have markedly weaker water retention capabilities than their non-fluorinated SPTES counterparts at elevated temperatures. Also, the conductivities measured for the fluorinated membranes were not significantly different than those of the non-fluorinated membranes. The lower water retention of the 6F-SPTES copolymer membranes at elevated temperatures can be presumably attributed to the enhanced hydrophobicity of the 6F-SPTES membrane acting to expel water more effectively. We speculate that increased thermal motions apparently results in the loss of some bound water from within the ionic clusters at higher temperatures more easily in 6F-SPTES copolymer membranes. A 6F-100 homopolymer was found to be almost water soluble as it had taken up too much water due to the very high degree of sulfonation and had lost structural integrity.

The underlying point of emphasis throughout this work is to present the different ways in which ionic and molecular transport can be enhanced be it through the use of ionic liquids, block copolymers, organic solvents, or sulfonic acid groups. NMR measurements were performed and analyzed. Yet other spectroscopic techniques may be used as well and may even provide greater insight into dynamic systems such as polymer electrolytes. The future development of Li-ion batteries and fuel cells hinges upon the use of different experimental techniques on different materials to elucidate the advantages or disadvantages in employing those certain materials and drive the science forward.

Bibliography

[1] M.S. Dresselhaus, G.W. Crabtree, and M.V. Buchanan, MRS Bulletin 30 (2005) 518.

[2] Coalition for Affordable and Reliable Energy, Energy and America's Economy, "www.careenergy.com/energy/energy-americas-economy.asp," 2003.

[3] P. Hoffman, Tomorrow's Energy: Hydrogen, Fuel Cells, and the Prospects for a Cleaner Planet, Reprint ed., The MIT Press, USA, 2001.

[4] BBC News, *Riddle of 'Baghdad's batteries,'* "news.bbc.co.uk/1/hi/sci/tech/2804257.stm," 2003.

[5] D. Giancoli, Physics: Principles with Applications, 6th ed., Prentice Hall, NJ, 2004.

[6] Britannica Student Encyclopedia, *Voltaic Cell*, "www.britannica.com/ebi/art/print?id=52967&articleTypeId=0," 2007.

[7] L.A. Bloomfield, How Everything Works: Making Physics Out of the Ordinary, 1st ed., John Wiley & Sons, Place, 2006.

[8] Duracell, *Alkaline Manganese Dioxide*, "www.duracell.com/oem/Pdf/others/ATB-full.pdf," 2005.

[9] Encyclopedia Britannica Inc., "www.britannica.com/eb/art/print?id=19439&articleTypeId=0," 2006.

[10] Answers.com, *Nickel-Cadmium Battery*, "http://www.answers.com/topic/nickel-cadmium-battery?cat=technology," 2007.

[11] Cadex Electronics Inc., *Is Lithium-Ion the Ideal Battery?*,"http://www.batteryuniversity.com/partone-5.htm," 2005.

[12] D. Linden, T.B. Reddy, Handbook of Batteries, 3rd ed., McGraw-Hill, USA, 2002.

[13] NEC/Tokin, *Lithium-Ion Rechargeable Battery*, "www.nectokin.com/english/product/me/chisiki/img/Dousa-b.jpg," 2004.

[14] Paul Scherrer Institut, *Batteries*, "http://ecl.web.psi.ch/lithium," 2007.

[15] United States Patent 20020102461, *Lithium ion battery containing an anode comprised of graphitic carbon nanofibers*, "www.freepatentsonline.com/20020102461.html," 2002.

[16] M. Despotopoulou, M.T. Burchill, Progress in Organic Coatings 45 (2002) 119.

[17] Y.H. Rho, K. Kanamura, Journal of Power Sources 158 (2006) 1436.

[18] W.H. Meyer, Advanced Materials 10 (1999) 439.

[19] F.A. Amaral, C. Dalmolin, S.C. Canobre, N. Bocchi, R.C. Rocha-Filho, S.R. Biaggio, Journal of Power Sources 164 (2007) 379.

[20] T. Inada, K. Takada, A. Kajiyama, M. Kouguchi, H. Sasaki, S. Kondo, M. Watanabe, M Murayama, R. Kanno, Solid State Ionics 158 (2003) 275.

[21] C.A. Vincent, Solid State Ionics 134 (2000) 159.

[22] M.B. Armand, J.M. Chabagno, M.J. Duclot, in Fast-ion transport in solids: Electrodes and Electrolytes, Eds. P. Vashishta, J. N. Mundy and G. Shenoy, Elsevier, Amsterdam: North–Holland, 1979.

[23] Corrosion Doctors, *Lithium-Ion Polymer Battery*, "www.corrosion-doctors.org/Secondaries/li-ion-poly.htm," 2007.

[24] Q. Li, N. Imanishi, Y. Takeda, A. Hirano, O. Yamamoto. Electrochem. Solid-State Lett. 7 (2004) A470.

[25] A. Isaacs, Oxford Dictionary of Physics, 5th ed., Oxford University Press, UK, 2005.

[26] Riso, *History of the Fuel Cell*, "www.risoe.dk/Afd-abf/sofc/fuel/history_uk.htm," 2007.

[27] NASA, *Spacecraft Systems Become More Troublesome*, "www.hq.nasa.gov/office/pao/History/SP-4203/ch7-4.htm." 2007.

[28] Answers.com, *Proton Exchange Membrane Fuel Cell*, "http://www.answers.com/topic/proton-exchange-membrane-fuel-cell," 2007.

[29] O.J. Murphy, G.D. Hitchens, D.J. Manko, Space Electrochemical Research and Technology 11 (1993) 149.

[30] F. Tailoka, D.J. Fray, R.V. Kumar, Solid State Ionics 161 (2003) 267.

[31] T. Kalli, Electrochemical and Physiochemical Characterization of Radiation-Grafted Membranes for Fuel Cells. Ph.D. thesis, Helsinki University of Technology (2003).

[32] J.R.P. Jayakody, A. Khalfan, E.S. Mananga, S.G. Greenbaum, T.D. Dang, R. Mantz, Journal of Power Sources 156 (2006) 195.

[33] M.B. Comisarow, A.G. Marshall, Journal of Mass Spectroscopy 31 (1996) 581.

[34] D.J. Lurie, S.J. Mccallum, J.M.S. Hutchison, M. Aleccit, Magnetic Resonance Materials in Physics, Biology and Medicine 4 (1996) 77.

[35] J.W. Emsley, J. Feeney, Progress in Nuclear Magnetic Resonance Spectroscopy 50 (2007) 179.

[36] Eds. L. D. Field, S. Sternhell, Analytical NMR, 1st ed., John Wiley & Sons, New York, 1989.

[37] J.A. Ferretti and R.R. Ernst, J. Chem. Phys. 65 (1976) 4283.

[38] P. Mansfield, I.L. Pykett, J. Magn. Reson. 29 (1978) 355.

[39] L.D. Field and S. Sternhell, Analytical NMR, John Wiley & Sons, United Kingdom, 1989.

[40] C. Kittel, Introduction to Solid State Physics, 8th Edition, John Wiley & Sons, USA 2004.

[41] E. Fukushima and S. Roeder, Experimental Pulse NMR, Westview Press, USA, 1981.

[42] J.R. Singer, J. Phys. E: Sci. Instrum. 11 (1978) 281.

[43] UBC Chemistry, *Magnetism, Curie's Law and the Bloch Equations*, "www.chem.ubc.ca/faculty/straus/Nlecture1.pdf," 2006.

[44] J.R.P. Jayakody, Nuclear Quadrupole Resonance Studies of the "SORC" Sequence and Nuclear Magnetic Resonance Studies of Polymers. Ph.D. thesis, The Graduate Center CUNY (1993).

[45] M.J. Williamson, J.P. Southall, H.V.St.A. Hubbard, S.F. Johnston, G.R. Davies, I.M. Ward, Electrochimica Acta 43 (1998) 1415.

[46] Chemagnetics CMX Reference, Solids System Block Diagram, 1994.

[47] E. Fukushima and S. Roeder, Experimental Pulse NMR, Westview Press, USA, 1981.

[48] M.A.B. Meador, J.D. Kinder, W.R. Bennett, *Novel Molecular Architectures Developed for Improved Solid Polymer Electrolytes for Lithium Polymer Batteries*, "www.grc.nasa.gov/WWW/RT2001/5000/5160meador.html," 2002.

[49] M.A.B. Meador, V.A. Cubon, D.A. Scheiman, W.R. Bennett, Chem.Mater. 15 (2003) 3018.

[50] C. Xue, M.A.B. Meador, L. Zhu, J.J. Ge, S.Z.D. Cheng, S. Putthanarat, R.K. Eby, A. Khalfan, G.D. Bennett, S.G. Greenbaum, Polymer 47 (2006) 6149.

[51] A. Johansson, Dynamic Properties of Polymer Electrolytes Studied by NMR Spectroscopy, Ph.D. thesis, Uppsala University (1995)

[52] Great Lakes Industrial Technology Center, Better Performance with *NASA Glenn's Lithium Polymer Battery*, "www.glitec.org/techJuly05.htm," 2005.

[53] D.M. Tigelaar, M.B. Meador, J.D. Kinder, W.R. Bennett, *Novel Elastomeric Membranes Developed for Polymer Electrolytes in Lithium Batteries*, "www.grc.nasa.gov/WWW/RT/2004/RM/RM09P-tigelaar.html." 2005

[54] F. Ciuffa, F. Croce, A. D'Epifanio, S. Panero, B. Scrosati, Journal of Power Sources 127 (2004) 53.

[55] M.K. Song, Y.T. Kim, Y.T. Kim, B.W. Cho, B.N. Popov, and H.W. Rhee, J. Electrochem. Soc. 150 (2003) A439.

[56] B. Barriere, *A Family of Fluorinated Processing-Aids for Polyolefins*, "www.arkema-inc.com/literature/pdf/253.pdf," 2007.

[57] N. Byrne, Enhanced Ion Dissociation in Polyelectrolyte Gel Materials, Ph.D. thesis, Monash University, 2006.

[58]. M. Smart, R. Bugga, S. Surampudil, *Ethyl methyl carbonate as a cosolvent for lithium-ion cells*, "findarticles.com/p/articles/mi_qa3957/is_200106/ai_n8973554," 2001.

[59] H.H. Lee , Y.Y. Wang , C.C. Wan , M.H. Yang, H.C. Wu, D.T. Shieh, Journal of Applied Electrochemistry 35 (2005) 615.

[60] X. Wang, E. Yasukawa, S. Kasuya, J. Electrochem. Soc. 148 (2001) A1058.

[61] H. Olivier-Bourbigou, L. Magna, *Ionic Liquids. Perspectives for Organic and Catalytic Reactions*, "iusti.polytech.univ mrs.fr/MOLTEN_SALTS/IUSTI_EDITION/75/edito75.pdf," 2002.

[62] P.E. Stallworth, J. Li, S.G. Grembaum, F. Croce, S. Slane, M. Saloman, Solid State Ionics 73 (1994) 119.

[63] F. Croce, G. B. Appettechi, S. Slane, M. Saloman, M. Tavarez, S. Arumugam, Y. Wang, S.G. Greenbaum, B. V. Chowdari, Solid state ionics 86 (1996) 307.

[64] B. Oh and K. Amine, Solid State Ionics, 175 (2004) 785-788.

[65] P.E. Stallworth, S.G. Greenbaum, F. Croce, S. Slane, M. Salomon, Electrochim. Acta 40 (1995) 2137.

[66] H. Ye, Investigation of Novel Electrolyte Systems for Advanced Metal/Air Batteries and Fuel Cells, Ph.D. Thesis, Rutgers State University of New Jersey, 2007.

[67] A. Dobley, J. DiCarlo, K.M. Abraham, *Non-aqueous Lithium-Air Batteries with an Advanced Cathode Structurehttp*, "www.yardney.com/lithion/Documents/PaprAD-JD-KMA.pdf," 2007.

[68] K.M. Abraham, Z. Jiang, J. Electrochem. Soc. 143 (1996) 1.

[69] H. Ye and J.J. Xu, *Novel Polymer Electrolytes Based on Ionic Liquids and Their Application to Solid-state Thin-film Li-Air Batteries*, "http://ecsmeet2.peerxpress.org/ms_files/ecsmeet2/2006/05/21/0004078 6/00/40786_0_art_file_0_1148268172.pdf," 2006.

[70] S. Slade, S.A. Campbell, T.R. Ralph, F.C. Walsh, Journal of the Electrochemical Society 149 (2002) A1556.

[71] J. Payne, *Nafion® - Perfluorosulfonate Ionomer*, "www.psrc.usm.edu/mauritz/nafion.html," 2005.

[72] Heitner-Wirguin, 1996, Mauritz et al, 2004).

[73] J. O. M. Bockris, A. K. N. Reddy, M. Gamboa-Aldeco, Modern Electrochemistry, Plenum, New York, 1998.

[74] T. A. Zawodzinski, T. E. Springer, J. Davey, R. Jestel, C. Lopez, J. Valerio, S. Gottesfeld, J. Electrochem. Soc. 140 (1993) 1981.

[75] H.L. Yeager, A. Eisenberg, Perfluorinated ionomer membranes, in: A. Eisenberg, H.L. Yeager (Eds.), ACS Symp. Series 180, Amer. Chem. Soc, Washington, DC, 1982.

[76] B.S. Pivovar, Polymer 41 (2006) 4194.

[77] G.Q. Lu, F.Q. Liu, C.Y. Wang, Electrochemical and Solid-State Letters 8 (2005) A1-A4.

[78] J.R.P. Jayakody, A. Khalfan, E.S. Mananga, S.G. Greenbaum, T.D. Dang and R. Mantz, Journal of Power Sources 156 (2006) 195-199.

[79] S. Rodrigues, *Propulsion Directorate*, "www.pr.afrl.af.mil/mar/2005/oct2005.pdf," 2005.

[80] F.S. Bates and G.H. Fredrickson, *Annu Rev Phys Chem* 41 (1990), p. 525.

[81] L. Zhu, S.Z.D. Cheng, B.H. Calhoun, Q. Ge, R.P. Quirk and E.L. Thomas *et al.*, *J Am Chem Soc* 122 (2000), p. 5957.

[82] C. Park, C.De. Rosa, L.J. Fetters and E.L. Thomas, *Macromolecules* 33 (2000), p. 7931.

[83] D.E. Fenton, J.M. Parker and P.V. Wright, *Polymer* 14 (1973), p. 589.

[84] M.B. Armand, J.M. Chabagno and M. Duclot, Fast ion transport in solids. In: P. Vashishta, J.N. Mundy and G.K. Shenoy, Editors, North Holland, New York (1979), p. 131.

[85] D. Golodnitskyz, E. Livshits, R. Kovarsky, E. Peled, S.H. Chung and S. Suarez *et al.*, *Electrochem Solid-State Lett* **7** (2004), pp. A412–A415.

[86] P.V. Wright, *MRS Bull* 27 (2002), pp. 597–602.

[87] Y.T. Kim and E.S. Smotkin, *Solid State Ionics* 149 (2002), pp. 29–37.

[88] A. Nishimoto, K. Agehara, N. Furuya, T. Watanabe and M. Watanabe, *Macromolecules* 32 (1999), pp. 1541–1548.

[89] F. Croce, L. Persi, B. Scrosati, F. Serraino-Fiory, E. Plichta and M.A. Hendrickson, *Electrochim Acta* 46 (2001), p. 2457.

[90] P.P. Soo, B. Huang, D.R. Sadoway and A.M. Mayes, *J Electrochem Soc* 146 (1999), p. 32.

[91] M. Yoshino, K. Ito, H. Kita and K. Okamoto, *J Polym Sci B Polym Phys* 38 (2000), pp. 1707–1715.

[92] K. Okamoto, M. Fujii, S. Okamyo, H. Suzuki, K. Tanaka and H. Kita, *Macromolecules* 28 (1995), pp. 6950–6958.

[93] Initial screening of other rod and coil combinations was reported inM.A.B. Meador, V.A. Cubon, D.A. Schieman and W. Bennett, 11th International meeting on lithium batteries, *Meeting abstracts* 153, The Electrochemical Society, Pennington, NJ (June 23–28, 2002).

[94] M.A.B. Meador, V.A. Cubon, D.A. Scheiman and W.R. Bennett, *Chem Mater* 15 (2003), p. 3018.

[95] E.O. Stejskal and J.E. Tanner, *J Chem Phys* 42 (1965), pp. 288–292.

[96] Y. Takahashi and H. Tadokoro, *Macromolecules* 6 (1973), p. 672.

[97] M. Avrami, *J Chem Phys* **7** (1939), p. 1103.

[98] Y. Lee and R.S. Porter, *Macromolecules* 21 (1988), p. 2770.

[99] M. Ratner, P. Johanson and D.F. Shriver, *MRS Bull* 25 (2000), pp. 31–38.

[100] Z. Gadgourova, Y. Andreev, D. Tunstall and P. Bruce, *Nature (London)* 412 (2001), pp. 520–523.

[101] D. Golodnitsky, E. Peled, E. Livshits, A. Ulus, Z. Barkay and I. Lapides *et al.*, *J Phys Chem A* **105** (2001), pp. 10098–10106.

[102] F. Ciuffa, F. Croce, A. D'Epifanio, S. Panero, B. Scrosati, Journal of Power Sources 127 (2004) 53.

[103] ChemFinder. "*Chemical Name*," from "chemfinder.cambridgesoft.com," 2004.

[104] J. Dupont, C. S. C., and J. Spencer, Journal of the Brazilian Chemical Society 11 (2000) 337.

[105] S. Suarez, S. Abbrent, S. G. Greenbaum, J. H. Shin, S. Passerini, Solid State Ionics 166 (2004) 407.

[106] S. Abbrent, S.H. Chung, S.G. Greenbaum, J. Muthu, E.P. Giannelis, Electrochimica Acta 48 (2003) 2113.

[107] J.-M. Tarascon, M. Armand, Nature 414 (2001)359.

[108] R. P. Hamlen, T. B. Atwater, in *Handbook of Batteries* D. Linden, T. B. Reddy, Eds. (McGraw Hill, 2002) pp. 38.1.

[109] K. M. Abraham, Z. Jiang, J. Electrochem. Soc. 143 (1996)1.

[110] J. Read, J. Electrochem. Soc. 149 (2002)A1190.

[111] P. Bonhote, A. P. Dias, N. Papageorgiou, K. Kalyanasundaram, M. Gratzel, Inorg. Chem. 35 (1996)1168.

[112] A. B. McEwen, H. L. Ngo, K. LeCompte, J. L. Goldman, J. Electrochem. Soc. 146 (1999)1687.

[113] J. Caja, T. D. J. Dunstan, D. M. Ryan, V. Katovic, paper presented at the Proceeding of Electrochem. Soc. 2000.

[114] A. Webber, G. E. Bloomgren, in *Advances in Lithium-ion Batteries* W. A. v. Schalkwijk, B. Scrosati, Eds. (Kluwer Academic/Plenum Publ., New York, 2002) pp. 185.

[115] H. Sakaebe, H. Matsumoto, Electrochem. Comm. 5 (2003)594.

[116] J. H. Shin, W. A. Henderson, S. Passerini, Electrochem. Comm. 5

(2003)1016.

[117] W. Xu, C. A. Angell, Science 302 (2003)422.

[118] A. Noda *et al.*, J. Phys. Chem. B 107 (2003)4024.

[119] M. Doyle, S. K. Choi, G. Proulx, J. Electrochem. Soc. 147 (2000)34.

[120] R. D. Rogers, K. R. Seddon, *Ionic Liquids: Industrial Applications for Green Chemistry*, ACS Symposium Series 818 (American Chemical Society, Washington DC, 2002), pp. 1.

[121] H. Matsumoto *et al.*, paper presented at the Molten Salts XII-Proceeding of the Electrochemical Society 2000.

[122] S. Seki *et al.*, Electrochem and Solid-State Lett. 8 (2005)A577.

[123] D. R. MacFarlane, P. Meakin, J. Sun, N. Amini, M. Forsyth, J. Phys. Chem. B 103 (1999)4164.

[124] P. C. Howlett, D. R. MacFarlane, A. F. Hollenkamp, Electrochem. Solid-State Lett. 7 (2004)A97.

[125] K. Hayashi, Y. Nemoto, K. Akuto, Y. Sakurai, J. Power Sources 146 (2005)689.

[126] T. E. Sutto, P. C. Trulove, H. C. D. Long, paper presented at the Molten Salts XIII, Pennington, NJ 2002.

[127] J.-H. Shin, W. A. Henderson, S. Passerini, Electrochem and Solid-State Lett. 8 (2005)A125.

[128] J.-H. Shin, W. A. Henderson, S. Passerini, J. Electrochem. Soc. 152 (2005)A978.

[129] A. Noda, K. Hayamizu, M. Watanabe, J. Phys. Chem. B 105 (2001)4603.

[130] K. Hayamizu, Y. Aihara, H. Nakagawa, T. Nukuda, W. S. Price, J. Phys.

Chem. B 108 (2004)19527.

[131] N. Bryne, P. C. Howlett, D. R. MacFarlane, M. Forsyth, Adv. Mater. 17 (2005)2497.

[132] C. Tiyapiboonchaiya *et al.*, Nat. Mater. 204 (2004)29.

[133] Y. Katayama, M. Yukumoto, T. Miura, Electrochem and Solid-State Lett. 6 (2003)A96.

[134] T. Sato, T. Maruo, S. Marukane, K. Takagi, J. Power Sources 138 (2004)253.

[135] J. Fuller, A. C. Breda, R. T. Carlin, J. Electrochem. Soc. 144 (1997)L67.

[136] J. Fuller, A. C. Breda, R. T. Carlin, J. Electroanalytical Chem. 459 (1998)29.

[137] M. Watanabe, T. Mizumura, Solid State Ionics 86-88 (1996)353.

[138] A. Noda, M. Watanabe, Electrochim. Acta 45 (2000)1265.

[139] J. Y. Song, Y. Y. Wang, C. C. Wan, J. Power Sources 77 (1999)183.

[140] J. M. Tarascon, A. S. Gozdz, C. N. Schmutz, F. Shokoohi, P. C. Warren, Solid State Ionics 86-88 (1996)49.

[141] J. J. Xu, H. Ye, J. Huang, Electrochem. Comm. 7 (2005)1309.

[142] J. James H. Davis, C. M. Gordon, C. Hilgers, P. Wasserscheid, in *Ionic Liquid in Synthesis* P. Wasserscheid, T. Welton, Eds. (WILEY-VCH, 2003) pp. 7.

[143] E. O. Stejskal, J. E. Tanner, J. Chem. Phys. 42 (1965)288.

[144] E. O. Stejskal, J. Chem. Phys. 43 (1965)3597.

[145] H. Matsumoto *et al.*, Chem. Lett. (2000)922.

[146] F. M. Gray, *Polymer Electrolytes*, materials monographs (The Royal Society of Chemistry, Cambridge, 1997), pp. 1.

[147] I. Nicotera, C. Oliviero, W. A. Henderson, G. B. Appetecchi, S. Passerini, J.Phys. Chem. B 109 (2005)22814.

[148] K. Xu, Chem. Rev. 104 (2004)4303.

[149] E. Fukushima, S.B.W. Roeder, *Experimental Pulse NMR: A Nuts and Bolts Approach*, (Addition-Wesley Publishing Company, Reading, 1981), pp. 164)

[150] J.A. Kerres, *Membr. Sci.* 185 (2001), p. 29.

[151] T.A. Zawodzinski Jr., C. Derouin, S. Radzinski, R.J. Sherman, V.T. Smith, T.E. Springer and S. Gottesfeld, *J. Electrochem. Soc.* 140 (1993), p. 1041.

[152] P. Dimitrova, K.A. Fridrich, U. Stimming and B. Vogt, *Solid-State Ionics* 160 (2002), p. 115.

[153] C. Yang, P. Costamagna, S. Sirinivasan, J. Benziger and A.B. Bocarsly, *J. Power Sources* 103 (2001), p. 1.

[154] R.M. Mooze, S. Gottesfeld and P. Zelenay, *ECS Proc.* 98 (1999) (27), p. 365.

[155] S. Suarez, S.H. Chung, S. Greenbaum, S. Bajue, E. Peled and T. Duvdivani, *Electrochem. Acta* 48 (2003), p. 2187.

[156] T.A. Zawodzinski Jr., T.E. Springer, J. Davey, R. Jestel, C. Lopez, J. Valerio and S. Gottesfeld, *J. Electrochem. Soc.* 140 (1981).

[157] J.J. Fontanella, C.D. Edmonson, M.C. Wintersgill, Y. Wu and S.G. Greenbaum, *Macromolecules* 29 (1996), p. 4944

[158] J.J. Fontanella, M.C. Wintersgill, R.S. Chen, Y. Wu and S.G. Greenbaum, *Electrochem. Acta* 40 (1995), p. 2321.

[159] S. Matsumura, N. Kihara and T. Takata, *Macromolecules* 34 (2001), p. 2848.

[160] F. Wang, M. Hickner and J.E. McGrath, *J. Membr. Sci.* 197 (2002), p. 231.

[161] T.D. Dang, Z. Bai, M.J. Dalton and E. Fossum, *Proceedings of the Polymer Preprints ACS National Meeting, vol. 45* Anaheim (2004), p. 22.

[162] C.P. Slichter, Principles of Magnetic Resonance (3rd ed.), Springer Series in Solid State Science, New York (1990).

[163] J.R.P. Jayakody, P.E. Stallworth, E.S. Mananga, J.F. Zapata and S.G. Greenbaum, *J. Phys. Chem. B* 108 (2004), p. 4260.

[164] M.C. McLin, M.C. Wintersgill, J.J. Fontanalla, R.S. Chen, J.P. Jayakody and S.G. Greenbaum, *Solid-State Ionics* 60 (1993), p. 137.

[165] E.O. Stejskal and J.E. Tanner, *J. Chem. Phys.* 43 (1965), p. 3597.

[166] M. Holz, *Phys. Chem. Chem. Phys.* 2 (2000).

[167] C.A. Edmondson, P.E. Stallworth, M.C. Wintersgill, J.J. Fontenalla, Y. Dai and S.G. Greenbaum, *Electrochim. Acta* 43 (1998), p. 1295

[168] O.J. Murphy, G.D. Hitchens, D.J. Manko, Space Electrochemical Research and Technology 11 (1993) 149-166.

[169] P. Dimitrova, K.A. Fridrich, U. Stimming, B. Vogt, Solid-State Ionics 160 (2002) 115-122.

[170] T. A. Zawodzinski, T. E. Springer, J. Davey, R. Jestel, C. Lopez, J. Valerio and S. Gottesfeld, J. Electrochem. Soc. 140 (1993) 1981-1985.

[171] X. Liu, C. Suo, Y. Zhang, X. Wang, C. Sun, L. Li and L. Zhang, J. Micromech. Microeng.16 (2006) S226-S232.

[172] C. Yang, S. Srinivasan, A.B. Bocarsly, S. Tulyani and J.B. Benziger, Journal of Membrane Science 237 (2004) 145-161.

[173] Z. Bai, T.D. Dang and M.F. Durstock, J. of Membrane Science 281 (2006) 508-516.

[174] J.R.P. Jayakody, A. Khalfan, E.S. Mananga, S.G. Greenbaum, T.D. Dang and R. Mantz, Journal of Power Sources 156 (2006) 195-199.

[175] Z. Bai and T.D. Dang, Macromol. Rapid Commun. 27 (2006) 1271-1277.

[176] M.H. Levitt, Spin Dynamics: Basics of Nuclear Magnetic Resonance, first ed., John Wiley and Sons, New York, 2001, pp. 315-320.

[177] E.O. Stejskal and J.E. Tanner, J. Chem. Phys. 42 (1965) 288-292.

[178] Gierke, T.D.; Hsu, W.Y. in : Eisenberg, A.; Yeager, H.L. (Eds.), Perfluorinated Ionomer Membranes, ACS Symposioum Series No. 180, American Chemical Society, Washington, DC, 1982, p.283

[179] Smitha, B, Sridhar, S. and Khan, A.A. J. Membr. Sci., 2005, (259), 10

[180] Junichi Kawamura, Kazuki Hattori, Takahiro Hongo, Ryo Asayama, Naoaki Kuwata, Takeshi Hattori and Junichiro Mizusaki, Solid State Ionics 176 (2005) 2451-2456.

[181] R.S. Macomber, A Complete Introduction to Modern NMR Spectroscopy, first ed., John Wiley and Sons, New York, 1998, pp. 78-81.

[182] E. Fukushima and S.B. Roeder, Experimental Pulse NMR: A Nuts and Bolts Approach, Addison-Wesley, Massachusetts, 1981, pp. 125-135.

[183] J. Rozière and D.J. Jones, Annual Review of Materials Research 33 (2003) 503-555.